Part III

BROADBAND COMMUNICATION LEO SATELLITE-BASED PASSIVE RADAR

Chapter 5

Broadband Communication LEO Satellite-Based Passive Radar System: Analysis, Design and Developments

Several constellations of broadband Low-Earth Orbit (LEO) communication satellites, such as Starlink or OneWeb, have started to be deployed in the last few years to provide global internet access, becoming potential candidates to be exploited as illumination of opportunity for passive radar applications. In fact, their characteristics provide promising advantages in terms of global coverage, high bandwidth (i.e. better resolution), high received power on Earth surface (i.e. increased maximum range), predictable trajectory, and network density and robustness when compared to other satellite-based illuminators of opportunity. However, they also pose certain challenges for the development of passive radar systems due to the necessity to track the satellites with a narrow beam reference antenna, their fast-relative dynamics which induce range and Doppler migration effects, and the use of non-standardized signals with limited publicly available information, which in addition are not optimized for radar usage.

Therefore, this chapter presents the the analyses of potential capabilities, with a special focus on the estimation of the achievable performance and on the experimental characterization

of the transmitted signals for passive radar applications. Besides, the proposed passive radar architectures and the developed prototypes are also discussed. While in the following chapter, this concept is experimentally validated by using the developed systems and proposed techniques in measurement campaigns, showing potential applications on Earth monitoring and target detection.

5.1 Overview of emerging satellite-based illuminators of opportunity

The reduction in satellite launch costs has brought a revolution in the space sector with a significant increase in the number of satellites launched, as shown in Figure 5.1, most of them deployed in LEO with altitudes below 2000 km. In this regard, multiple LEO satellite constellations have been recently planned and started to be deployed with the objective to provide global services not only for broadband communication but also for Earth observation (e.g. Capella Space, ICEYE or Planet), and positioning, navigation and timing (PNT) (e.g. Xona Systems).

The ongoing deployment of broadband communication satellite constellations in LEO, such as Starlink or OneWeb, generally composed of hundreds or thousands of satellites [Del19], has made available an emerging class of satellite illuminators of opportunity with advantageous characteristics for the development of passive radar systems. In this way, the opportunistic use of the signals transmitted by these novel satellites could help overcome the limitations imposed by previously investigated satellite illuminators of opportunity such as Digital Video Broadcasting Satellites (DVB-S) [Pis20], Global Navigation Satellite Systems (GNSS) [San20; Pas20], Iridium or Inmarsat [Sto17].

As of June 2023, Starlink and OneWeb companies have deployed respectively more than 4300 and 630 satellites out of their first-phase constellations of 4408 and 648 satellites [Spa20; Wor20]. Nevertheless, considering the increasing number of applications filled by several companies (e.g. Telesat, Keppler Communications, Kuiper Systems or Boeing) to deploy

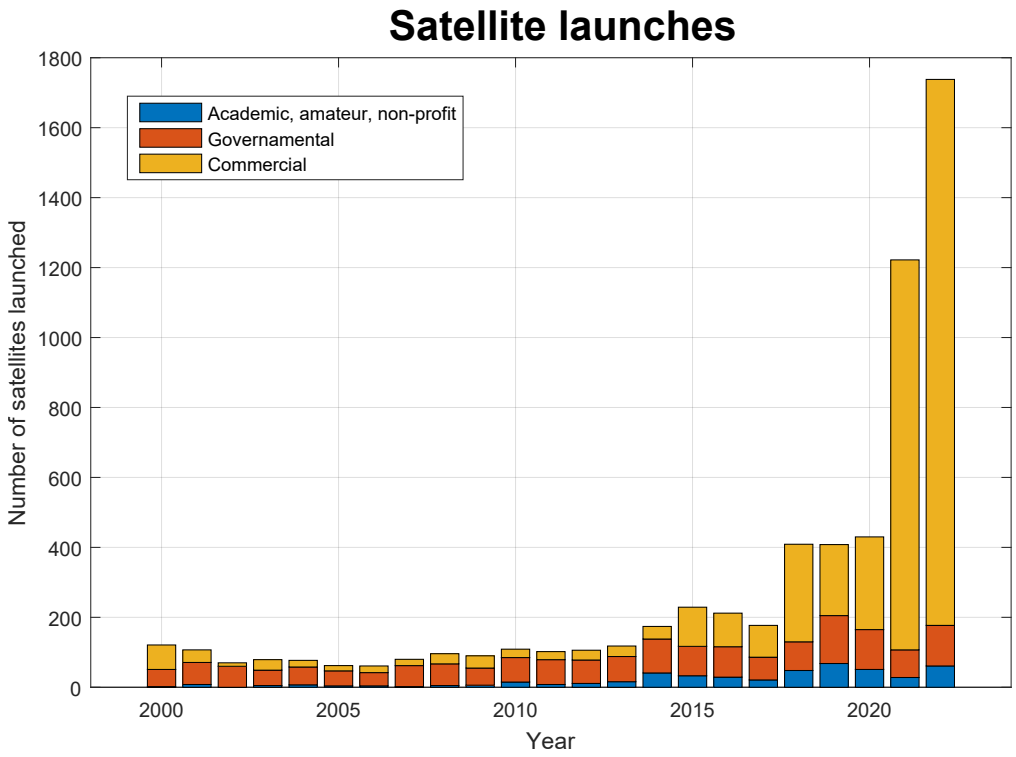

Figure 5.1: Number of satellite launches promoted by commercial, governmental and academic/non-profit institutions (data from [McD]).

and exploit LEO satellites, more and more constellations are expected to be available in the following years [Al 22].

Compared to other space-based illuminators of opportunity for passive radar applications, these new broadband communication satellite constellations provide:

- Global and persistent coverage including oceans, poles and remote areas.
- High bandwidth signals for enhanced range resolution
- High radiated power levels with lower propagation losses due to the shorter transmitter-receiver distances from LEO satellites for enhanced signal-to-noise ratio (SNR) and detection range.
- Transmitter movement that can be estimated and predicted based on publicly available orbital data [Cel] enabling passive Synthetic Aperture Radar (SAR) applications with static ground receivers.

- Transmitter robustness and redundancy with spatial diversity thanks to the multiple and dense constellations.

Therefore, it is highly relevant to analyse and investigate the potential usage of these emerging broadband communication LEO satellites as illuminators of opportunity and their achievable capabilities for passive radar applications. As a comparison with other available satellite illuminators with global coverage, including poles and oceans, Table 5.1 shows the main system parameters of the Starlink constellation, the novel LEO SAR constellations, the TerraSAR-X satellite, and the GNNS constellations. Global and persistent illumination is only achieved by GNNS and Starlink constellation, but the latter offers higher bandwidth signals, higher power levels on Earth surface and a higher transmission frequency more sensitive to Doppler effect and in SAR and interferometric techniques. In this way, the novel broadband communication LEO constellations may enable, for example, emerging persistent high-resolution remote sensing application for local zones with ground-based receivers such as avalanche detection or infrastructure monitoring, even in remote areas where terrestrial transmitters of opportunity have no coverage.

Sayin et al. [Say19] firstly performed a power budget analysis for passive radar target detection considering the preliminary design of the Starlink constellation, which was changed during its deployment, reducing the altitude of the satellites from 1110 km to 550 km. Nevertheless, they showed the theoretical feasibility of a Starlink-based passive radar in terms of signal-to-noise ratio (SNR) when compared to already validated GNSS-based passive radar systems. Besides, the possibility to use Starlink transmissions as opportunistic signals for self-positioning and navigation applications have been recently demonstrated [Kha21; Nei21a].

However, these constellations also pose important challenges for the development of passive radar systems. In order to receive the reference signal with enough signal-to-noise ratio (SNR), the satellites are required to be tracked with a narrow beam reference antenna. Besides, their fast-relative dynamics induce range and Doppler migration effects, which have to be considered when developing the associated signal processing algorithms for target detection applications, apart from giving rise to Doppler-spread clutter which could mask the moving targets. And most significantly, since these LEO constellations are mainly proprietary systems

Table 5.1: Main characteristics of Starlink, LEO SAR constellations (i.e. Iceye and Capella Space), TerraSAR-X and GNSS constellations (i.e. Global Positioning System -GPS- and Galileo). (Notes: Power flux density on Earth surface is estimated assuming pointing towards nadir although SAR satellites usually operate in side-looking mode increasing the propagation distance between the satellite and the Earth surface.)

Parameter	*Starlink*	*Iceye*	*Capella Space*	*TerraSAR-X*	*GPS*	*Galileo*
Number of active satellites (May 2023)	4112	24	10	1 (not a constellation)	31	28
Nominal altitude [km]	540-570	560-580	525	514	20,200	23,222
Orbital inclination	53°, 53.2°, 70°, 97.6°	97.7°	44°, 53°, 97.5°	97.44°	55°	56°
Transmission frequency [GHz]	10.7-12.7	9.65	9.3-10	9.65	1.575 (L1), 1.227 (L2), 1.176 (L5)	1.575 (E1), 1.191 (E5), 1.278 (E6)
Maximum bandwidth [MHz]	240	300	600	300	15.3 (L1), 11 (L2), 12.5 (L5)	24.5 (E1), 51.1 (E5), 40.9 (E6)
Max. transmitting EIRP [dBW]	27.6-31	77.6	76	Not disclosed (∼78 dBW)	∼26.5 (L1), ∼16.6 (L2)	∼32-35
Max. power flux density on Earth surface [dBW/m^2]	-98.2	-48.4	-49.4	-47.2	-130.6 (L1), -140.5 (L2)	-123.3
Global and persistent illumination	Yes	No	No	No	Yes	Yes

with non-standardized signals, there is a lack of publicly available information about their properties, modulation and internal structure, which in addition are not optimized for radar.

Given the potential capabilities and challenges of the emerging LEO communication satellite constellations as illuminators of opportunity for passive radar applications, this doctoral thesis focuses on their analysis, with a particular emphasis on the estimation of the achievable performance, on the experimental characterization of the transmitted signals in terms of the resolution, ambiguities and sidelobe levels of their ambiguity functions, and on the experimental validation of the proposed system and techniques.

To perform the experimental acquisition of the transmitted signals, passive radar prototypes have been developed based on the exploitation of user-downlink signals in the 10.7 – 12.7 GHz band transmitted from these LEO constellations. In this chapter, in addition to the results of the performed analyses, these experimental systems will be described, along with the general passive radar architectures proposed for target detection and imaging applications.

5.2 Starlink and OneWeb satellite constellations

According to the applications approved by the FCC [Spa16; Spa20; Wor20], Starlink and OneWeb are deploying LEO satellite constellations composed in a first stage of 4408 and 648 satellites, respectively, at polar and non-polar orbits. Besides, Starlink has recently started to deploy a second-generation constellation with an orbit inclination of 43°.

The main aim of these constellations is to offer low-latency and high-speed global internet access mainly in rural and remote areas. Since the first Starlink test satellite, launched in February 2018, more than 4600 Starlink satellites have been launched, of which approximately 4300 are currently working in orbit (as of June 2023) providing commercial services in many countries around the world. OneWeb began to deploy its constellation in February 2019, reaching a total of more than 630 operational satellites by June 2023.

The Starlink first-stage constellation is divided into five shells with different inclination angles at altitudes between 540 and 570 km, while OneWeb satellites follow near-polar orbits at 1200 km of altitude. The main parameters of these constellations are detailed in Table 5.2, while Figure 5.2 graphically shows for a specific time both planned constellations, which are almost completely deployed.

In addition, Figure 5.3 represents the percentage of time as a function of the number of visible satellites of the planned OneWeb and Starlink constellations for receivers located in mid-latitudes (i.e. 50° latitude) and in the polar region (i.e. 89° latitude), taking into account the minimum elevation angles specified in the corresponding applications. Given their global characteristic, it can be observed that both constellations persistently provide at least one visible satellite at both considered locations, although OneWeb planned constellation results

Table 5.2: Starlink and OneWeb constellation parameters

Parameter	***Starlink***				***OneWeb***
	Shell 1	*Shell 2*	*Shell 3*	*Shell 4/5*	
Orbital planes	72	72	36	6/4	12
Satellites per plane	22	22	20	58/43	49 (+5 spare)
Altitude	550 km	540 km	570 km	560 km	1200 km
Inclination	53°	53.2°	70°	97.6°	86.4°
Number of satellites	1584	1584	720	348/172	648
Operational (as of June 2023)	1495	1548	404	233/-	634

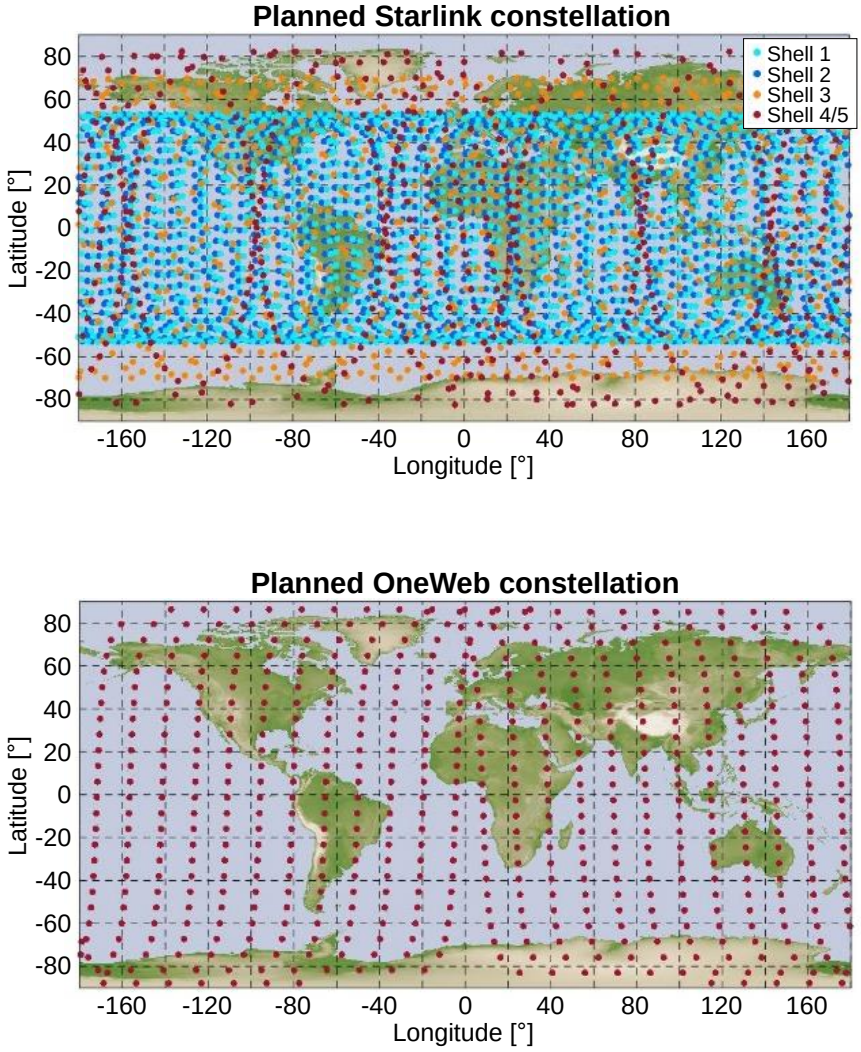

Figure 5.2: Starlink and OneWeb planned satellite constellations for a specific point in time represented on an equirectangular projection.

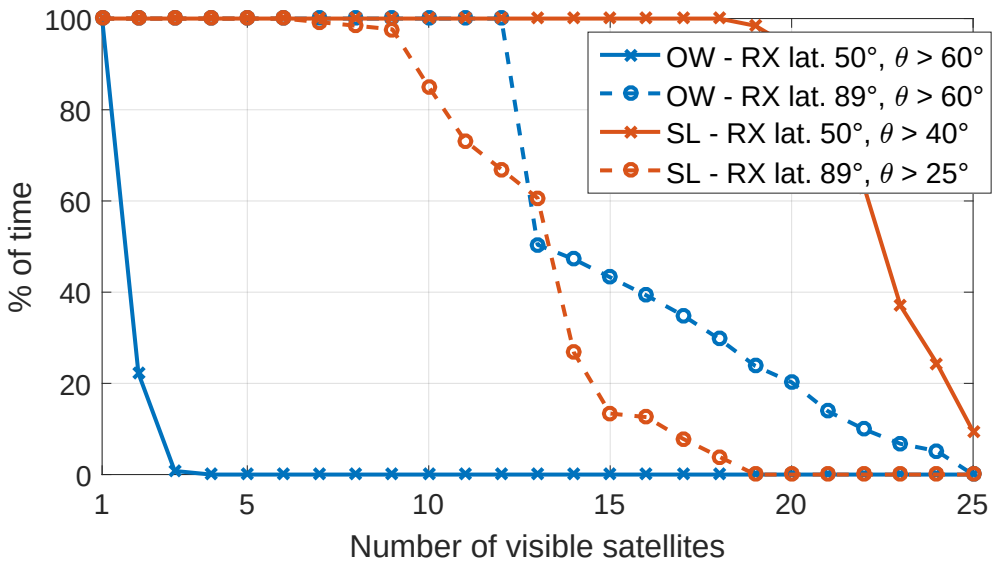

Figure 5.3: Percentage of time as a function of the number of visible satellites for the OneWeb (OW) and Starlink (SL) planned constellations considering receivers placed at 50° and 89° latitudes and the minimum elevation angles θ specified in the corresponding applications.

in a higher number of visible satellites in polar regions while Starlink constellation has a higher number of available satellites in mid-latitudes.

To provide broadband Fixed Satellite Services (FSS), Starlink and OneWeb satellites maintain bidirectional links, shown in Figure 5.4, with user terminals at X/Ku band and with gateways at Ka band using left-handed or right-handed circular polarization (LHCP or RHCP). Figure 5.5 shows their frequency plan [Spa16; Wor20], noting that user-downlink signals, which are considered as potential candidates of illumination of opportunity for passive radar, cover the 10.7 – 12.7 GHz band, which is also the allocated band for DVB-S satellites deployed at geostationary equatorial orbits (GEO).

The user-downlink band is divided into 250 MHz channels, which Starlink satellites, thanks to their onboard phased array antenna, use to realize a hexagonal cell deployment with simultaneous steerable and adaptable spot beams of approximately 2.25° -3 dB-beamwidth [Spa16]. On the other hand, OneWeb satellites have 16 user-downlink non-steerable spot beams arranged linearly in the South-North direction with highly elliptical patterns of 50° x 3.12° -3 dB-beamwidths. To avoid interference between spot beams, both constellations use

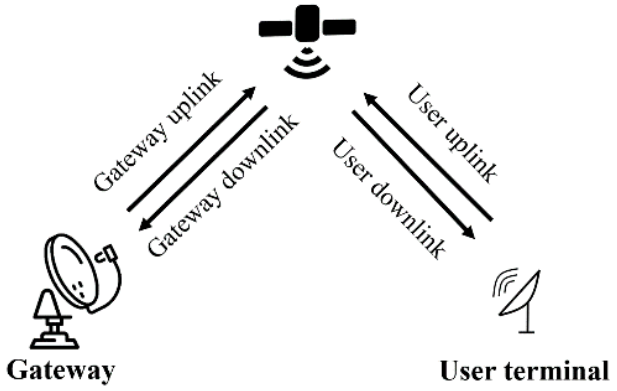

Figure 5.4: Bidirectional links for broadband LEO communication satellites.

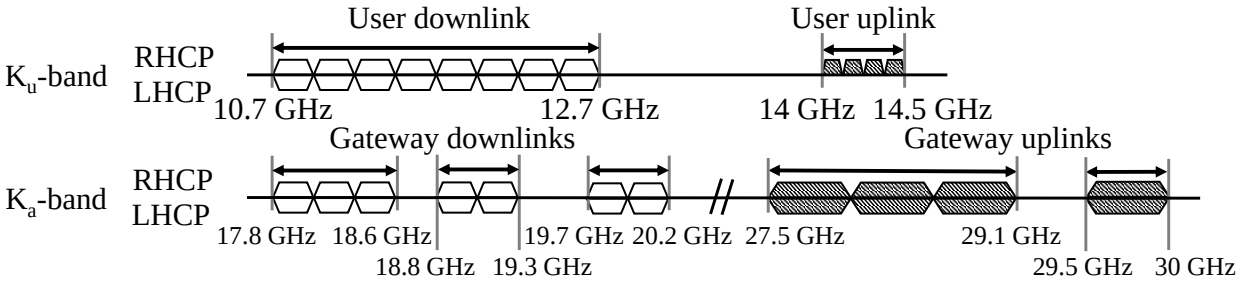

Figure 5.5: Frequency plan of Starlink and OneWeb communication satellites.

different frequency channels for adjacent beams. These illumination patterns are schematically represented in Figure 5.6 and Figure 5.7 for Starlink and OneWeb satellites, respectively.

Starlink satellites adapt the effective isotropic radiated power (EIRP) density of their spot beams between -56.2 dBW/Hz (at nadir) and -52.8 dBW/Hz (at maximum offset) in order to compensate the additional propagation losses when increasing the distance to the Earth surface in the pointing direction. OneWeb satellites have a maximum EIRP density of -49.4 dBW/Hz, which gives rise to a similar power flux on Earth surface for both constellations, since OneWeb satellites are at a higher altitude.

Although, detailed information about the physical layer of the user downlink is not publicly available, based on measurements and other published works [Hum23], it is noted that Starlink satellites use Orthogonal Frequency-Division Multiplexing (OFDM) modulation, while OneWeb user-downlink transmissions are based on Single Carrier-Time Division Multiplexing (SC-TDM). However, their experimental characterization for passive radar applications in terms of the ambiguity function is presented in Section 5.6.

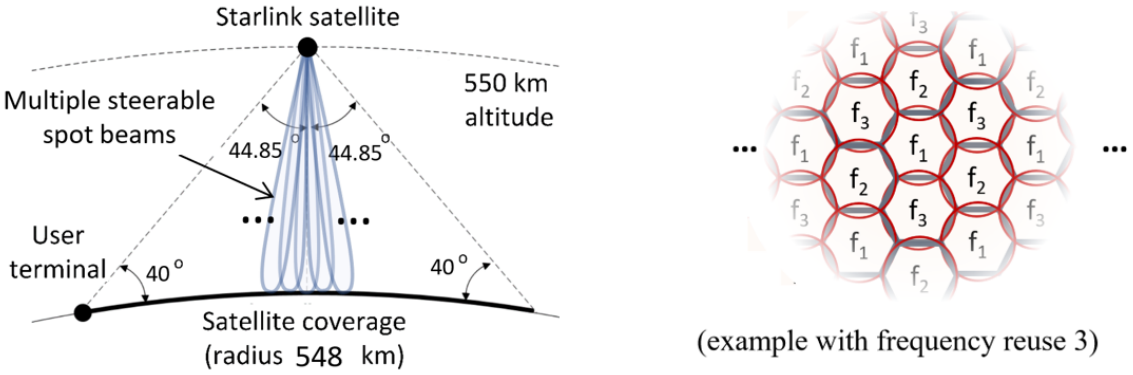

Figure 5.6: Illuminating spot beam patterns of a Starlink satellite with a cell deployment (left) and an exemplary frequency reuse factor of 3 (right).

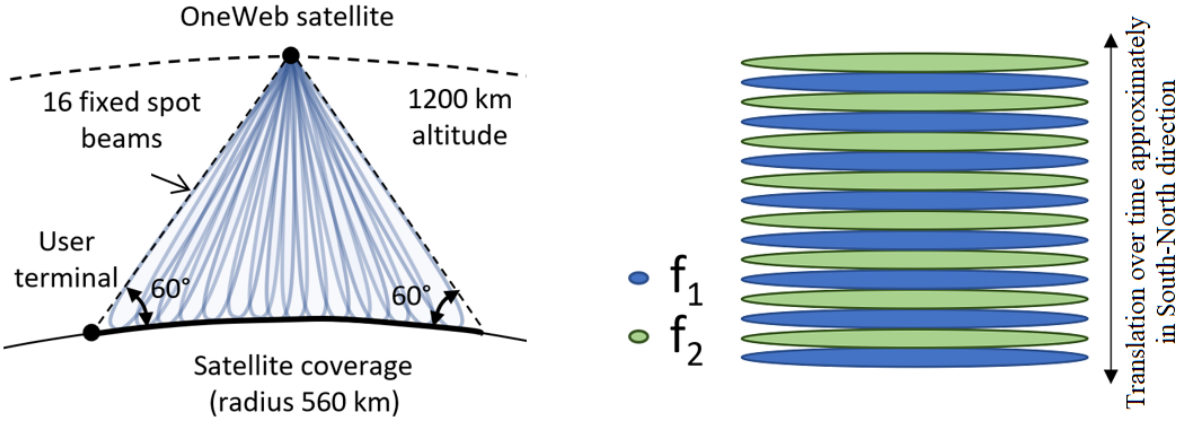

Figure 5.7: Illuminating spot beam patterns of a OneWeb satellite showing 16 fixed beams with respect to the satellite body reference system (left) and exemplary frequency reuse factor of 2 (right).

5.3 Passive radar system architecture

Based on the common architecture of passive radar systems composed of a reference channel to receive a copy of the direct signal and a surveillance channel pointed towards the area of interest to receive the reflections on the targets, Figure 5.8 shows a proposed architecture to exploit satellite user-downlink signals for target detection applications based on the use of a satellite tracking reference antenna.

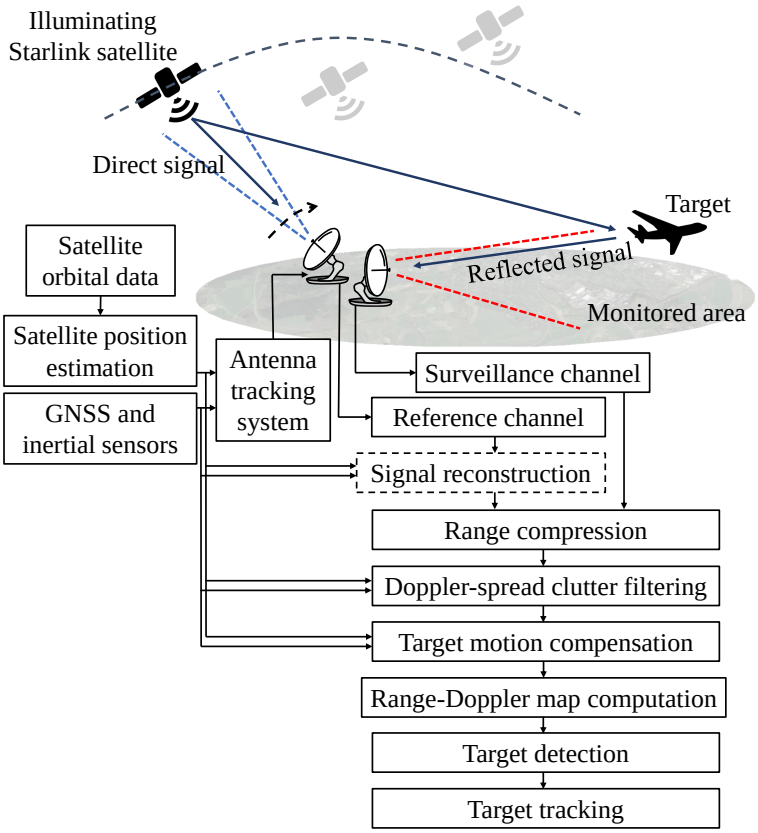

Figure 5.8: Proposed passive radar system architecture for target detection applications.

In order to receive the reference signal with enough SNR to effectively apply signal processing algorithms based on the cross-correlation between the reference and surveillance signals, a high-gain narrow-beam antenna is required to track the illuminating satellite. The inputs of the tracking system are the location and attitude of the receiving platform, measured with dual GNSS and inertial measurement unit (IMU) sensors, and the estimated satellite position computed for example with the SGP4 model (Simplified General Perturbation 4) [Val01] from the orbital parameters in Two Line Element (TLE) format, which are regularly updated. In this way, the mechanically or electronically steerable reference antenna can be

pointed in azimuth, elevation and polarization skew towards the direction of the illuminating satellite after applying multiple coordinate system transformation, schematically shown in Figure 5.9, to transform the estimated satellite position from Earth-fixed coordinate system to the antenna-body coordinate system, represented in Figure 5.10. The attitude of the antenna body can be measured with high performance dual GNSS/IMU sensors, which also enable the operation on moving platforms. Alternatively, in a GNSS-denied scenario, the antenna body orientation can be calibrated by resorting to GEO satellites with a known position, such as those broadcasting DVB-S signals. In this latter case, in order to improve the accuracy of this attitude calibration, several DVB-S satellites can be sequentially considered. The exploitation of GEO DVB-S satellites in this context is particularly convenient as their broadcast signals are transmitted in the same frequency bands of Starlink and OneWeb user-downlink signals and, therefore, this calibration step can be performed without the need for additional hardware.

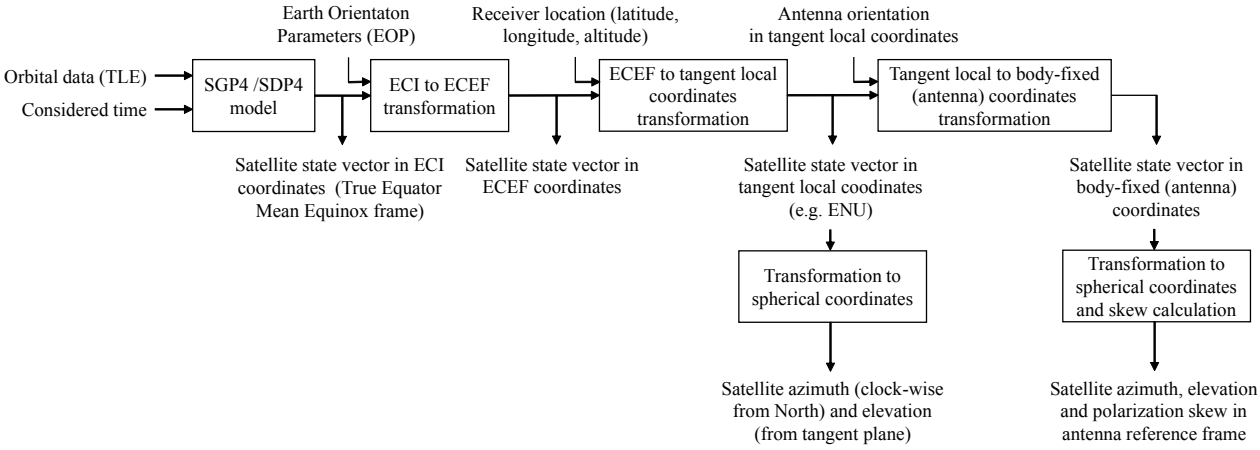

Figure 5.9: Diagram with computation steps to estimate satellite azimuth, elevation and skew in the antenna-body coordinate system from TLE data. SGP4 = Simplified General Perturbations 4, SDP4 = Simplified Deep Space Perturbations 4, ECI = Earth Center Inertial, ECEF = Earth-Centered Earth-Fixed, ENU = East, North, Up.

When the LEO satellite tracked with the reference antenna is no longer visible or stops transmitting towards the area where the passive radar receiver is located, it is necessary to switch the antenna pointing to start tracking a subsequent illuminating satellite. However, since these constellations are designed to maintain a continuous communication with low latency, handover protocols between satellites are implemented and, therefore, the illumination of the area is not expected to be interrupted because of the requirement to switch between

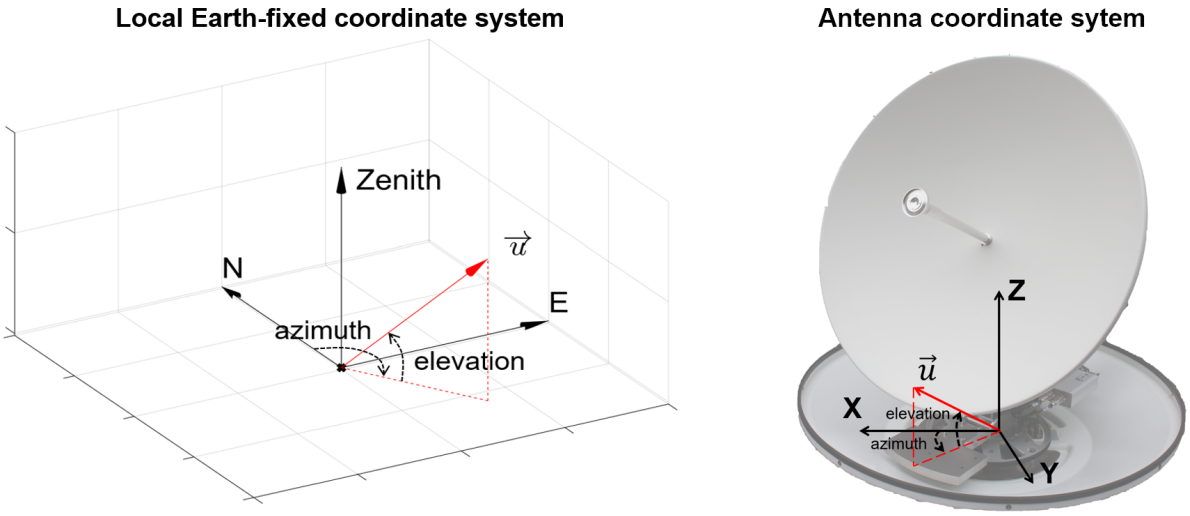

Figure 5.10: Diagrams of the considered local Earth-fixed coordinate system at the position of the antenna (left) and of the body-fixed antenna coordinate system (right), showing the considered definition of azimuth and elevation of the pointing direction $\vec{u}$ in each coordinate system.

satellites. Besides, if only a single reference channel is available, the use of an electronically steerable antenna is preferable in order to perform the satellite switching with practically no interruption of the continuous operation of the suggested passive radar.

Regarding the signal processing for target detection applications, after coherently digitising both reference and surveillance channels, the range compression is applied by computing the cross-correlation between both channels. In order to ideally reconstruct a noise-free reference signal, the direct signal can be demodulated and remodulated based on blind demodulation algorithms for OFDM signals in the case of Starlink, as the one specifically developed in [Hum23], or for SC-TDM signals in the case of OneWeb, requiring time and frequency synchronization. This required synchronization (i.e. start of symbols and, for OFDM, position of pilots) can be achieved for example by leveraging the synchronization sequences embedded in the transmitted signals obtained by reverse engineering based on cyclostationary analysis of experimentally acquired signals [Hum23]. However, the reconstruction step can be avoided with a limited loss of performance, also reducing the computational complexity of the signal processing, if the SNR of the reference signal is high enough (i.e. above 10 dB) [Cui15]. Besides, the usage of a narrow beam antenna for the reference channel greatly reduces the multipath components.

Given the dynamics of the LEO satellites, the clutter cancellation must consider the Doppler spread [Was19]. However, depending on the position and velocity of the moving targets, clutter signals might still hinder their detection, as their scattered signals may lie within the intra-clutter region. On the other hand, not only the movement of the target gives rise to range and Doppler migration effects, but also the movement of the satellites during the integration time. This issue is particularly relevant due to the fairly high bandwidths and carrier frequencies (in passive radar context) offered by Starlink and OneWeb signals. In order to coherently integrate and focus the target response for integration times in the order of hundreds of milliseconds or higher, the application of target motion compensation (TMC) techniques is required. However, for integration times shorter than one second and common linear target dynamics, a 1^{st} order TMC algorithm [Pig17] is appropriate to effectively integrate the target response, as shown in Subsection 5.5.4.

After the computation of the range-Doppler map, target detection can be performed by constant-false-alarms algorithms (CFAR), and estimations of the bistatic range and velocity of the detected targets can be computed. Considering the sequence of associated target measurements along the satellite pass, or measurements from different illuminating satellites (i.e. multistatic approach), target localization and tracking in Cartesian coordinates can be achieved by means of particle filtering or extended Kalman filter (EKF) [Gom22a]. Besides, when multiple satellites, for example from different constellations, are simultaneously illuminating the area but only one receiving reference channel is available, resource management methods, in order to select the reference satellite, can be applied to optimize the target localization and tracking performance. In this case, the use of an electrically steerable reference antenna is also preferred to allow the fast switching between illuminating reference satellites.

As previously introduced, the predictable trajectories of the satellites enable the application of imaging techniques based on synthetic aperture radar (SAR). In this case, a wide beam antenna (e.g. a horn antenna) is suitable for the surveillance channel in order to simultaneously image a wide area, compensating the decrease of the antenna gain with a longer integration time, which also improves the along-track resolution. Besides, as shown in Figure 5.11, if

several receiving surveillance channels are available, multiple spatial channels can be used to apply single-pass cross-track (e.g. for terrain elevation or displacement measurements) or along-track (e.g. for ground moving target indicator, GMTI) interferometry. It is important to note that the continuous illumination of the area of interest from different spatially diverse LEO satellites allows to get images persistently and from multiple illumination angles. Subsection 5.5.5 includes further discussion on the potential SAR imaging performance.

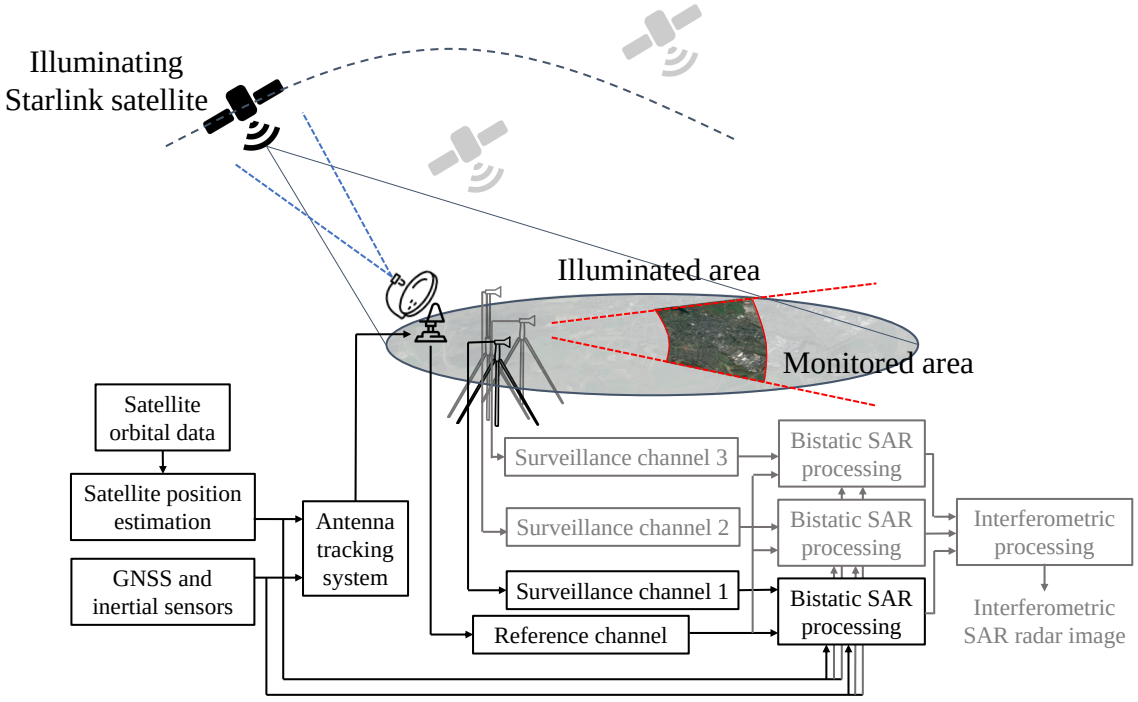

Figure 5.11: Proposed passive radar system architecture for imaging application including multiple surveillance channels (in grey) that enable the application of single-pass along- or cross-track interferometric techniques.

Based on the presented system architectures, passive radar prototypes have been developed in order to receive the signals transmitted by the considered LEO satellites and validate the proposed techniques.

5.4 Experimental passive radar prototypes

The SABBIA 2.0 system developed over the last years by Fraunhofer FHR is a high-resolution passive radar with antenna steering and satellite tracking capabilities that can operate with GEO DVB-S/S2 or LEO communication satellite signals in the 10.7-12.7 GHz band

[Sei22]. This high-performance and modular system includes four coherent channels with an instantaneous bandwidth of 625 MHz that can be flexibly used for surveillance/reference polarimetric or spatial channels, enabling the acquisition of up to two adjacent Starlink or OneWeb channels. Figure 5.12 depicts the SABBIA 2.0 front-end diagram for the low-band operation (i.e. 10.7-11.7 GHz) for one of the channels, while Figure 5.13 shows the rack including the system components. In order to enable the coherent operation of the channels, required for the passive radar signal processing, the GPS-disciplined 10 MHz reference for the Low-Noise Blocks (LNB) and the local oscillator for the IQ demodulators are shared between channels. Besides, the system implements an Automatic Gain Control (AGC) in order to efficiently exploit the full dynamic range of the 8-bit Analogue-to-Digital Conververters (ADC).

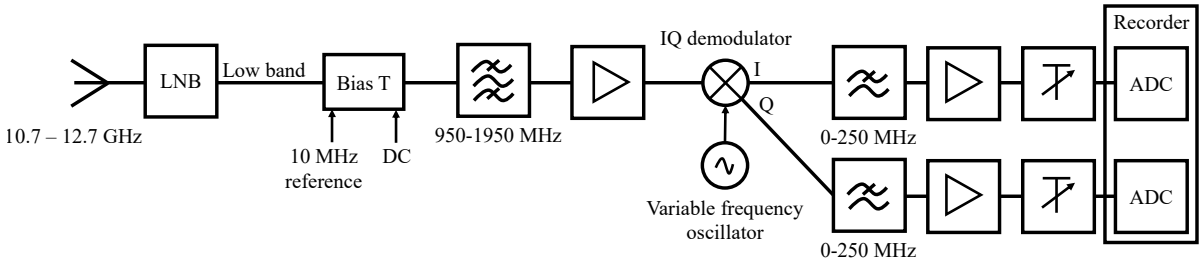

Figure 5.12: SABBIA 2.0 front-end block diagram for one of channel.

Figure 5.13: Rack of SABBIA 2.0 passive radar system including the front-ends, reference signal synthesizer, controlling units and recording computers.

Besides, an acquisition system mounted in a transportable 8U 19" rack, shown in Figure 5.14, based on the use of COTS SDR has been also developed. Figure 5.15 represents the system diagram which consists of an Ettus USRP X310 SDR with two UBX 160 daughterboards that simultaneously and coherently provide two receiving channels, i.e. one for the reference channel and one for the surveillance channel, covering frequencies between 10 MHz and 6 GHz with an instantaneous bandwidth of up to 160 MHz and an ADC resolution of 14 bits.

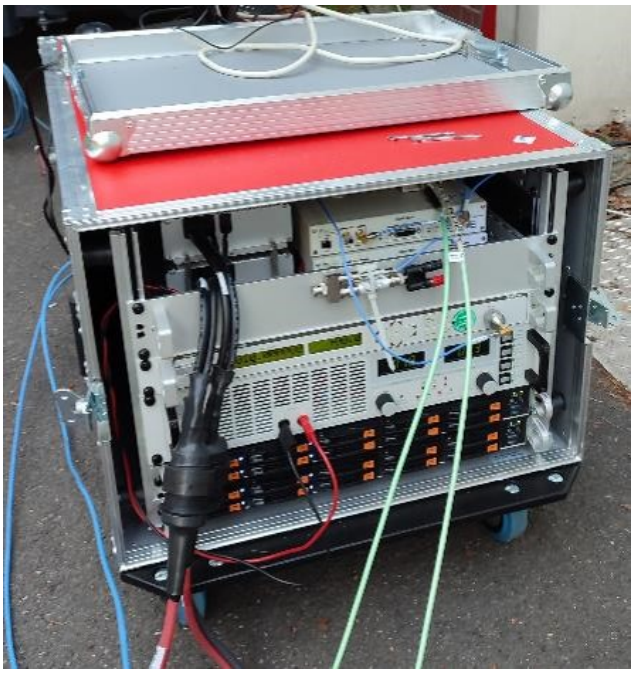

Figure 5.14: Portable 8U 19" rack including the USRP X310, reference signal generation, power supply and recording and control computer.

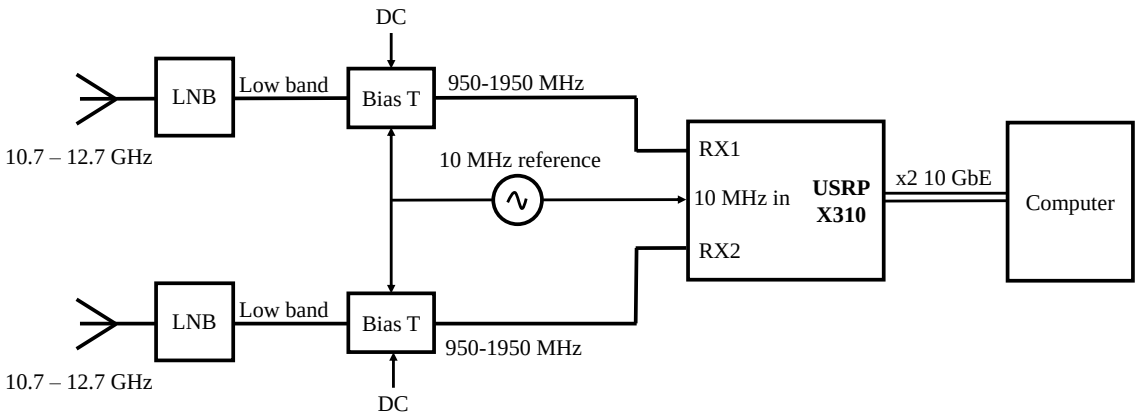

Figure 5.15: Block diagram of the developed system based on a COTS SDR, i.e. USRP X310, for the acquisition of signals transmitted by broadband communication LEO satellites.

For controlling the USRP and recording the digitised signals, the USRP is connected via two SFP-10G-T (Small Form-factor Pluggable 10 Gigabit Transceiver) and two Cat 7 Ethernet cables to a server computer A116TS-H11 from SuperMicro, which includes an AMD EPYC 7401p processor with 24 cores, 62.8 GB RAM and 8 TB of storage capacity in NVMe SSDs (Non-Volatile Memory Express Solid State Drives). For passive radar operation, a common 10 MHz reference signal obtained from a signal generator is shared between the USRP and the LNBs of both channels. This 10 MHz reference signal and the power supply (DC) for the LNBs are injected via the bias-tee. In this way, up to 160 MHz bandwidth of the intermediate frequency signals after the LNBs, which ranges from 950 MHz to 1950 MHz for the lower-band (i.e. 10.7-11.7 GHz) of DVB-S or LEO communication satellites, can be digitised. Although, this limited bandwidth does not allow the complete digitization of a broadband communication satellite channel (i.e. 250 MHz bandwidth), this system has been validated for the reception of the narrow-bandwidth pilots transmitted by Starlink satellites, which can be exploited for specific opportunistic navigation [Nei21a] or passive radar techniques [Cri23b], or to verify the reception of signals and the correct tracking of the satellites by steerable directional antennas.

Several antenna options, shown in Figure 5.16 are available with characteristics suitable for different applications. Among them, mechanically or electronically steerable antennas with high-gain narrow beams can be used thanks to ad hoc developments based on commercial antennas from EPAK [EPA] or Kymeta [Kym], respectively. While EPAK antennas allows the simultaneous reception of both orthogonal linear polarizations, Kymeta antennas present a low-profile suitable to be mounted on certain platforms (e.g. vehicles) and faster pointing switching. Besides, wider-beam horn antennas are also available to be used, mainly in the surveillance channel, when a fixed wide area is required to be covered for example in imaging applications or short-range wide area surveillance.

As already described, the reference channel antenna tracks the illuminating satellite to receive the direct signal with enough signal-to-noise ratio. This satellite tracking is achieved based on orbit propagator methods from the updated orbital data publicly available and by calibrating the orientation of the antenna body using reference DVB-S satellites. The example

(a) EPAK antennas

(b) Kymeta antennas

(c) Horn antennas

Figure 5.16: Antenna module options for the developed LEO satellite signal acquisition systems.

reception of OneWeb signals, shown in Figure 5.17, and further results of signal reception and characterization presented in Section 5.6 validate the proposed calibration method, the developed antenna control, and the possibility to track LEO satellites from their TLE orbital data using a narrow beam antenna with an approximate -3 dB-beamwidth of 2°.

These systems have been used to perform the experimental analysis of the Starlink and OneWeb user-downlink signals for passive radar applications and to validate the exploitation of these signals as illumination of opportunity in passive radar experiments

5.5 Theoretical analyses of achievable capabilities

5.5.1 Maximum detection performance and range resolution

Based on the characteristics of Starlink constellation and the parameters of the developed prototype, shown in Table 5.3, a power budget analysis is performed assuming free space propagation and perfect coherent integration in order to estimate the maximum detection range of the system for the two antenna configurations of the surveillance channel (high-gain narrow-beam or low-gain wide-beam). Figure 5.18 represents the SNR of targets on the Earth surface with respect to their distance to the receiver, while the SNR of the direct signal in the reference channel is estimated above 12 dB when a high-gain tracking antenna of 39 dBi is used. Besides, it can be noted that these results are approximately similar to the

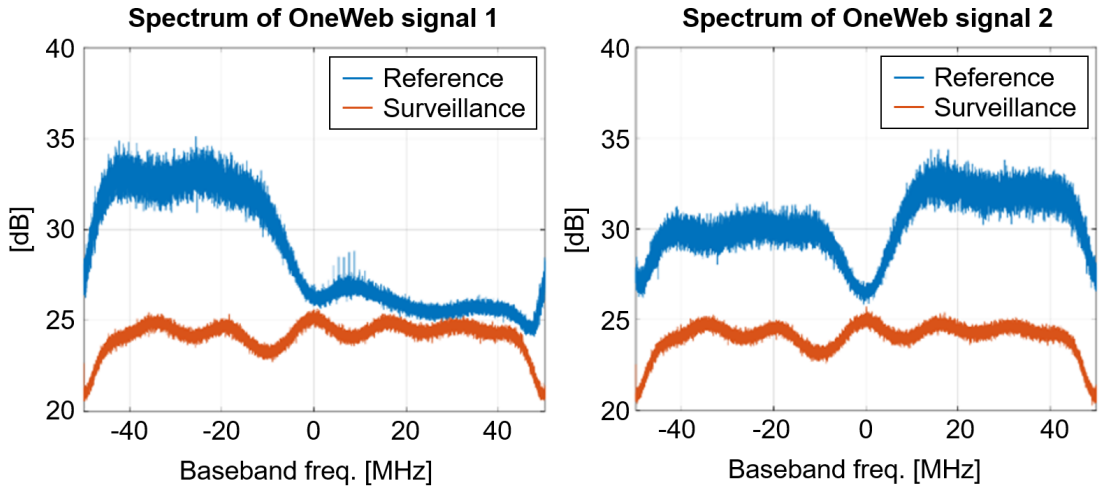

Figure 5.17: Exemplary spectra of received signals with the USRP X310-based system and Kymeta antennas at two different times while a OneWeb satellite was being tracked with the reference antenna. The USRP was configured to digitised a 100 MHz-bandwidth at the intermediate frequency of 1.45 GHz (i.e. the center frequency of the acquisition was set to 11.2 GHz given the first down-conversion performed by the LNB with a local oscillator at 9.75 GHz). Part of two adjacent OneWeb channels are therefore digitised.

Table 5.3: System parameters considered for the power budget analysis.

Parameter	*Value*
Frequency	11.7 GHz (user-downlink)
Bandwidth	240 MHz
EIRP density	-56.22 dB/Hz (Nadir)
Antenna gain (high/low)	39 dBi (dish) / 17 dBi (horn)
Noise factor	2 dB
Additional losses	4 dB
Integration time	0.5 s

ones obtained considering the OneWeb constellation as both Starlink and OneWeb satellites achieve an analogous power flux on the Earth surface.

As can be observed, with a high-gain surveillance antenna of 39 dBi gain, a 1 m^2 RCS target might be detected up to 1.9 km away from the receiver with a 90% probability of detection and a 10^{-4} probability of false alarm, assuming a Swerling 3 (SW3) target and a Neymann-Pearson detector [Ric14]. However, the narrow beam of approximately 2° considerably limits the instantaneous field-of-view and, therefore, a scanning of the area of interest is necessary. But,

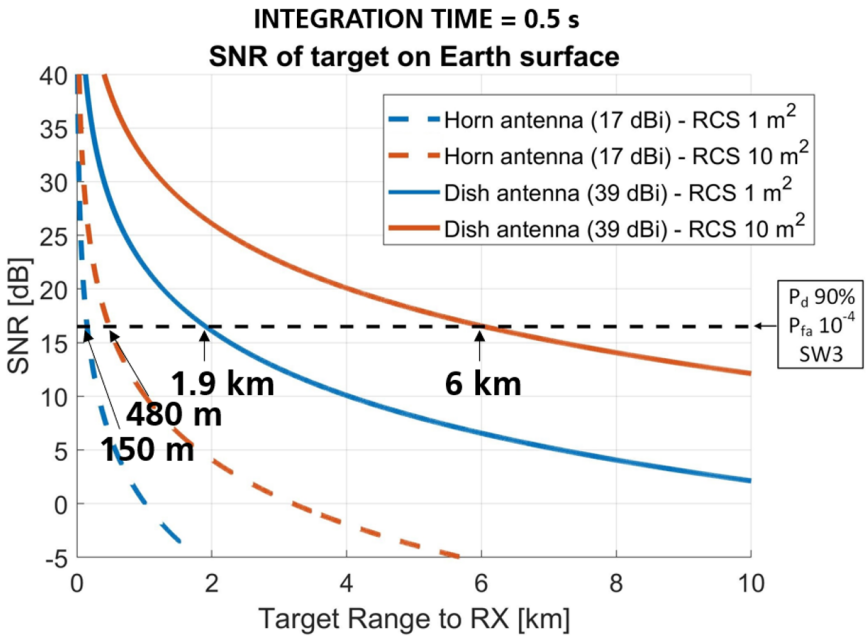

Figure 5.18: Estimated SNR for ground targets of different radar cross sections (RCS) (1 m^2 or 10 m^2) based on their distance to the receiver (RX), considering the two antenna configurations of the surveillance channel (high-gain narrow beam, i.e. dish, and low-gain wide beam, i.e. horn).

a 360° scan for only one elevation angle would require 90 s, which might not be operationally suitable in many application scenarios.

On the other hand, the use of a low-gain wide-beam antenna of 17 dBi gain reduces the maximum detection range of a 1 m^2 RCS target to only 150 m. Although increasing the integration time is suitable for imaging SAR applications, this might not be effective and feasible for target detection as more complex target motion models and compensation algorithms need to be considered. However, the future development of compact, low cost and wide bandwidth digital array receivers at X band may overcome this issue by enabling the generation of simultaneous narrow beams and increasing the full instantaneous field-of-view [Gom22b].

Nevertheless, it has to be noted that the power flux on Earth surface of Starlink and OneWeb user-downlink signals is approximately -98 dBW/m^2, which is considerably higher than the one achieved by DVB-S GEO satellites and GNSS signals [Cri10]. As examples, for an Astra-1KR transponder, the estimated power flux on Earth surface is about -108 dBW/m^2, while for the global positioning system (GPS) L1 signal, it is -140.5 dBW/m^2. Therefore,

the passive radar system based on the novel LEO communication satellites is expected to achieve better detection ranges than the already experimentally-validated passive radar based on other satellite illuminators of opportunity.

Since the transmitter-ground target distance is much longer than the considered target-receiver distances, a 10 dB increase in the SNR (e.g. by considering larger target RCS) results in a detection range improvement by a factor of about 3. However, in relation with the maximum detection ranges, the illumination pattern of the satellites also needs to be considered because, in order to retrieve the reference signal and apply the cross-correlation processing, both the reference channel receiver and the target have to be illuminated by the same spot beam.

With the objective to estimate the size of the Starlink spot beam footprints on Earth surface, Figure 5.19 shows the results obtained by simulating a planar square phased-array antenna with a 2.25° -3 dB-beamwidth in broadside (nadir) direction [Spa16] to carry out a hexagonal cell deployment with fixed cell centers on Earth surface around the area centered at 50.5°N, 7.38°E. Two different satellite locations are considered along a satellite pass. The practically elliptical footprints change during the satellite pass due to the beam widening behaviour of phased-array antennas when pointing away from broadside direction, and to the distance and incident angle variations. However, the minor axis of Starlink spot beam -3 dB-footprints is always longer than 20 km. Since OneWeb satellites have wider highly elliptical beams and a higher altitude, their spot beams have a larger footprint on Earth surface of about 1100x70 km.

The achievable range resolution on the Earth surface is time-varying and depends on the position of the illuminating LEO satellite and the receiver. Considering a 240 MHz channel bandwidth, two Starlink satellite positions (i.e. altitude 550 km) with different satellite elevation angles along one pass and a receiver placed at Fraunhofer FHR (50.617°N, 7.132°E), Figure 5.20 represents the range resolution on Earth surface in the orthogonal direction of iso-range contours. As can be observed, when the satellite is in a low elevation position, the area between the satellite and the receiver (i.e. around the projection of the baseline on the Earth surface) presents a diminished resolution, while the area around the extended baseline

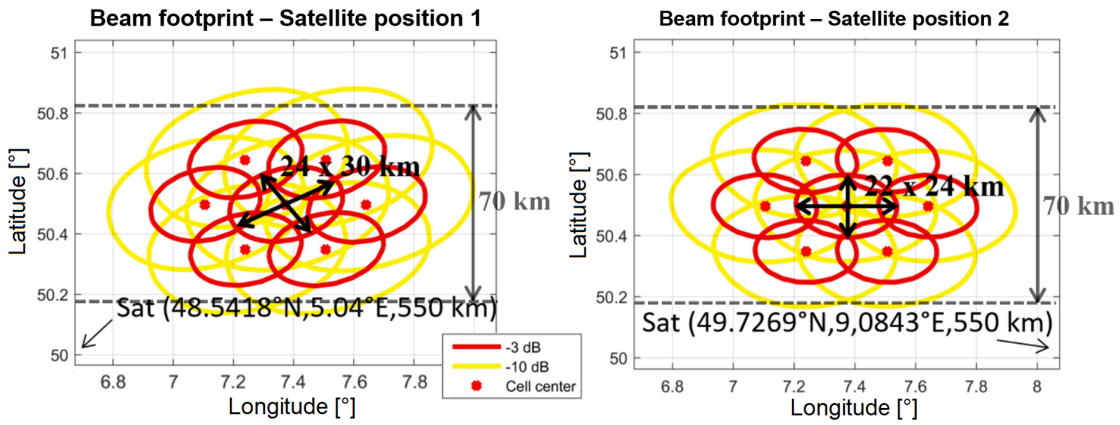

Figure 5.19: Spot beam footprints at -3 dB and -10 dB for two positions of a Starlink satellite (with 53° inclination orbit) considering a rectangular phased array antenna with a -3 dB-beamwidth of 2.25° at broadside (nadir). In order to compare with the size of a OneWeb beam footprint, a 70 km width associated with the -3 dB-beamwidth of a OneWeb beam in the South-North direction is shown in grey.

(i.e. beyond the receiver) presents a pseudo monostatic configuration with a resolution close to 0.6 m. In contrast, when the satellite presents a high elevation angle (i.e. near-zenith position), the achievable range resolution on Earth surface is mostly uniform with a value around 1.25 m (i.e. the speed of light divided by the channel bandwidth). Therefore, although a high range resolution can be achieved, if several satellites are simultaneously illuminating the area of interest, an appropriate reference satellite selection should be done in order to optimize the range resolution where targets are expected.

5.5.2 Required tracking antenna azimuth and elevation rate

In order to continuously track the satellites with the reference antenna, the maximum tracking speed of the system should be greater than the maximum azimuth and elevation rate reached by the satellites during their passes. Figure 5.21 shows the analysis of an exemplary near-zenith pass of a Starlink satellite for a receiver placed at Fraunhofer FHR (50.617°N, 7.132°E) including the temporal evolution of the baseline length and Doppler frequency (for a 11.7 GHz transmitter center frequency) and the satellite's azimuth, elevation, azimuth rate and elevation rate.

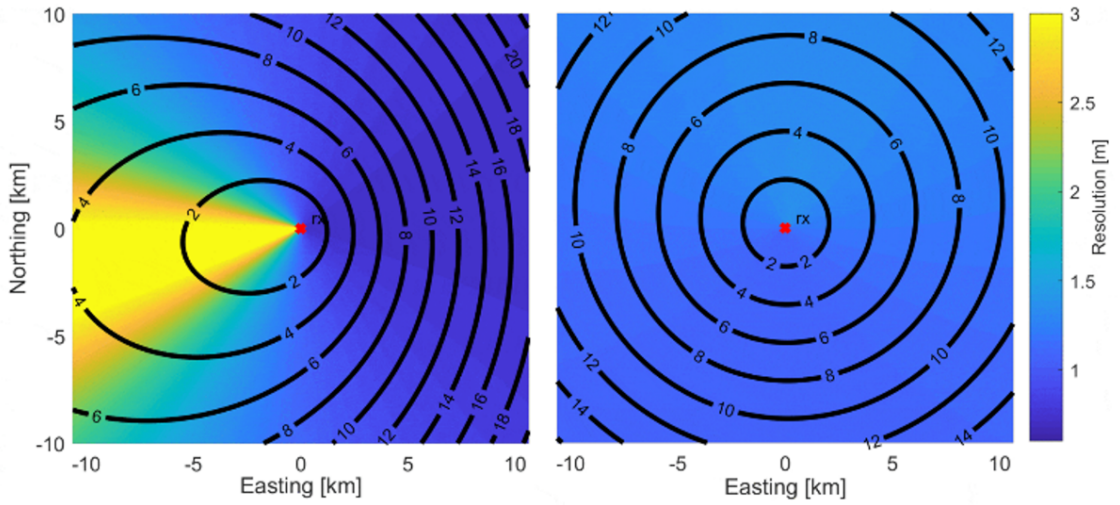

Figure 5.20: Achievable range resolution on Earth surface and iso-range contours (black curves, in km) for two positions of a Starlink satellite (with 53° inclination orbit) at 40° elevation angle (left) and close to 90° elevation, i.e. near-zenith position (right), and a receiver placed at Fraunhofer FHR.

The fast relative motion of the satellite is reflected in the high Doppler frequency of the direct signals. Besides, considering a minimum elevation of 40°, a near-zenith pass lasts around 2.7 minutes, other passes being of shorter duration. However, even for near-zenith passes, the required azimuth and elevation rate is limited to 5°/s which is completely feasible for current systems, including mechanical tracking systems. Both considered tracking antennas for the developed prototypes, i.e. EPAK and Kymeta antennas, meet this requirement.

5.5.3 Estimated accuracy of satellite position predictions

Using the methodology suggested in [Osw06], the position prediction confidence level of the SGP4 orbit propagator based on TLE data is approximately evaluated for Starlink LEO satellites. This method is based on the comparison of satellite positions propagated from previous and later TLE data with the position obtained by TLE data at their specific epochs without propagation. In this way, assuming uncorrelated errors in subsequent TLE data and low errors of the orbital parameters at the TLE epoch, the accuracy of the propagation method can be approximately assessed. This historical analysis is performed using TLE data provided by the 18$^{\text{th}}$ Space Control Squadron (SPCS) through space-track.org [spa] during one month.

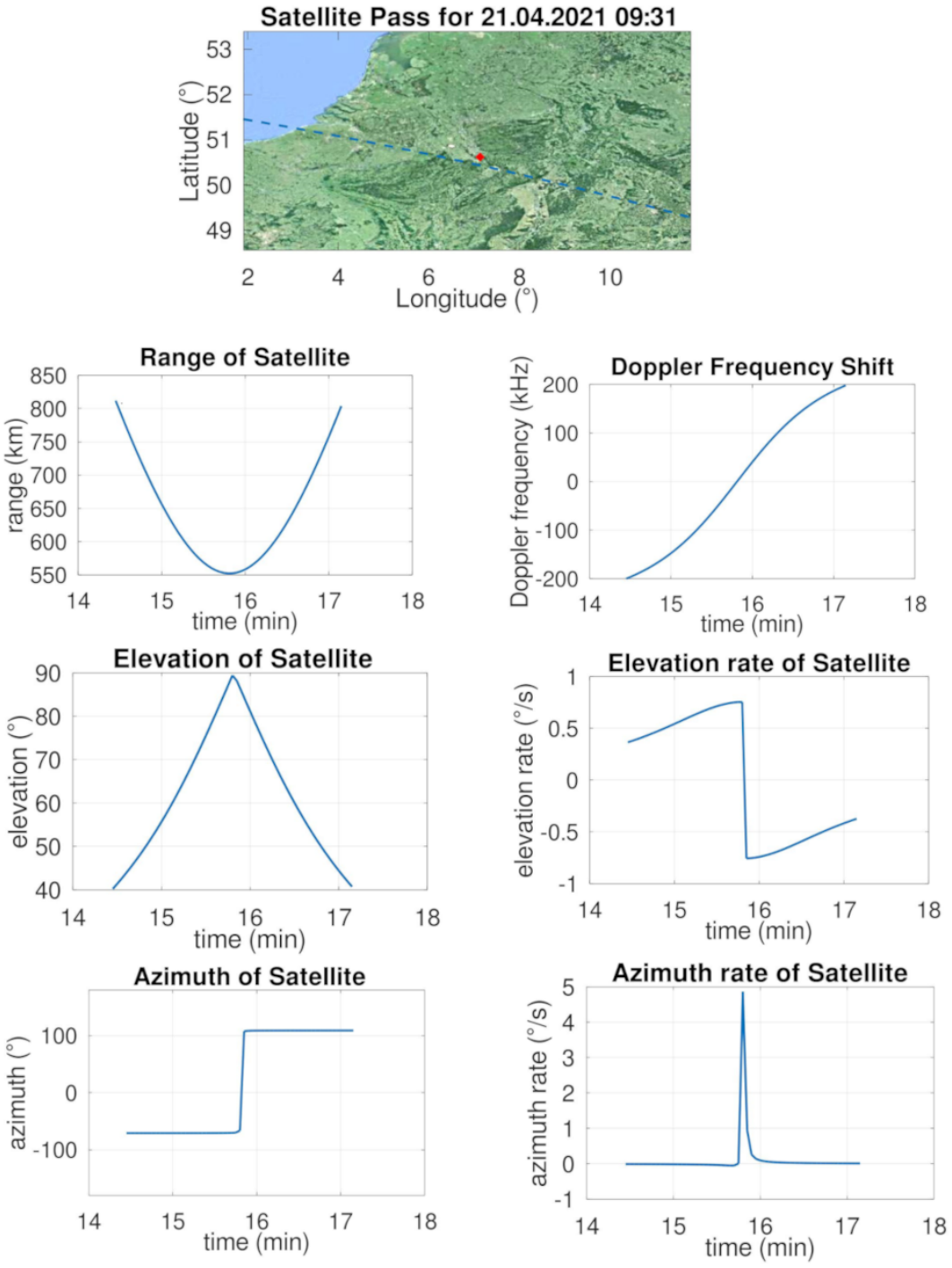

Figure 5.21: Analysis of a near-zenith pass of a Starlink satellite.

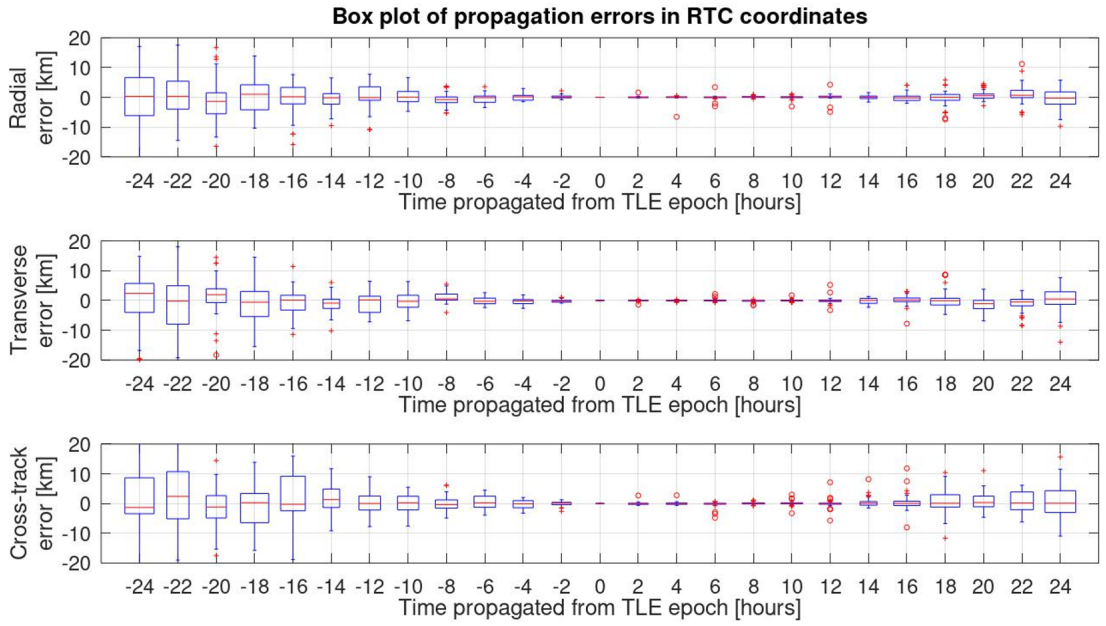

Figure 5.22: Box plots of satellite position propagation errors in RTC coordinates for the STARLINK-1007 satellite based on historical analysis of TLE data and using SGP4 propagation method.

As an example, Figure 5.22 shows the results for the operational satellite STARLINK-1007 with box plots for radial, transverse and cross-track (RTC) coordinate errors.

As can be observed, for a propagation time less than 15 hours, the error in transverse and cross-track coordinates are limited to approximately ±3 km which entail a pointing error of less than ±0.45°. Besides, supplemental TLE data are provided by CelesTrak [Cel], which are presumed to be more accurate as they are derived from the onboard positioning measurements and orbital data distributed by satellite operators. Therefore, taking into account that TLE data of the satellites of these LEO constellations are updated on average every 9 hours, the propagation of TLE data to predict the satellite positions can be considered a feasible method to track them even with a narrow-beam reference antenna.

However, some signal processing techniques for passive radar applications, e.g. imaging algorithms such as back-projection or Doppler radar tomography [Cri23b], would require a higher accuracy in the transmitter position estimation. Therefore, further developments of methods to improve the estimation of the transmitting satellite position, for example, based on the received Doppler frequency of pilot signals [Nei21b] or interferometric techniques [Nic22], are required.

5.5.4 Range and Doppler migration effects

The dynamics of LEO satellites give rise to fast changes of the bistatic geometry (i.e. bistatic range and Doppler frequency) that result in migration effects of the target response when the target bistatic range and Doppler frequency change more than the associated resolution during the integration time. In this case, if target motion compensation (TMC) techniques are not applied, the energy of the target is smeared throughout several resolution cells, and the achieved integration gain is diminished.

In order to compute the target migration, the following definitions of the bistatic range R_{bi} and Doppler frequency $f_{D,bi}$ have been considered, which include the effect of the dynamic baseline due to the movement of the satellite but assume a static receiver:

$$R_{bi}(t) = R_T(t) + R_R(t) - L(t) \tag{5.1}$$

$$\begin{aligned} f_{D,bi} = -\frac{1}{\lambda}\left[\frac{\partial}{\partial t}R_{bi}(t)\right] &= -\frac{1}{\lambda}\left[\frac{\partial}{\partial t}R_T(t) + \frac{\partial}{\partial t}R_R(t) - \frac{\partial}{\partial t}L(t)\right] \\ &= \frac{1}{\lambda}\left[(\vec{v}_{sat} - \vec{v}_{Tgt})\cdot\vec{u}_{Tx-Tgt} + \vec{v}_{Tgt}\cdot\vec{u}_{Tgt-Rx} - \vec{v}_{sat}\cdot\vec{u}_{Tx-Rx}\right] \end{aligned} \tag{5.2}$$

where $R_T(t)$ is the time-dependent transmitter-to-target distance, $R_R(t)$ is the time-dependent target-to-receiver distance, $L(t)$ is the time-dependent baseline length (i.e. transmitter-to-receiver distance), λ is the wavelength associated with the center frequency of the transmitted signal (taken as 11.7 GHz in the performed analyses), $\vec{v}_{sat}$ is the three-dimensional velocity vector of the satellite, $\vec{v}_{Tgt}$ is the three-dimensional velocity vector of the considered target (null for static clutter), $\vec{u}_{Tx-Tgt}$ is the unitary vector in the direction from the transmitter to the target, $\vec{u}_{Tgt-Rx}$ is the unitary vector in the direction from the target to the receiver, and $\vec{u}_{Tx-Rx}$ is the unitary vector in the direction from the transmitter to the receiver.

Figure 5.23 shows the bistatic range and Doppler migration undergone by a stationary ground target as a function of its position around a passive radar receiver placed at Fraunhofer FHR for an integration time of 1 s and a near-zenith Starlink satellite position along its trajectory.

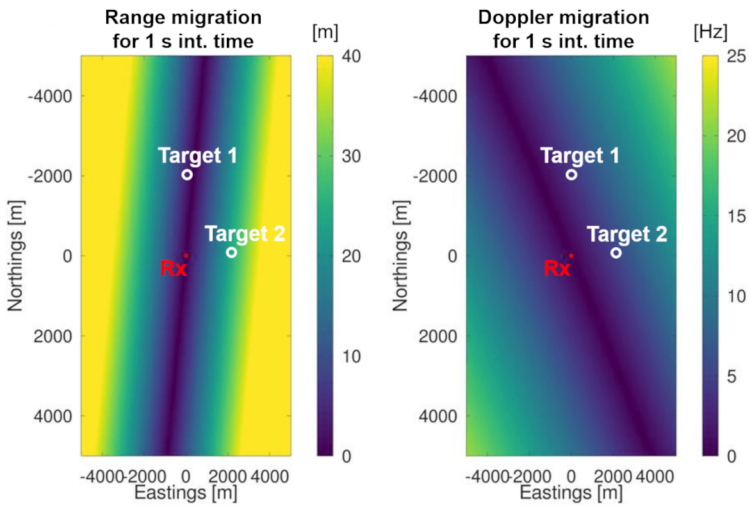

Figure 5.23: Bistatic range and Doppler migration of a stationary ground target as a function of its position around a receiver placed at Fraunhofer FHR for an integration time of 1 s and a near-zenith Starlink satellite position. Target 1 and Target 2 mark the positions analysed in Fig. 5.24.

In addition, for the same satellite position, Figure 5.24 represents the bistatic range and Doppler migration as a function of the integration time for two specific target locations (i.e. [0 , 2000] m and [2000 , 0] m in Cartesian coordinates with respect to the receiver position). As expected, large bistatic range and Doppler migration levels occur, which significantly limit the integration time if TMC approaches are not considered. Given the high range resolution of the system, even the response of static ground scatters may cross several range resolution cells for integration times shorter than 0.1 s.

It should be noted that, in general, higher range migration levels occurs for high elevation angle positions in lower altitude orbits. Therefore, the use of OneWeb satellites transmission generally results in lower target migration effects. Besides, if multiple satellites are illuminating the area of interest, the selection of the reference satellite can be made in order to achieve a favourable geometry that decreases the range and Doppler migration effects in a specific zone.

To analyse the applicability of TMC algorithms by simulating a scenario based on the signal model described in Equations 2.14 and 2.15, Figure 5.25 shows a comparison of range-Doppler maps obtained without TMC and applying a 1st order TMC algorithm based on Keystone transform [Pig17] for a coherent integration time of 0.5 s, a stationary ground target located

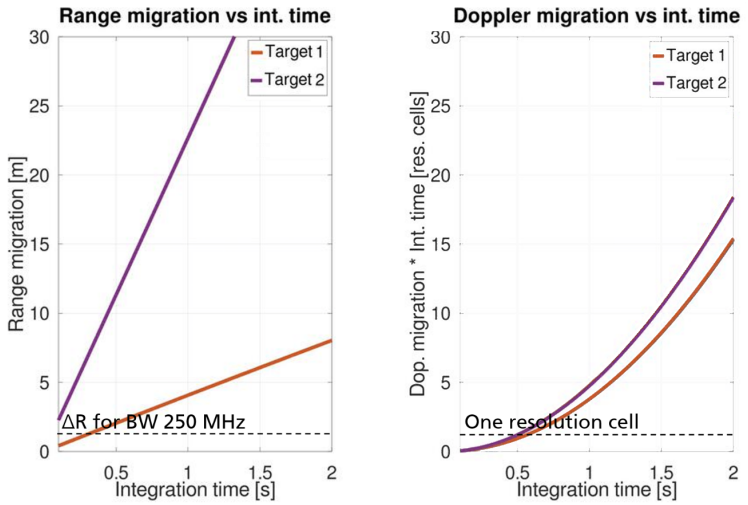

Figure 5.24: Bistatic range and Doppler migration as a function of the integration time for two static ground targets at $[0\,, 2000]$ m and $[2000\,, 0]$ m in Cartesian coordinates with respect to the receiver placed at Fraunhofer FHR, and a near-zenith Starlink satellite position.

at $[0\,, 2000]$ m with respect to the receiver and the satellite location and orbit represented in Figure 5.26.

As can be observed, without TMC, the energy of the target is spread throughout several resolution cells preventing target detection for low input SNR levels. However, since the target mainly undergoes range migration, a 1^{st} order TMC approach is appropriate to focus the target, achieving enough integration gain to enable its detection for both the input SNR levels considered (-40 dB and -60 dB). Longer coherent integration times and more distant or moving targets may require 2^{nd} order TMC algorithms to additionally compensate for the induced Doppler frequency rate.

5.5.5 SAR and polarimetric modes

The predictable dynamics of the satellites enable the application of SAR techniques in order to focus the response of static ground scatters and obtain an image of the area improving the cross-range resolution. However, as shown in Figure 5.27, different satellite positions along the trajectory (i.e. different bistatic geometries) give rise to different iso-range and iso-Doppler curve patterns. Therefore, some bistatic geometries are favourable to increase the cross-range resolution in certain areas of the scenario, usually when iso-range and iso-Doppler curves are

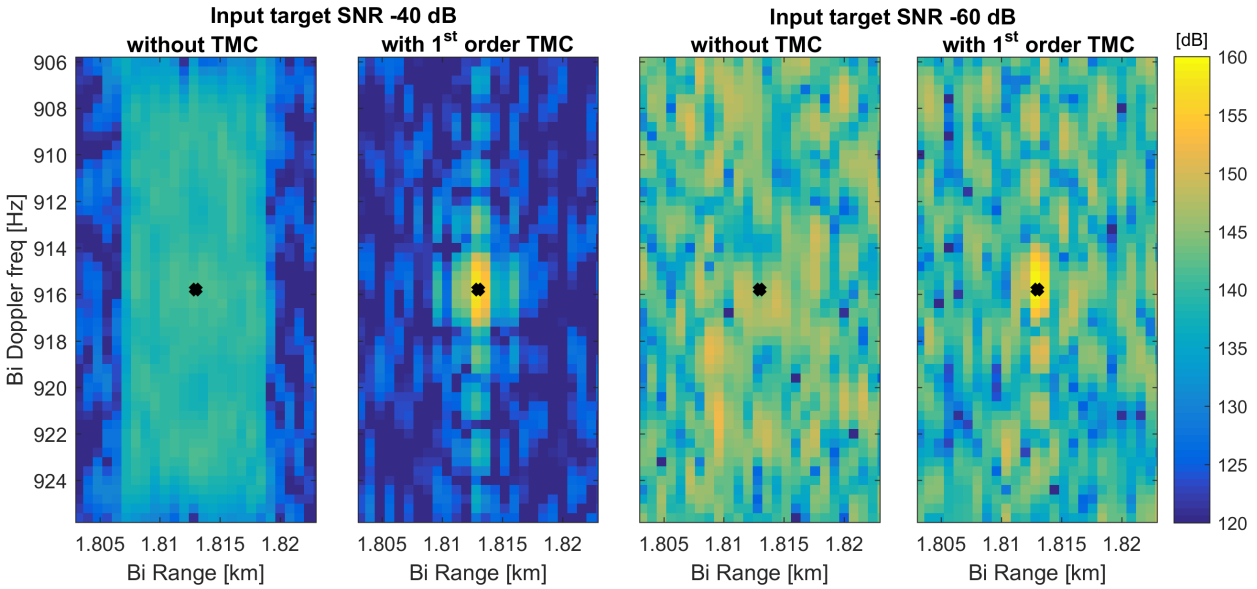

Figure 5.25: Range-Doppler (RD) maps obtained with no TMC and with a 1st order TMC algorithm. A coherent integration time of 0.5 s is considered for simulated scenarios composed of a stationary ground target located at $[0\,, 2000]$ m with an input SNR of -40 dB (left) and -60 dB (right) and the Starlink satellite position, shown in Figure 5.26, at 75° elevation angle from the receiver.

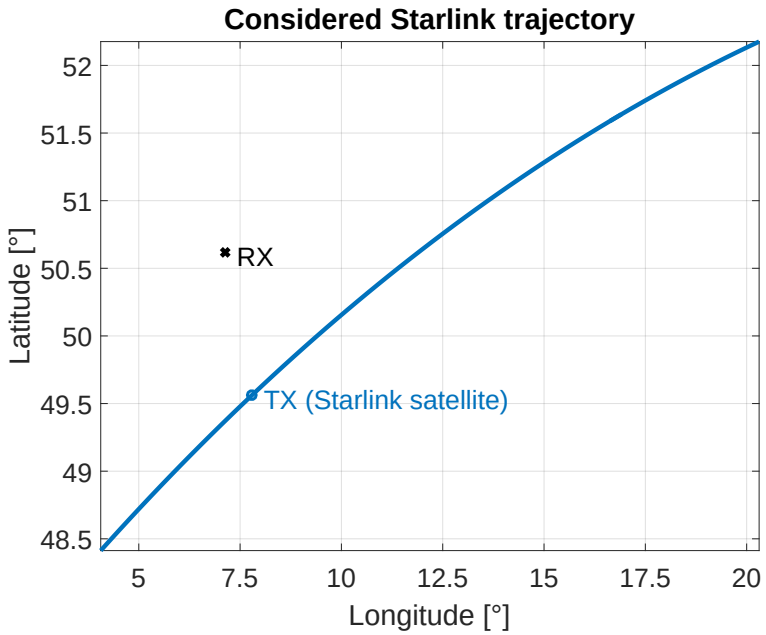

Figure 5.26: Considered Starlink satellite orbit and specific location, marked by a circle, for the range-Doppler map simulation with range and Doppler migration effects.

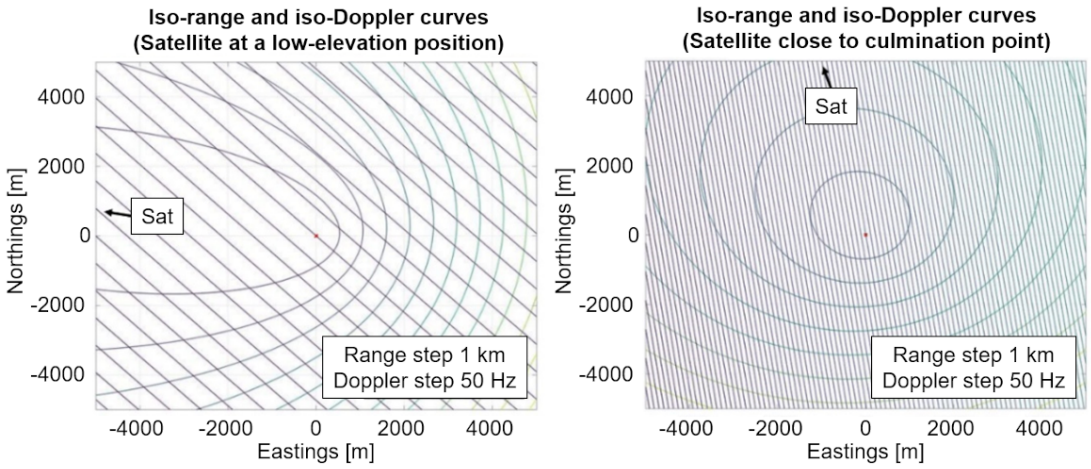

Figure 5.27: Iso-range (ellipses) and iso-Doppler (lines) curves for two exemplary geometries considering a trajectory of a Starlink satellite with 53° inclination when the satellite is at a low-elevation position (left) and when the satellite is near its culmination point, i.e. maximum elevation (right), for a receiver placed at Fraunhofer FHR.

nearly orthogonal. These geometries can be achieved, for example, when the satellite is near its culmination point (i.e. maximum elevation) and the imaging is performed in a side-looking configuration from the satellite track. Thanks to the different orbits, which provide a spatially diverse and multiangle illumination as shown in Figure 5.28, the reference satellite can be selected to achieve a favourable geometry for the area of interest.

Considering a zenith satellite location, Figure 5.29 represents an estimation of the achievable cross-range resolution on Earth surface (i.e. in the tangent direction to the iso-range curves) as a function of the coherent integration time at 5 km from the receiver for a side-looking imaging configuration. For this estimation, the transmitting synthetic aperture has been approximated as a linear array (i.e. linear satellite trajectory) with an approximate -3 dB-beamwidth given by $\Delta\theta_{3\,dB} = \frac{\lambda}{D}$, where λ is the wavelength associated to the center frequency of the signals (i.e. 11.7 GHz for the performed analysis), and D is the length of the synthetic array based on the velocity of the satellite and the integration time [Sho14]. This approximation is considered suitable based on the analysed integration times shorter than 10 seconds, and the distance to the satellites. It is also important to note that in this considered scenario, if the area of interest is limited to the side-looking region, the iso-Doppler curves are almost orthogonal to the iso-range curves, as similarly shown if the receiver is looking towards South in the bottom graph of Figure 5.27.

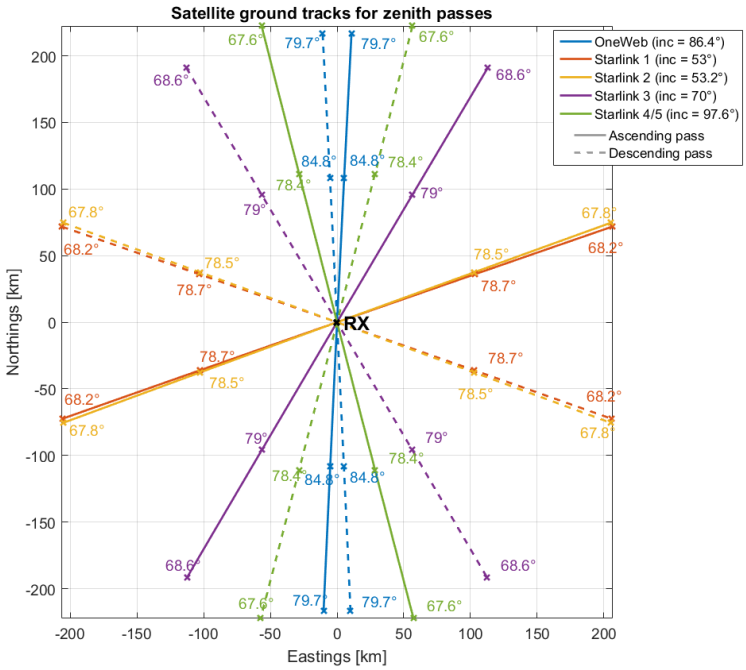

Figure 5.28: Satellite ground tracks for ascending and descending zenith passes of OneWeb and Starlink satellites of different constellation shells for a receiver (RX) placed at Fraunhofer FHR. The passes are represented for a duration of 60 s. The values inside the figure indicate the elevation of the satellite from the ground receiver located at (0,0) at the position of the markers, which are represented every 15 s (the markers associated to 30 s that lay over the RX are not represented for simplicity).

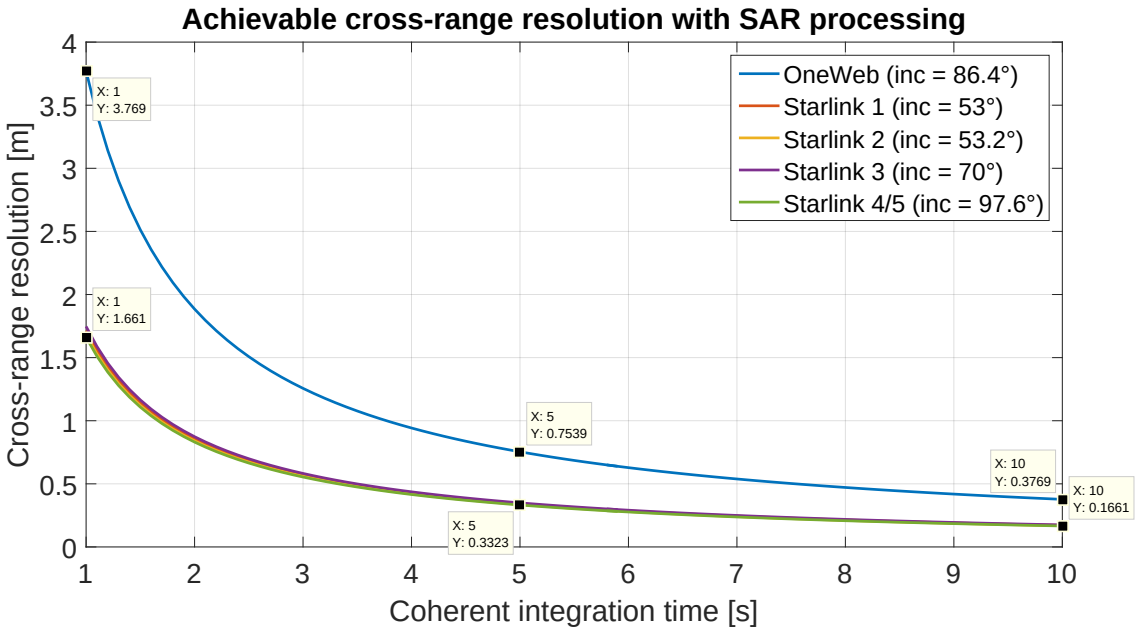

Figure 5.29: Estimated achievable cross-range resolution with SAR processing as a function of the coherent integration time for a side looking configuration and a zenith position of OneWeb and Starlink satellites, considering a receiver placed at Fraunhofer FHR. Similar side-looking cross-range resolutions are estimated for the different Starlink constellation shells and, therefore, their associate curves overlap.

As expected, the faster relative dynamics and lower altitudes of Starlink satellites give rise to a better achievable cross-range resolution. However, these estimations show that sub-meter cross range resolution might be achieved with both constellations as transmitters of opportunity. Nevertheless, to effectively achieve these resolutions the coherence of the target responses and the receiver must be guaranteed during the integration time. Besides, the trajectory of the reference satellite during the integration time needs to be estimated with a high accuracy in order to apply the back-projection algorithm. Although the propagation of the orbital data might not achieve the required level of accuracy, as shown before, methods based on the exploitation of the Doppler frequency of the received direct signal (e.g. beacon signals of Starlink) could be used to improve the trajectory estimation accuracy, apart from applying auto focus algorithms that compensate for residual motion errors in the SAR processing [Che21].

Since multiple simultaneous illuminating satellites are potentially available, the use of these dense satellite constellations as illumination of opportunity not only provides a multiangle

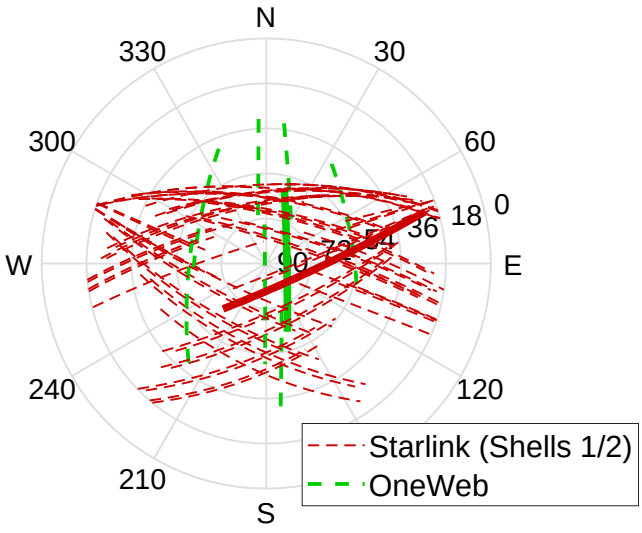

Figure 5.30: Sky plot of Starlink (shells 1 and 2) and OneWeb passes during two time intervals of 180 s, showing a complementary geometry between constellations. Solids lines are to compare a specific OneWeb pass with a Starlink pass.

illumination of the area, that can reduce shadows and increase spatial diversity, but also enable the application of multistatic SAR techniques, which may eventually extend the coverage or improve imaging resolution. A multistatic fusion approach for imaging applications based on the exploitation of the Starlink narrow-band pilot signals from multiple satellites, as a robust illumination of opportunity, applying Doppler radar tomography has been investigated in [Cri23b]. An additional approach is to consider the complementary geometries, shown in Figure 5.30, given by the orbits of OneWeb satellites (i.e. 86.4° orbit inclination), which pass in the South-North direction, and Starlink satellites from shells 1 and 2 (i.e. 53° and 53.2° orbit inclinations), which predominantly pass in the West-East direction. This multistatic geometry leads to different target bistatic range, bistatic Doppler frequency, bistatic angle and incident angle from the transmitter along time, as represented in Figure 5.31, providing the possibility to exploit spatial diversity thanks to the dense satellite networks deployed.

In addition to the multiangle illumination with spatial diversity, these novel illuminators of opportunity also allow the application of polarimetric methods. Both the multiangle illumination and polarization information may improve the target classification performance of the system [San21].

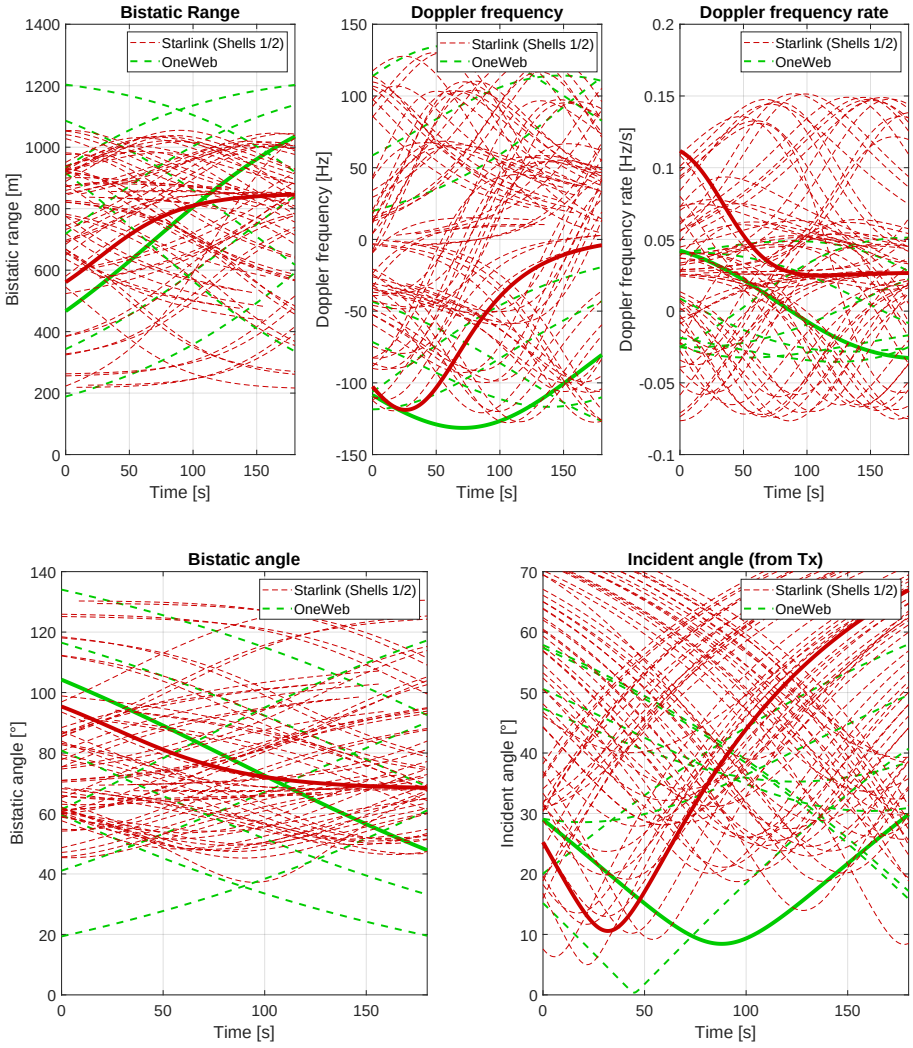

Figure 5.31: Bistatic range, bistatic Doppler frequency, bistatic Doppler frequency rate, bistatic angle and incident angle from the transmitter (with respect to surface normal) along time of an exemplary static target located 600 m South to the receiver at Fraunhofer FHR for the Starlink and OneWeb satellite passes shown in Figure 5.30. Solids lines are to compare a specific OneWeb pass with a Starlink pass.

Based on the available information, user-downlink signals may be transmitted in both orthogonal circular polarizations. If the reference and surveillance channels allow the digitization of two orthogonal polarization (horizontal and vertical or RHCP and LHCP) and the satellites simultaneously transmit pseudo-orthogonal signals in each orthogonal circular polarization, these signals could be separated in the receiver and exploited to get full-polarimetric information of the targets. However, even if the satellites transmit in a single circular polarization, the reception of the horizontal and vertical polarizations in the surveillance channel may allow the application of hybrid compact polarimetric techniques [Mun22; Kum23].

These analyses demonstrate the significant potential capabilities that these emerging illuminators of opportunity offer. Nevertheless, since these are proprietary systems and there is no available standard defining the physical layer, it is necessary to perform an experimental characterisation of the signals and to determine their properties and suitability for passive radar applications, mainly based on their ambiguity function, as presented in the following section.

5.6 Experimental signal characterization for passive radar applications

Using the developed receiving systems, Starlink and OneWeb signals were acquired in order to perform their experimental characterization and assess their properties for passive radar applications.

5.6.1 Starlink signals

In order to demonstrate that Starlink signals were being transmitted towards the area around Fraunhofer FHR (50.617°N, 7.132°E), the first experimental set-up for signal acquisition was a commercial LNB feed horn (model AK54-XT2) with linear polarization pointed towards zenith (i.e. 90° elevation) and connected to a receiving channel of an Ettus USRP X310 software defined radio with UBX 160 daughterboards. As this receiver configuration does not allow the digitization of a complete transmission channel (of approximately 250 MHz

bandwidth), only the central 10 MHz bandwidth of the channel centered at 11.325 GHz was digitised without any antenna polarization axis alignment since Starlink signals were expected to be circularly polarized.

During a 150 second signal recording, 32 Starlink satellites met the elevation angle requirement (i.e. greater than 25°) specified in the constellation application. However, as shown in Figure 5.32, only 4 satellites crossed the estimated 60° -3 dB-beam of the LNB feed horn during this signal acquisition. The computed spectrogram of the received signal centered at 11.325 GHz, shown in Figure 5.32, confirms the reception of Starlink beacon signals around the center frequency of the selected transmission channel. As can be seen, the received beacon signals follow the estimated Doppler frequency pattern based on the predicted trajectory of the satellites (overlaid as coloured lines), although they present a frequency shift possibly due to orbit propagation inaccuracies from TLE and a local oscillator frequency bias of the receiver as it was not GPS-locked during these measurements. These patterns also show the fast changes (approximately up to 3.4 kHz/s) of the Doppler frequency of the received signals during the passes due to the dynamics of the LEO satellites.

As can be seen in the spectrum represented in Figure 5.33, nine beacons or pilot signals are transmitted with 44 kHz separation between them. These beacons could be used to point the reference antenna towards the satellite and to estimate and compensate the frequency offset of the received signals.

These signals are received during a long-time interval while the satellite is passing. Therefore, they can be considered as an “always-on” signal whose transmission does not depend on the number of users connected to the network or to the network load. Although this kind of “always-on” signals is particularly suited to be used as illumination of opportunity for passive radars, in terms of availability and robustness, the narrow bandwidth of these beacons prevents their usefulness with common signal processing techniques. However, by exploiting the dynamic multistatic geometry of the transmitting network, the application of only-Doppler or Doppler radar tomography approaches can be considered [Cri23b].

Thanks to the enhanced instantaneous bandwidth of the developed SABBIA 2.0 passive radar system, a complete user-downlink transmission channel can be recorded, enabling the

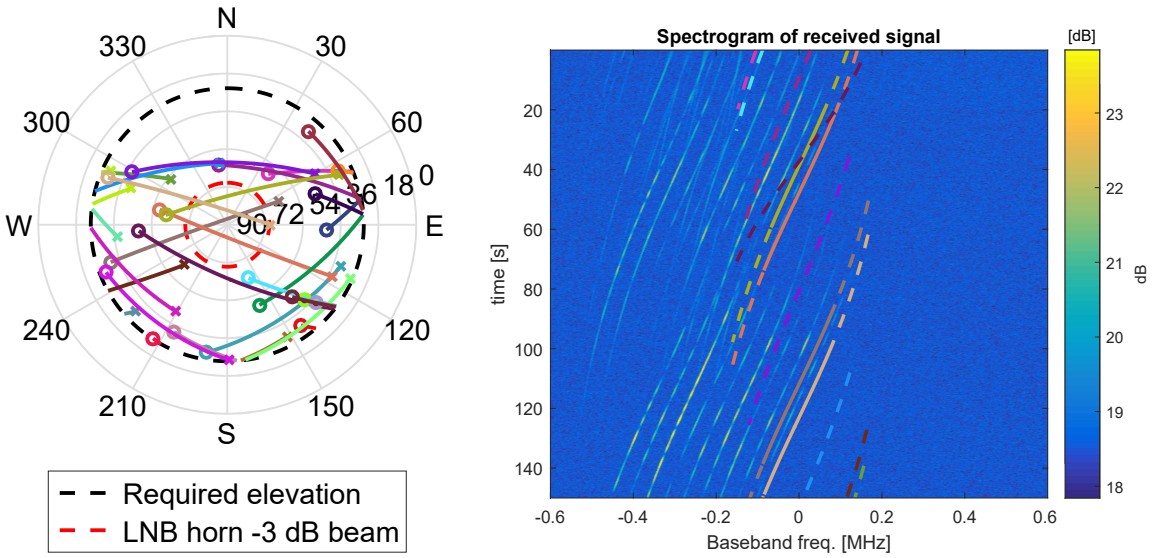

Figure 5.32: Sky plot of Starlink satellite passes (left) during a 150 second signal recording at 11.325 GHz center frequency with an LNB feed horn of 60° -3 dB-beamwidth pointed towards zenith connected to an Ettus USRP X310, and computed spectrogram of the received signal (right). The Doppler frequency of the satellites that present an elevation above 50° during the measurement are overlapped (dash line for elevation interval between 50° and 70° and solid line for elevation above 70°) maintaining the colors associated to each satellites for both the sky plot and the spectrogram.

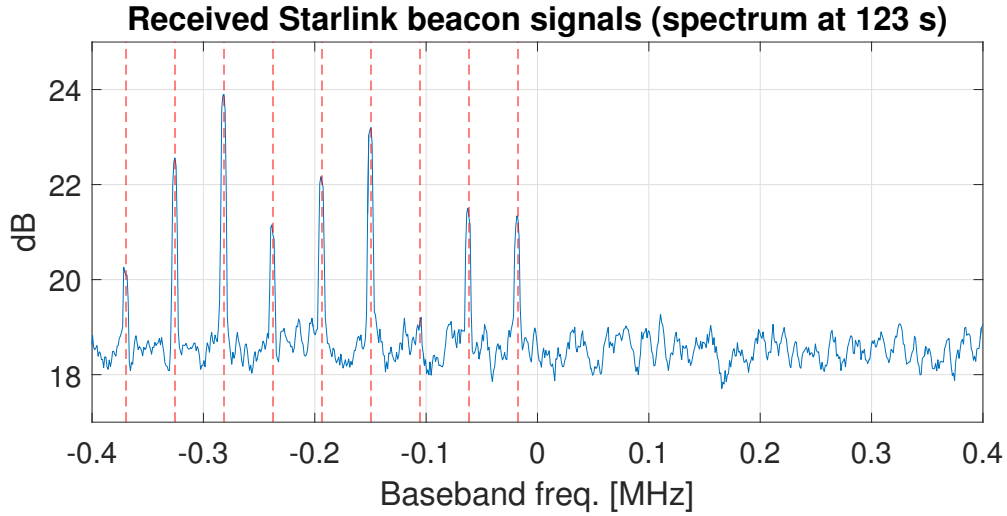

Figure 5.33: Spectrum of the received signal at 123 s showing the beacon signals around the center frequency of the transmission channel with 44 kHz separation between them.

signal characterization for passive radar applications. By tracking Starlink satellites with a high-gain reference antenna, i.e. EPAK or Kymeta antennas, based on the TLE orbital parameters of the satellites, transmitted signals were recorded and subsequently processed, also validating the feasibility of receiving LEO satellite signals with a narrow-beam antenna based on the position prediction from the TLE data, in accordance with previous accuracy analyses. During these measurements no Starlink or OneWeb terminals were used to force the satellites to transmit and, therefore, only opportunistic transmissions were received.

Figure 5.34 shows the computed spectrograms of two received Starlink signals. As can be observed, the time and frequency band support of the Starlink received signals during acquisitions longer than 1 minute is different between different receptions depending on the resource allocation and handover protocols that these satellites might be using. A higher average received power is generally observed when the satellite is near the zenith (i.e. higher elevation). Since Starlink satellites adapt their transmitted power and array aperture to approximately maintain the power flux on the Earth surface along their passes, this effect could be mainly associated to the transmission of a more continuous signal with user data when the satellite is in a near-zenith position in comparison to the transmissions received when the satellite is in a lower elevation which are mainly pulsed, as shown in Figure 5.35. It is important to note that a pulsed signal decreases the effective integration time of the passive radar signal processing and limits the unambiguous Doppler interval.

Better availability of Starlink signals could exist in other areas, depending on the network load. However, this entails a typical limitation of passive radar systems based on communication systems with respect to broadcast systems and, therefore, the exploitation of robust "always-on" signal components should be preferably considered or automatic search and selection methods should be developed, which could be time intensive in the case of a dense satellite constellation as Starlink whose resource allocation and handover protocol are not well known. For Starlink satellites, the beacon signals transmitted at the center of the frequency channels are considered a robust transmission, which could be exploited for radar application, as said before.

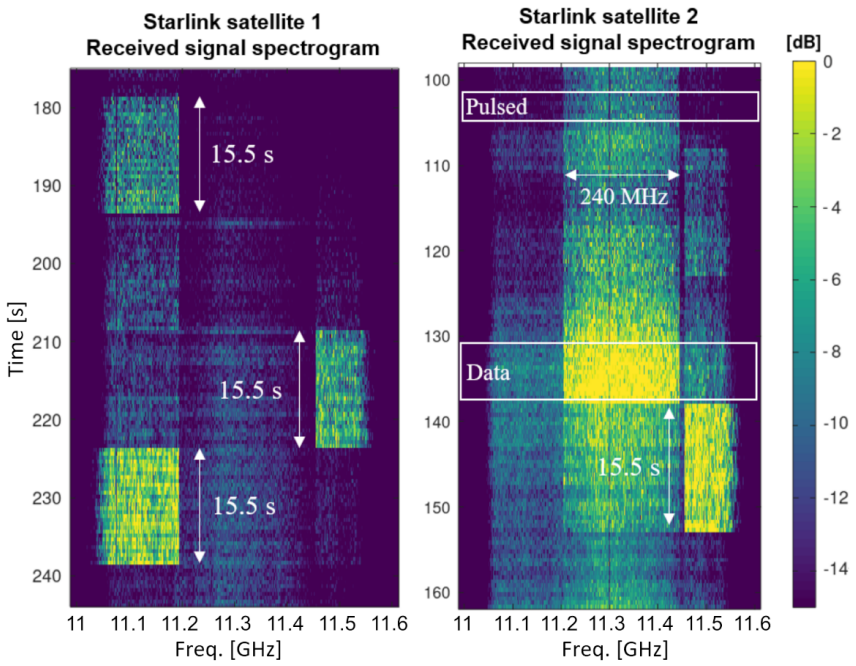

Figure 5.34: Normalized spectrograms of received signals from two Starlink satellites using a linearly polarized reception without polarization alignment.

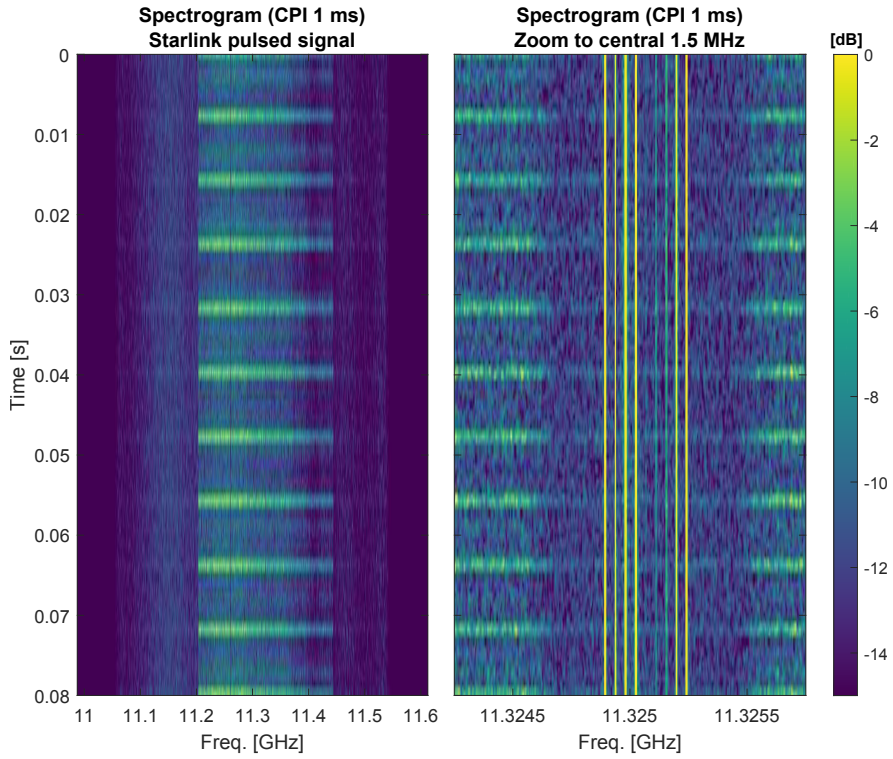

Figure 5.35: Normalized spectrogram computed with a coherent integration interval (CPI) of 1 ms of a pulsed transmission from a Starlink satellite: full-channel spectrogram (left) and zoom to the central 1.5 MHz of the transmission channel (right).

The ambiguity function obtained from an experimentally received signal with data transmission using a coherent processing interval (CPI) of 100 ms is represented in Figure 5.36. The ambiguity function shows a -3 dB-width of the main peak in the zero-Doppler cut of 1.25 m in agreement with the theoretical $\frac{c}{B}$, where c is the speed of light and B is the bandwidth of the signal (i.e. 240 MHz). In the zero-range cut, the -3 dB-width of the main peak (i.e. Doppler frequency resolution) is about 10 Hz corresponding to a 100 ms CPI. Although, the "noise-floor" is below 40 dB, the zero-Doppler cut displays a single ambiguity with level -33 dB associated with the cyclic prefix of the OFDM modulation, while the zero-range cut presents several ambiguities (i.e. at odd multiples of 188 Hz and at 686 Hz) due to the internal structure of the received signal and to some periodic OFDM symbols without transmission, which should be considered when developing the signal and data processing for the suggested passive radar architecture, for example, by attempting to remove them based on the reciprocal filter [Gas16]. As with other OFDM-based communication systems used as illuminations of opportunity (e.g. Digital Video Broadcasting – Terrestrial or Long-Term Evolution [Eve15]), the ambiguities in Doppler can be associated with the repetition of synchronisation signals or channel estimation pilots along multiple frames of the signal or, in communication system, some periodicity in the intervals without transmission.

Besides, the Starlink ambiguity function changes over time due to the different network load and worsens when less user data is being transmitted and a pulsed signal is received. For example, the zero-Doppler cut shown in Figure 5.37 for a time interval of 80 ms with a pulsed signal structure, i.e. with low data payload transmissions, presents higher ambiguity levels.

Nevertheless, when user data is being transmitted, the obtained ambiguity function is considered suitable for high-resolution passive radar applications with a thumbtack shape (i.e. a narrow peak at zero range and zero Doppler with low sidelobe levels and ambiguities).

5.6.2 OneWeb signals

Figure 5.38 shows the computed spectrogram of a received OneWeb signal during approximately 3 minutes in agreement with the satellite pass duration. The spectrogram shows an alternating pattern between two adjacent frequency channels related to the use of multiple fixed beams in

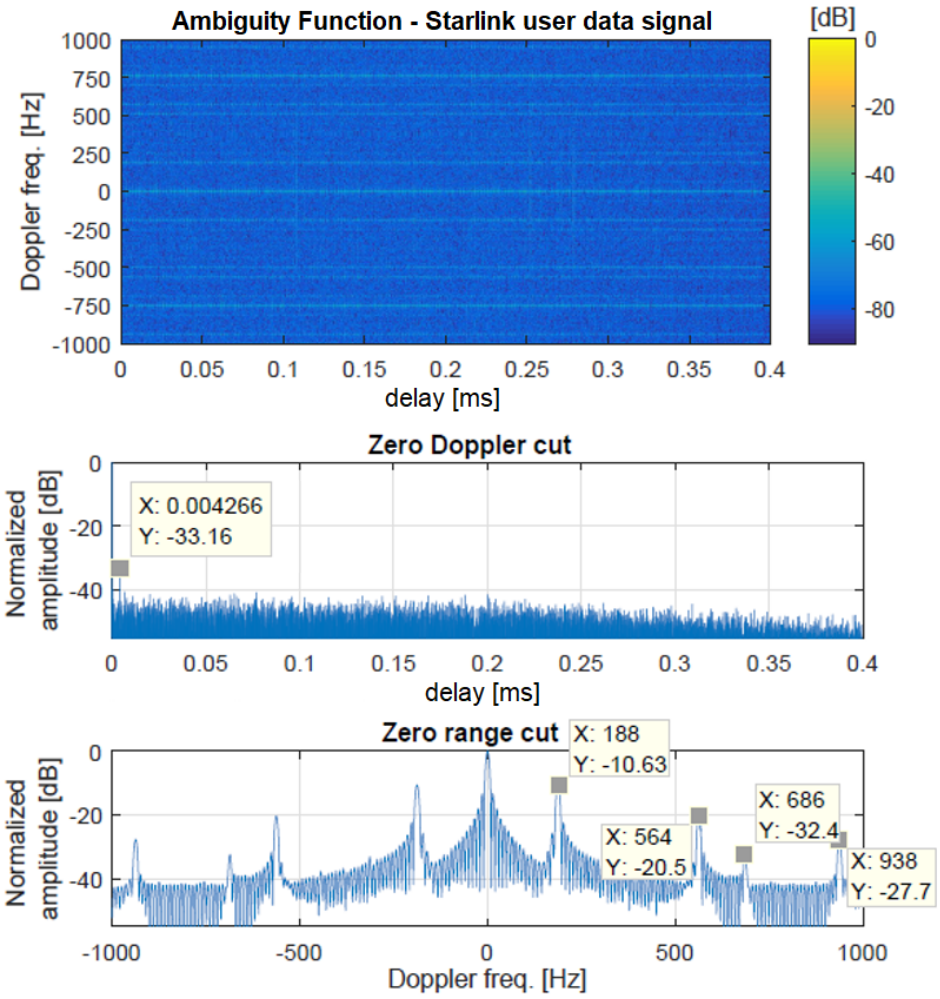

Figure 5.36: Normalized range-Doppler ambiguity function computed using 100 ms CPI from a received Starlink user-downlink signal with data transmission (filtering the 250 MHz of the transmission channel).

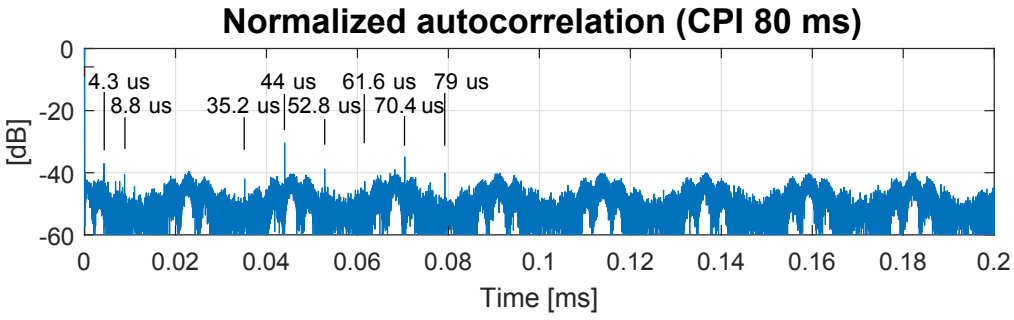

Figure 5.37: Normalized autocorrelation (i.e. zero Doppler cut of the AF) computed with a CPI of 80 ms of a pulsed transmission from a Starlink satellite.

the satellite-body reference coordinates that illuminate the area sequentially. This pattern has been observed in all performed OneWeb downlink signal measurements, showing a more robust, predictable and non-pulsed illumination of the area and an easier selection of the illuminating satellite (i.e. the satellite with higher elevation from the receiver location). However, the validity of this result should be analysed in the future when the OneWeb constellation starts to provide general communication services.

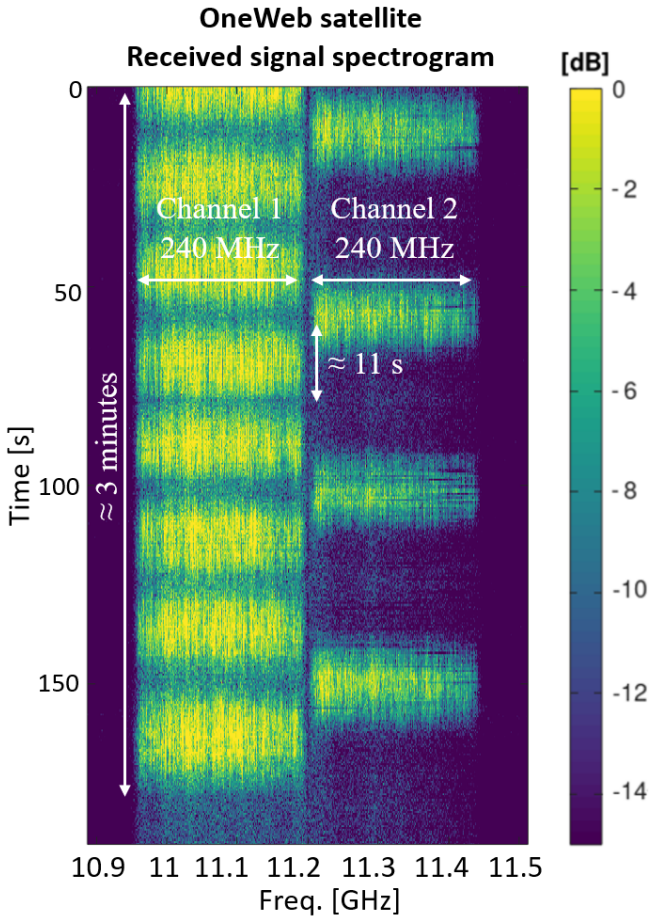

Figure 5.38: Normalized spectrogram of a received signal from a OneWeb satellite using a linearly polarized reception without polarization alignment.

The waveform diversity between both constellations is visible in the different ambiguity function that is obtained from the experimentally received OneWeb signal with a coherent processing interval (CPI) of 100 ms, represented in Figure 5.39. Similar to Starlink signals, the widths of the main peak in the zero-Doppler and zero-range cuts correspond to the 240 MHz signal bandwidth and 100 ms CPI. However, some differences are observed in the level of

ambiguities and sidelobes (i.e. "noise-floor"). OneWeb signals show a lower and more uniform "noise-floor" level with multiple ambiguities with a level lower than 40 dB in the zero-Doppler cut, while the common sinc-like pattern is obtained in the zero-range cut. However, for cuts at non-zero delays (i.e. vertical cuts of the 2D AF shown in Figure 5.39), sidelobes at multiples of 100 Hz are observed, possibly due to a signal frame structure associated to a 10 ms period. Nevertheless, the obtained ambiguity function is also considered suitable for high-resolution passive radar applications with low sidelobe levels and ambiguities.

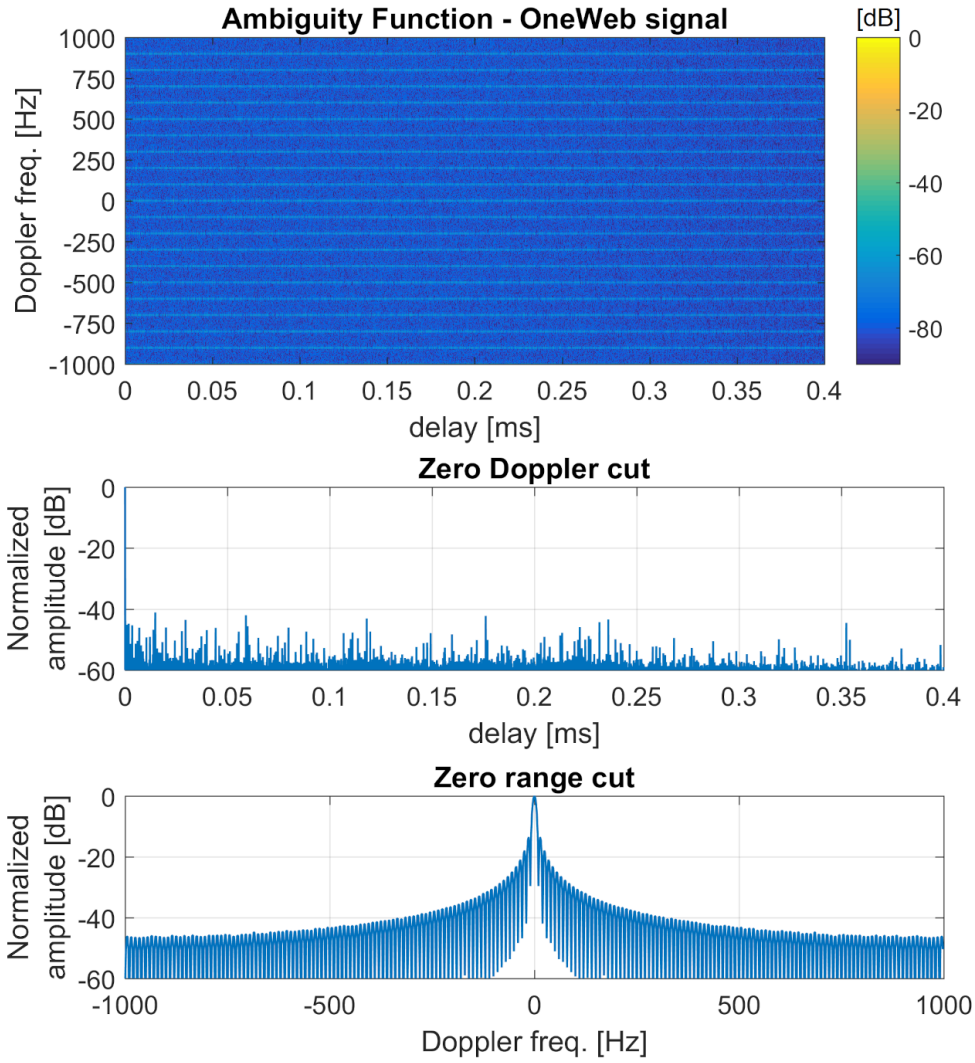

Figure 5.39: Normalized range-Doppler ambiguity function computed using 100 ms CPI from a received OneWeb user-downlink signal (filtering the 250 MHz of the transmission channel).

Having shown the technical feasibility and promising capabilities as illumination of opportunity of the user-downlink signals transmitted by the emerging LEO satellite constellations for broadband communications, as well as experimentally evaluated their ambiguity functions, which show properties suitable for high resolution passive radar applications, their preliminary experimental validation was performed. For this purpose, two measurement campaigns were carried out using the developed systems that allow the acquisition of the reference signals transmitted by the satellites and of the surveillance signals that include target and clutter scattered signals. Preliminary results of these measurement campaigns, which were focused respectively on the measurement of signals reflected by clutter or static elements of the monitored area, and on the measurement of signals reflected by a drone to evaluate the feasibility of the proposed system for moving target detection, are shown in the next chapter.

Chapter 6

Broadband Communication LEO Satellite-Based Passive Radar: Experimental Validation

In order to validate the exploitation of user-downlink signals from broadband communication LEO satellites for passive radar applications, two measurement campaigns were performed:

- The first field test was focused on the measurement of scattered signals from clutter or static elements in the area and was performed by deploying the SABBIA 2.0 passive radar system at an elevated location overlooking the Rhine river valley. These measurements are related to future remote sensing and structure monitoring applications, such as avalanche detection.
- The second field test is focused on the measurement of scattered signals from a medium sized drone, i.e. DJI Matrice 350 RTK. These measurements are related to future surveillance applications of critical infrastructures or platforms, or to 24/7 monitoring of drone flight or landing zones without the need to deploy active radars that contribute to the spectrum congestion and possible interference with critical communications systems.

The results obtained in these measurement campaigns are presented below, which allow to validate the presented concept and demonstrate the feasibility of detecting signals reflected

by clutter, up to about 2 km, and by medium sized drones up to at least 150 m, using a 30° -3 dB-beamwidth horn antenna in the surveillance channel. However, these results can be considered preliminary in the sense that better performance is expected from the application and validation in the future of more advanced radar signal processing techniques.

6.1 Area monitoring measurements

6.1.1 Measurement description

For these measurements an elevated location was selected, known as Erpeler Ley (50°34′56.9″N, 7°14″50.2″E), for the passive radar receiver with visibility over the Rhine river valley. In addition, the deployment of the system took into account the possibility of achieving appropriate geometries for certain satellite passes to apply radar imaging techniques as a way to improve the cross-range resolution by means of Doppler processing.

Figure 6.1 shows the satellite view of the measurement location representing the angular sector that is not blocked by orography and vegetation towards the area to be monitored, while Figure 6.2 show the view over the Rhine valley in the direction of the surveillance channels during the measurement.

Figure 6.1: Satellite view of Erpeler Ley showing the deployment location of the passive radar system and the sector with visibility over the Rhine valley.

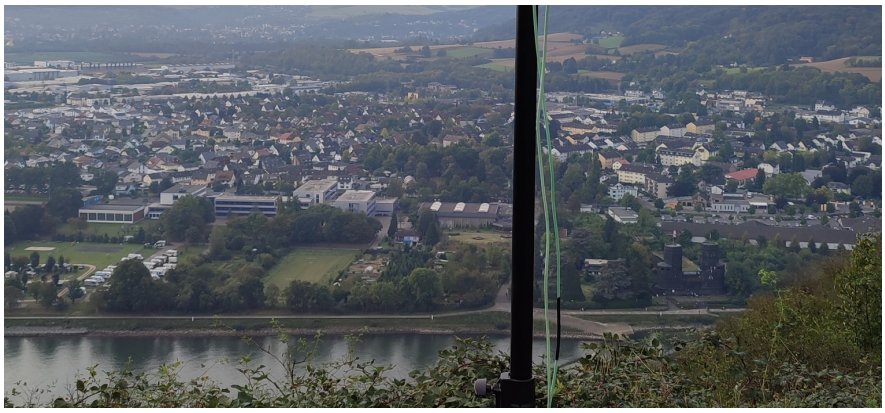

Figure 6.2: View of the Rhine valley in the direction of the surveillance channels during the measurements.

The measurement equipment consisted of the recording system SABBIA 2.0, developed by Fraunhofer FHR and adapted for the acquisition of LEO satellite signals, and two different types of antennas. One antenna setup consisted of two Kymeta antennas, which, as previously described, are electronically steerable antennas with a high gain and a narrow beamwidth, while the other one consisted of two horn antennas with fixed manual pointing, which provide a lower antenna gain but a wider beamwidth. The dimensions of these antennas are shown in Figure 6.3 and their main properties are summarized in Table 6.1.

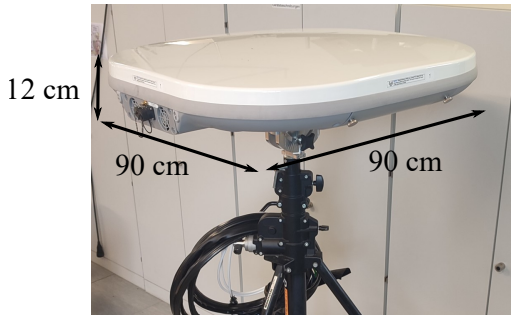

(a) u8 Kymeta antenna

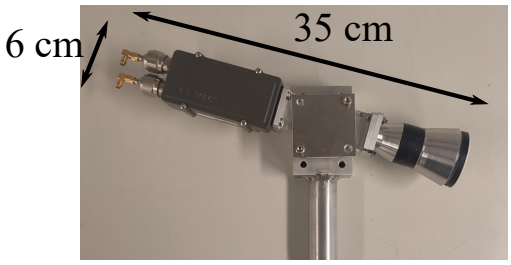

(b) Horn antenna

Figure 6.3: Antenna setups used for the measurement campaign and associated dimensions.

Property	*u8 Kymeta antenna*	*Horn antenna*
Pointing method	Electronically steerable + manual tilting	Fixed manual pointing
Antenna gain	37 dBi (estimated)	17 dBi
-3 dB-beamwidth	2.5° (estimated)	30°

Table 6.1: Main properties of the considered antenna setups.

As the SABBIA 2.0 system has four recording channels (i.e. eight real channels), the four antennas can be simultaneously connected. In this way, two reference antennas (one horn and

one Kymeta) and two surveillance antennas (one horn and one Kymeta) were used. Figures 6.4 and 6.5 show the measurement location including the antennas and the recording system SABBIA 2.0. Figure 6.6 shows the surveillance Kymeta antenna with the industrial area in the background to which the surveillance antennas were pointed.

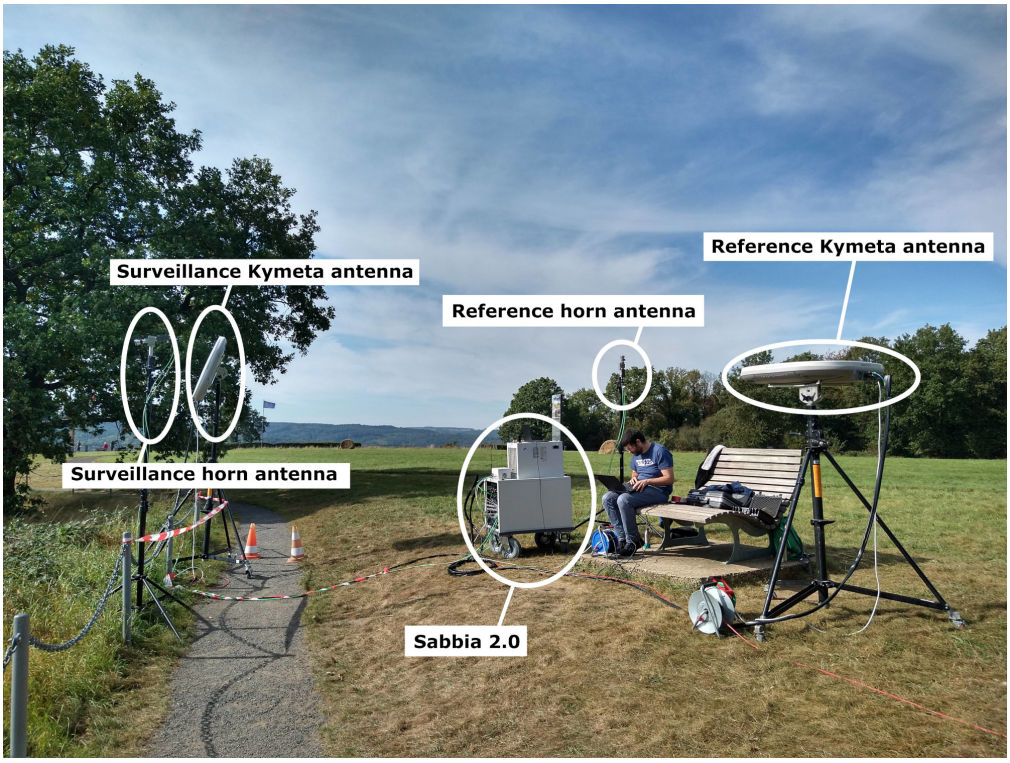

Figure 6.4: Figure of the trial location showing the antennas and the recording system SABBIA 2.0.

The reference horn antenna was pointed towards zenith, i.e. 90° of elevation. Similarly, the tripod and tilt of the reference Kymeta antenna were set up with the reference plane of the antenna parallel to the X-Y plane of the NED (North, East, Down) local reference coordinates (i.e. zero roll and pitch). Besides, the azimuth orientation of the antenna body frame (i.e. yaw) was calibrated by measuring the reference direction in which the DVB-S signals transmitted from the geostationary satellite ASTRA-1KR were received (associated to 164.7° azimuth and 31.0° elevation for the measurement location). With the antenna orientation calibrated, in order to acquire the signals transmitted by Starlink and OneWeb systems, those satellites were tracked with the electronically steerable narrow beam of the reference Kymeta antenna based on the orbit propagation from their TLE data.

Figure 6.5: Figure of the trial location showing the antennas, the recording system SABBIA 2.0, and the view across the Rhein valley.

Regarding the surveillance antennas, the Kymeta antenna was manually tilted by -70° (relative to zenith) with an additional electronically tilting of -31°, while the horn antenna was tilted by -103°, in order to locate the building at 50°34'34.15"N, 7°14'49.17"E in the main beam of the antennas. The location and tilting values of both surveillance antennas are also summarized in Table 6.2. Taking into account the configured tilt of the antennas and their associated beamwidths, Figure 6.7 represents an approximation of the estimated instantaneous footprints of the antennas over the monitored area of interest, showing the limited footprint of the Kymeta antenna due to its narrow beam. The electronic scanning of the Kymeta antenna beam could be considered in future measurements to expand the monitored area, although there would be a trade-off between the covered area and the time required.

Antenna	*Location*	*Tilting (relative to zenith)*
Kymeta	50.582473°N, 7.247245°E	−101°
Horn	50.582475°N, 7.247287°E	−103°

Table 6.2: Position and tilting (relative to zenith) of the surveillance antennas.

Figure 6.6: Figure of the trial location showing the reference Kymeta antenna and the view across the Rhein valley. The main beam of the Kymeta surveillance antenna was configured in the direction towards the buildings on the left.

The center frequency of all the measurements was set to 11.2 GHz. Therefore, the two adjacent channels from 10.95 GHz to 11.2 GHz and from 11.2 GHz to 11.45 GHz, respectively, were recorded, as previous tests showed that these channels were commonly used at the measurement location.

For these measurements, all the channels were linearly polarized. The polarization of the surveillance antenna channels were set to vertical, while no specific linear polarization alignment was set for the reference antennas since, based on public information, both OneWeb and Starlink satellites transmit circularly-polarized signals.

6.1.2 Measurement results

Using the described setup, several measurements were performed while tracking Starlink and OneWeb satellites with the reference Kymeta antenna. Since the signal transmission depends on the scheduling and handover protocols used by the satellites, which are currently not well known, as well as the network load (i.e. number of users and data being transmitted), only parts of the recordings contain signals received with enough signal-to-noise ratio in the

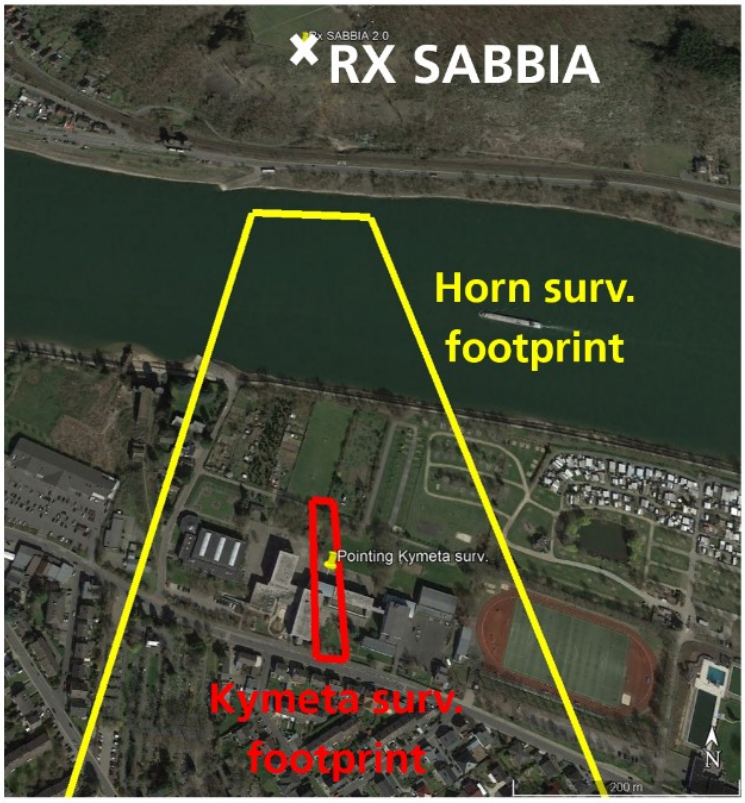

Figure 6.7: Approximate estimation of the instantaneous footprint of the surveillance Kymeta and horn antennas based on their associated -3 dB-beamwidth and configured tilt.

reference Kymeta channel to be visible in the processed spectrograms and to be, therefore, useful as reference signals for passive radar applications.

This highlights the need to improve the modelling of the resource allocation protocols or to implement an automatic searching algorithm scanning throughout the different frequency channels and visible satellites in order to reduce the time in which the system is not operational due to the lack of a received reference signal.

However, several signals from both Starlink and OneWeb satellites were recorded for different satellite positions and trajectories, as shown in Figure 6.8, giving rise to different bistatic geometries. For the measurement location, OneWeb satellites passes occur predominantly in the South-North direction, while Starlink satellites from the first and second shells (i.e. inclinations 53° and 53.2°, respectively) goes from West to East, showing complementary geometries. Preliminary analyses of exemplary Starlink and OneWeb acquisitions are reported below.

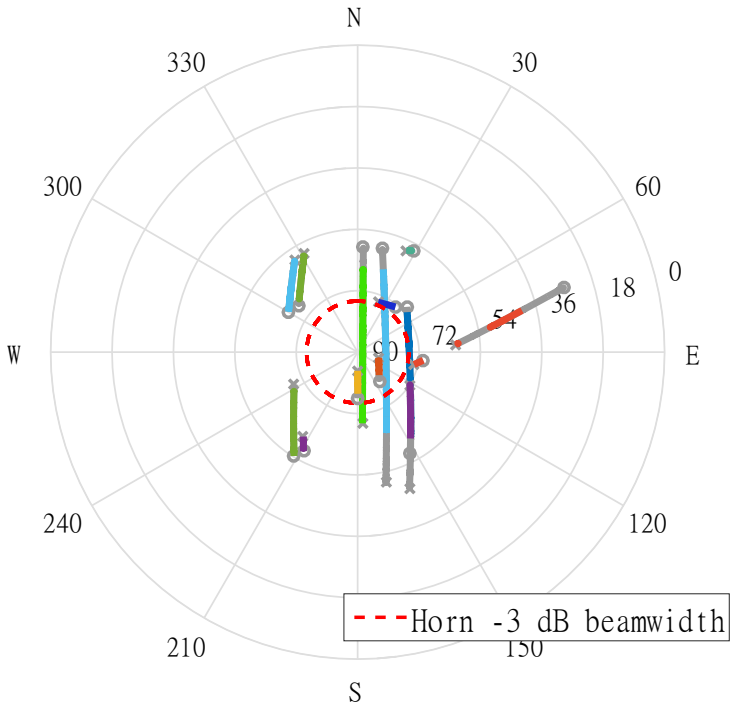

Figure 6.8: Sky plot of the tracked satellites during the measurements with signal reception. The sections of the passes with signal reception are represented with a colored solid line, while the sections without signal reception are shown as a gray solid line. The start of the satellite tracking is marked with a cross, while the end with a circle, showing the direction of the satellite pass (i.e. ascending vs. descending).

Results from a Starlink signal acquisition

Figure 6.9 shows the computed spectrograms of the received signals by the four considered channels while the STARLINK-3943 satellite was passing in ascending direction and was tracked with the Kymeta reference antenna. These spectrograms have been computed with a sampling interval of the time axis of 0.05 s. For each sampling interval, the Fast Fourier Transform (FFT) is applied over 50 consecutive signal batches of 128 µs each (i.e. coherent processing interval, CPI), which are then non-coherently averaged. Figures 6.9(a) and 6.9(b) show spectrograms computed for signals of 113 s duration received at the reference and surveillance Kymeta antennas, respectively, while Figures 6.9(c) and 6.9(d) represent the spectrograms for the reference and surveillance horn antennas.

In Figure 6.9(a) (i.e. for the reference Kymeta antenna tracking the satellites), Starlink signals can be clearly detected at positive frequencies, associated to the channel from 11.2 to

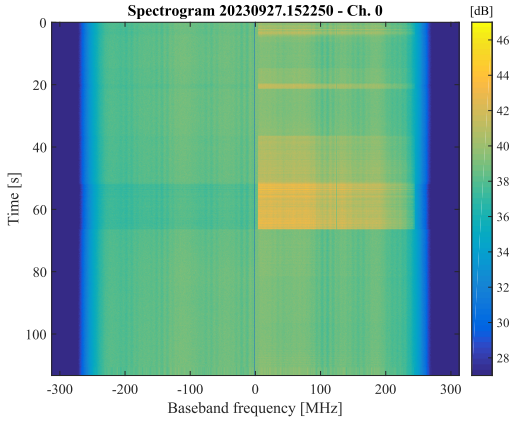

(a) Reference Kymeta antenna

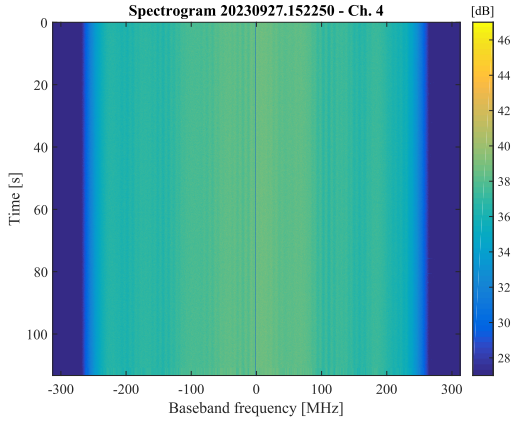

(b) Surveillance Kymeta antenna

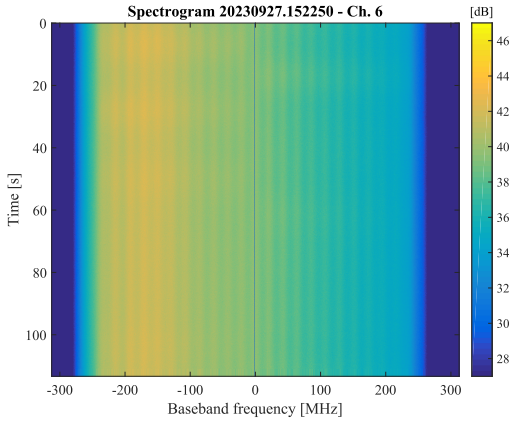

(c) Reference horn antenna

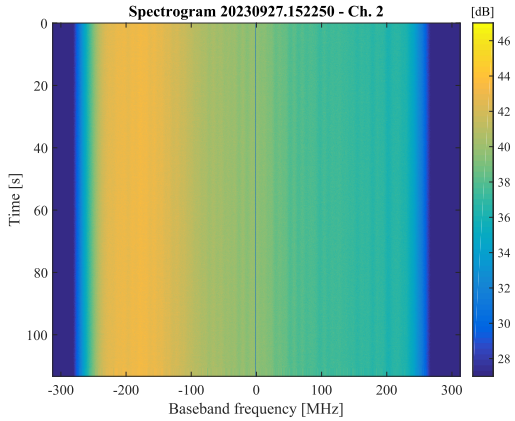

(d) Surveillance horn antenna

Figure 6.9: Spectrograms of the signals recorded for 113 s with a center frequency of 11.2 GHz using the four channels during a pass of the STARLINK-3943 satellite.

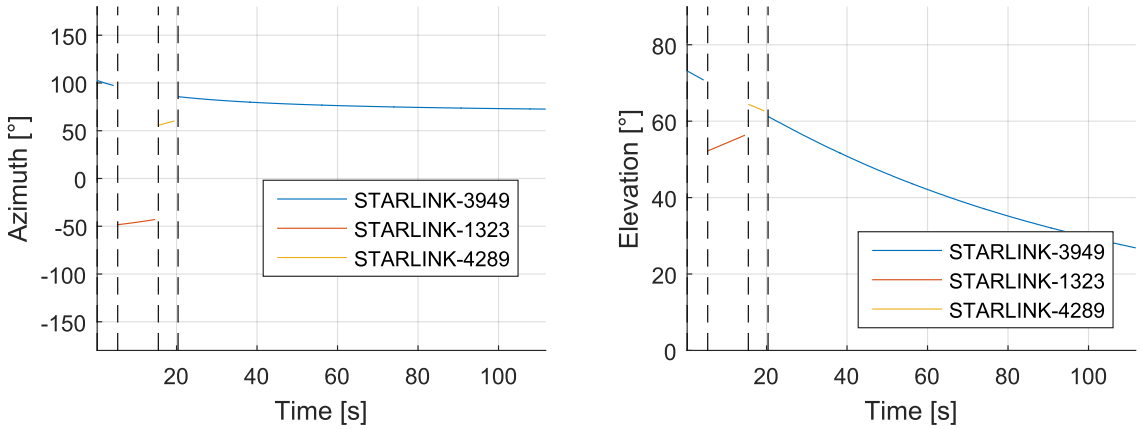

Figure 6.10: Azimuth and elevation of satellites being tracked by the reference Kymeta antenna during the considered recording.

11.45 GHz. As shown in Figure 6.10 and in the sky plot of the satellites passes during the measurement represented in Figure 6.11, at the beginning of the measurement, the reference Kymeta antenna switched between three visible Starlink satellites (STARLINK-3949, -1323 and -4289), but from 20 s onwards the antenna tracked satellite STARLINK-3949, from which signals were received. However, as the satellite was not transmitting continuously for the complete acquisition there are some gaps without visible signals in the spectrogram, e.g. from 21 s to 35 s or from 65 s.

In order to observe the variability of the received integrated power in each recorded transmitting channel (i.e. from 10.95 GHz to 11.2 GHz and from 11.2 GHz to 11.45 GHz) for the different considered antennas, the level of the spectrograms was averaged over frequency for each transmitting channel and represented along time in Figure 6.12.

As previously observed in the spectrogram of the reference Kymeta antenna, Starlink signals are detected for certain time intervals in the upper frequency channel. While tracking the satellite STARLINK-3949 (from time 20 s), significant jumps in the averaged level are observed with a periodicity of 15 s, suggesting that the handover or resource allocation protocols might operate in intervals of this duration. Although these level jumps could also be related to changes on the network load, they are more likely due to changes of the satellite beam that is serving the area where the receiver is located. When the averaged level is at its maximum (i.e. between 51 s and 66 s), a spot beam at the upper frequency channel may be steered to the receiver area, while when receiving a lower level (i.e. from 36 s to 51 s),

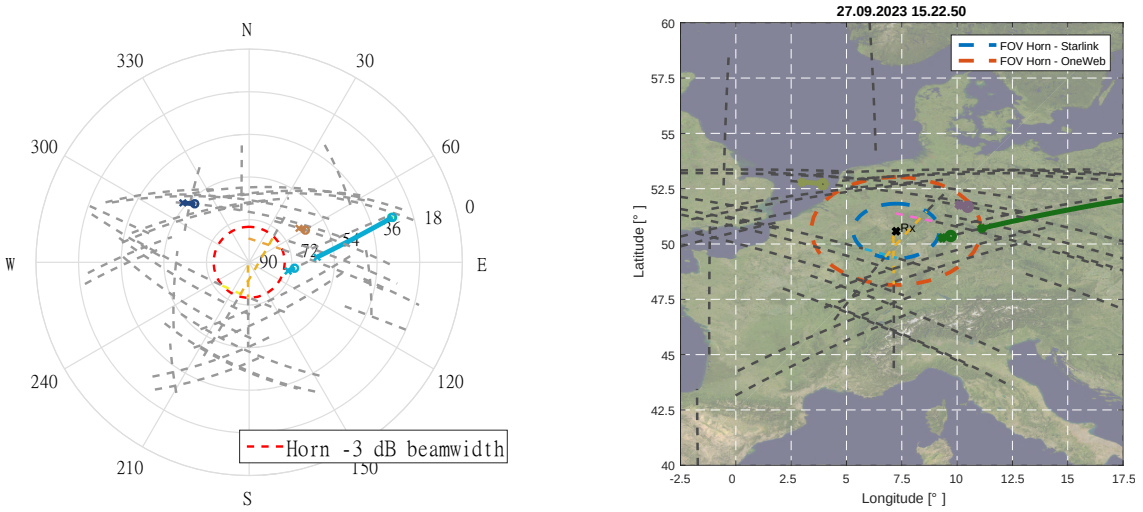

Figure 6.11: Sky plot of the satellite passes (left) and projection over an Earth map (right) of the satellites crossing the cone defined by an elevation higher than 40° during the considered measurement. Sections of the passes crossing the reference horn antenna -3 dB-beamwidth are represented with a colored dashed line, while the rest of the pass is represented with a gray dashed line. Tracked sections by the reference Kymeta antenna are represented by a solid colored line, whose start is marked with a cross and the end with a circle. Note that the horn antenna -3 dB-beamwidth (i.e. field-of-view, FOV) covers a wider area for OneWeb constellation due to the higher altitude of its orbits.

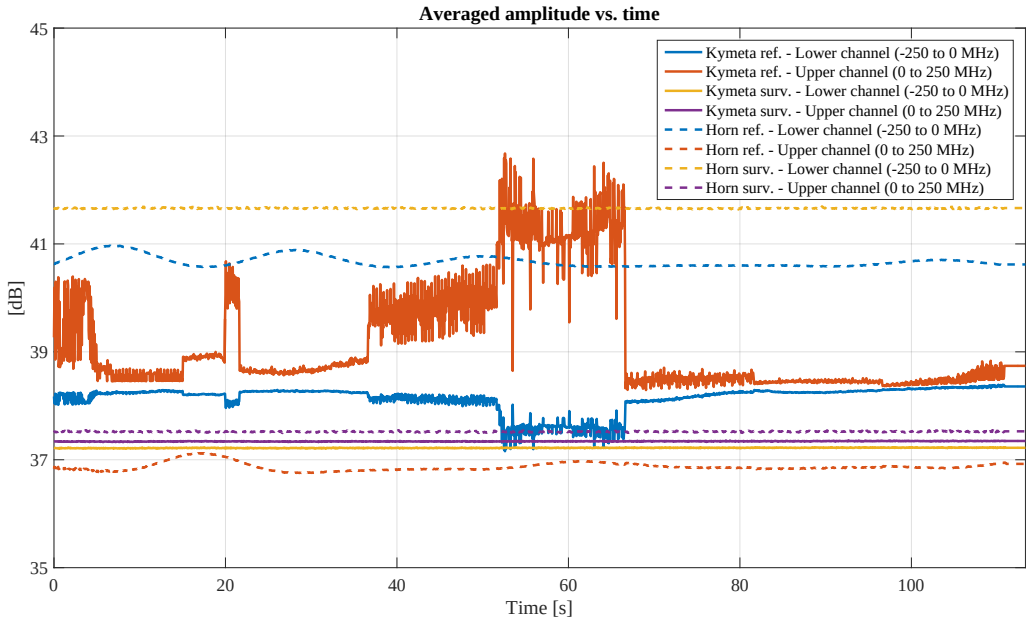

Figure 6.12: Averaged amplitude level along time in both digitised frequency channels (i.e. lower channel from 10.95 GHz to 11.2 GHz and upper channel from 11.2 GHz to 11.45 GHz) for the four considered antennas.

the signals might be received from a spot beam steered towards an adjacent cell. At those intervals in which the received averaged level is low or no signal is received, the receiver area might be served at a frequency channel which was not digitised (e.g. above 11.4 GHz) or by another Starlink satellite among those visible (refer to sky plot in Figure 6.11). Besides, the level variability inside each 15 s interval also shows some degree of periodicity which might be related to the use of periodic synchronization and pilot sequences.

The level jumps and variability in the lower frequency channel for the reference Kymeta antenna are not related to the reception of signals in this band but to an effect of the automatic gain control (AGC) implemented in the receiving system in order to avoid saturation while optimizing the usage of the dynamic range. When signals are received in the upper frequency channel, the total received power increases and, therefore, the AGC increases the attenuation to maintain the targeted averaged output level.

The averaged level of both the lower and upper frequency channels for the Kymeta and horn antenna surveillance channels does not change along the measurement, and no direct or scattered signals from the satellite can be detected in them without applying further processing. In agreement with the link budgets previously performed, this results experimentally shows that it is not feasible to receive with enough SNR the direct signal transmitted by these LEO satellites with a wide beam antenna and, therefore, a high-gain narrow beam antenna tracking the satelite is required to receive the full-band refrence signals. Since both surveillance antenna main beams are pointed towards the area of interest on the ground, direct signals might be only received through the sidelobes of the antennas with an increased attenuation, while scattered signals from the area of interest are also attenuated due to the two-way path propagation and to the fact that only part of the signal energy is reflected towards the surveillance antennas. These reasons explain why these signals are below the noise level in the surveillance channels if no further coherent integration is performed.

The slight ripples that are observed in the reference horn antenna channel for both the lower and upper frequency bands are thought to be due to the reception with low SNR of signals transmitted by two subsequent OneWeb satellites that were passing towards North

during the measurement. This pattern is similarly observed in the measurements presented below in which OneWeb satellites were tracked with the reference Kymeta antenna.

Furthermore, for both horn antenna channels, an unequal power distribution can be observed in the spectrograms between negative and positive frequencies. This effect is thought to be due to the frequency-dependent response of the currently used horn antennas and the circular to rectangular waveguide transitions between the antenna output and the Low-Noise Block (LNB) input.

Additionally to the full-band spectrograms, a closer analysis has been performed of the 1 MHz band at the center of the upper frequency channel (i.e. the band from 11.3245 GHz to 11.3255 GHz), in which beacon signals from Starlink satellites are expected to be received. Figure 6.13 represents the computed spectrograms for the central 1 MHz-band of the considered upper frequency channels for both the reference Kymeta and horn antennas. These spectrograms have been computed considering a sampling interval of the time axis of 0.4 s, applying for each interval an FFT over 4 consecutive batches of 8.192 ms (i.e. CPI), which are then non-coherently averaged. Besides, the computed spectrum for three specific times at which the STARLINK-3949 satellite was being tracked by the reference Kymeta antenna is represented in Figure 6.14, in which the beacon signals are shown.

As can be observed, the beacon signals transmitted from the tracked satellites are visible in the recorded signals from the reference Kymeta antenna even at times where data signals were not received, while no beacon signals are detected in the measurement from the reference horn antenna. During the measurement, the satellites tracked with the reference Kymeta antenna, whose beacon signals are detected, did not cross the main -3 dB-beamwidth of the reference horn antenna and, therefore, these beacons may not be received with enough SNR to be visible in the computed spectrogram. However, other three Starlink satellites crossed the main beam of the reference horn antenna during the recording, but their beacons signals are not detected either. Since beacons signals were detected in previous measurements using a horn antenna, further analysis and tests are required to assess the robustness of receiving these beacons with a low-gain wide beam antenna (in comparison to the Kymeta antenna). This would potentially enable the simultaneous reception of the beacon signals transmitted

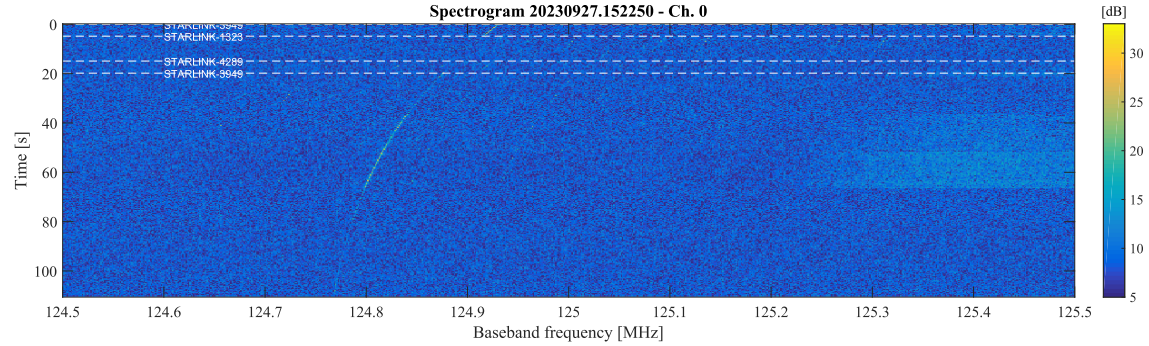

(a) Reference Kymeta antenna

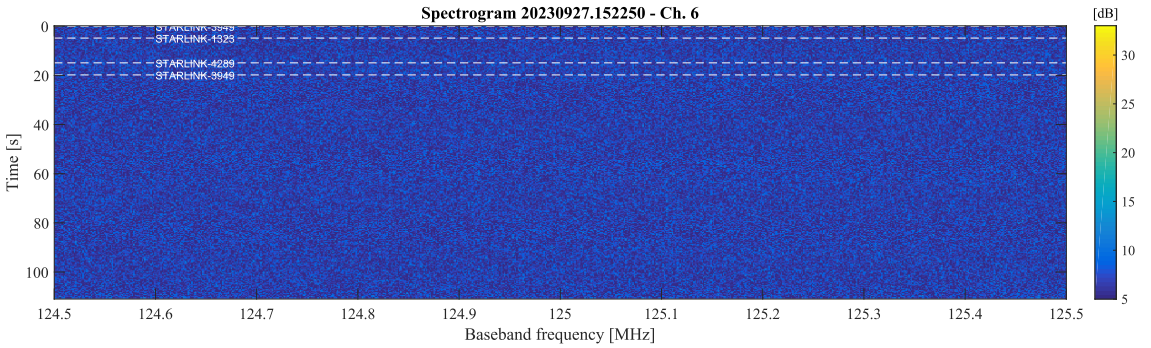

(b) Reference horn antenna

Figure 6.13: Spectrogram of the central 1 MHz-band of the upper frequency channel for the received signals with a) reference Kymeta antenna and b) reference horn antenna.

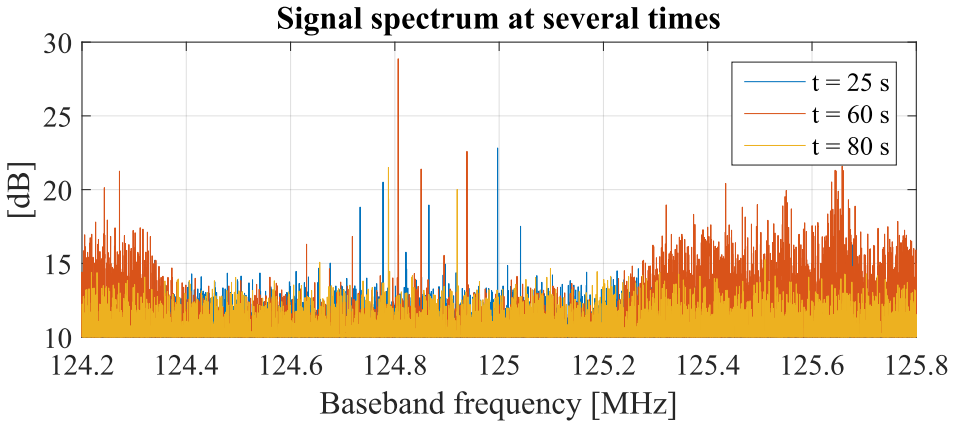

Figure 6.14: Spectrum at the center of the upper frequency channel of the received signal by the reference Kymeta antenna at several recording times.

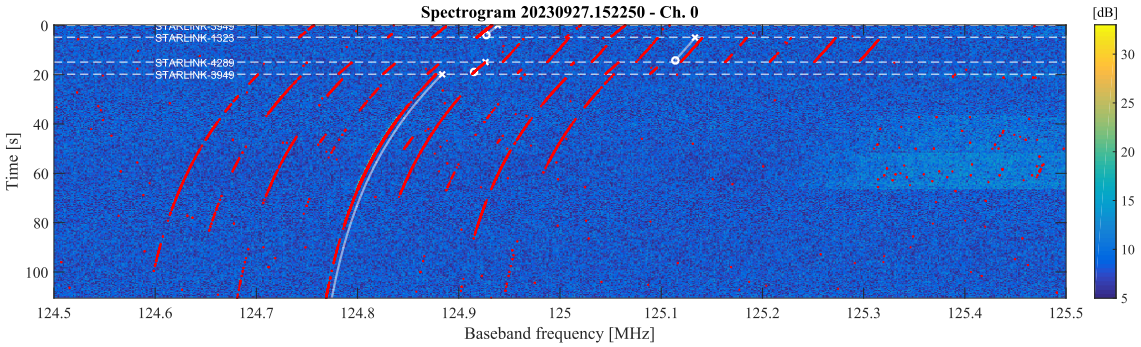

Figure 6.15: Automatic pilot detections using a CA-CFAR algorithm (red dots) and estimated Doppler frequency for the tracked satellites (white solid lines) over the spectrogram computed for the received signals with the reference Kymeta antenna.

by multiple visible Starlink satellites, which might be of interest for some multistatic imaging methods [Cri23b].

To verify the reception of the beacon signals and compare their received frequency variation with the predicted Doppler frequency for each tracked satellite from its TLE data and the SGP4 orbit propagator, Figure 6.15 represents these Doppler predictions (white lines) and the automatic pilot detections (red dots) obtained by the CA-CFAR (cell-averaging constant-false alarm rate) algorithm over the spectrogram computed for the reference Kymeta antenna. As can be seen, up to 9 pilot signals are received from each satellite with a 44 kHz separation between them, being the central pilot normally the one with the highest level. The frequency variations of the pilot signals match the pattern of the estimated Doppler frequency, however there is a shift between the received center pilot frequency and the Doppler frequency estimates that is different (positive or negative) for the different satellites tracked. It is thought that these shifts are mainly due to inaccuracies in the satellite position estimation from the TLE data and the orbit propagator or to synchronization differences between the satellite transmitters and the receiver oscillators. These inaccuracies limit the application of imaging methods, such back-projection, that compensate for the transmitter movement in order to focus the response of the scatters. Therefore, further analysis is required to develop methods that improve the accuracy of the satellite position estimation, for example based on the received direct signal, in order to enable the application of imaging algorithms and effectively increase the integration time by compensating for the movement of the transmitter.

Nevertheless, range-Doppler maps can be computed by cross-correlating, for example, the reference signal received by the Kymeta reference antenna and the surveillance signal received by the surveillance horn antenna, which has a wider beam than the Kymeta antenna, potentially receiving scattered signals from a wider area. As an example, Figures 6.16 and 6.17 show the range-Doppler map obtained for the received signals at the measurement time of 58 s with a CPI of 3 s in which, apart from the direct signal interference at zero range and zero Doppler and ambiguities associated to it at zero range and ± 0.15 kHz, some weak scattered signals can be observed at close range and up to 750 m in bistatic range. These signals might be associated to static elements or clutter of the area but the SNR is low to obtain more details of it. The received signal power for Starlink satellites, which is lower than expected, may be explained by the fact that the full user data payload was not being used. Using a longer CPI to increase the SNR of the scattered signals would require the application of TMC or back-projection methods that require more accurate estimations of the satellite positions during the CPI.

However, this result already validates the operation of the developed system and the feasibility of receiving and detecting scattered signals from an area by exploiting user-downlink signals from the emerging broadband communication LEO satellites using a passive radar configuration.

Results from a OneWeb signal acquisition

Similarly, Figure 6.18 shows the computed spectrograms of the signals received with the four channels while the ONEWEB-0446 satellite was passing in ascending direction (from South to North) and was tracked with the reference Kymeta antenna. These spectrograms have been computed with the same parameters used previously for Starlink results. Besides, Figure 6.19 represents the azimuth and elevation of the ONEWEB-0446 satellite being tracked by the reference Kymeta antenna, and Figure 6.20 shows the sky plot of the satellite passes during the measurement.

In the recorded signal from the reference Kymeta antenna, which was tracking the considered OneWeb satellite, signals can be clearly detected with an alternating pattern between both lower and upper frequency channels. As said before, this pattern can be explained by the way

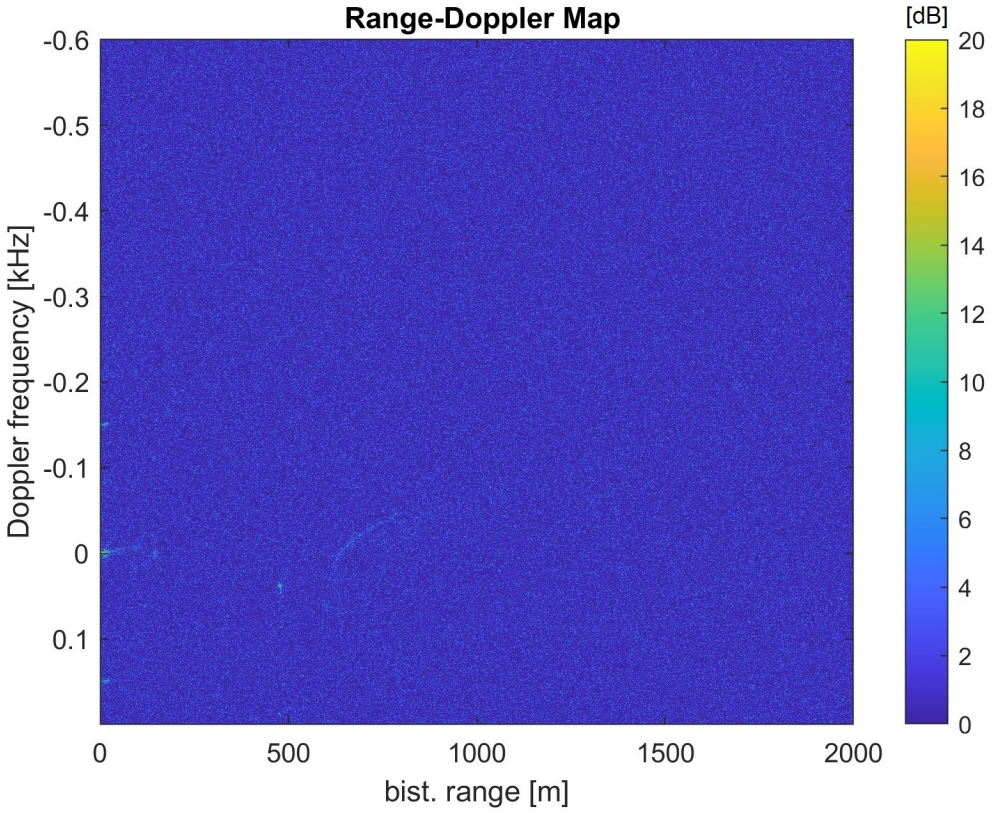

Figure 6.16: Range-Doppler map obtained by cross-correlating the reference signal received by the Kymeta antenna tracking the considered Starlink satellite and the surveillance signal received by a horn antenna pointed towards the area of interest, using a CPI of 3 s.

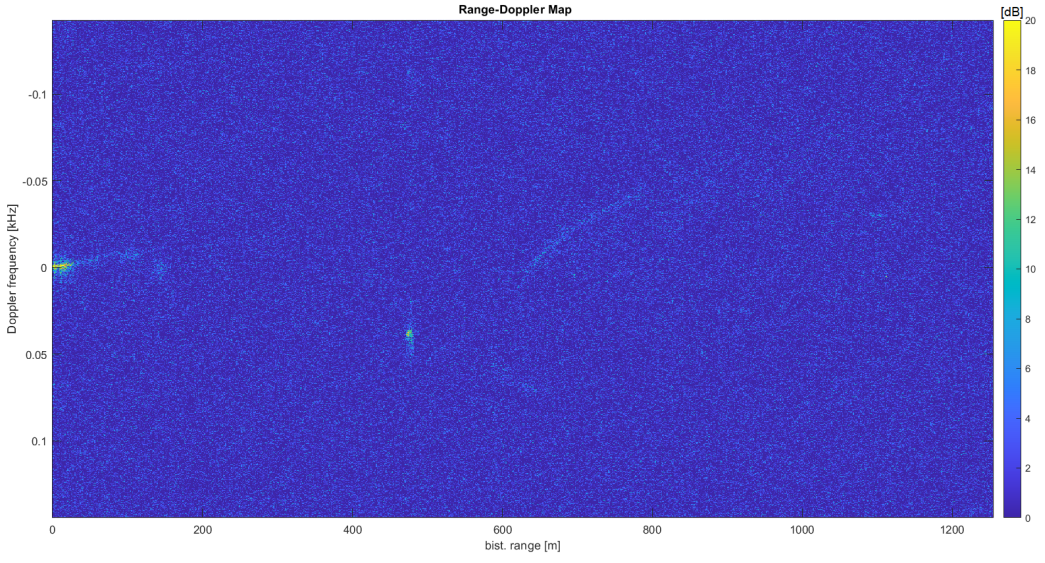

Figure 6.17: Zoom of the range-Doppler map of Figure 6.16 in which clutter scattered signals are observed with low SNR.

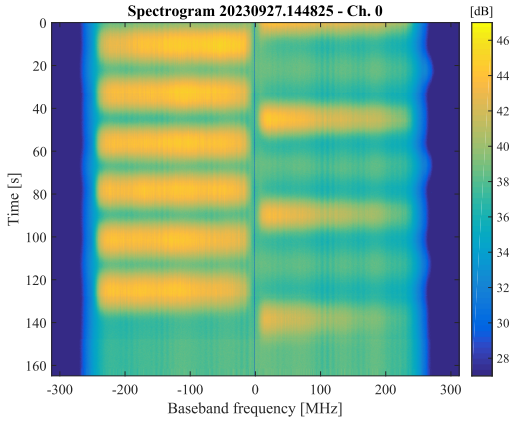

(a) Reference Kymeta antenna

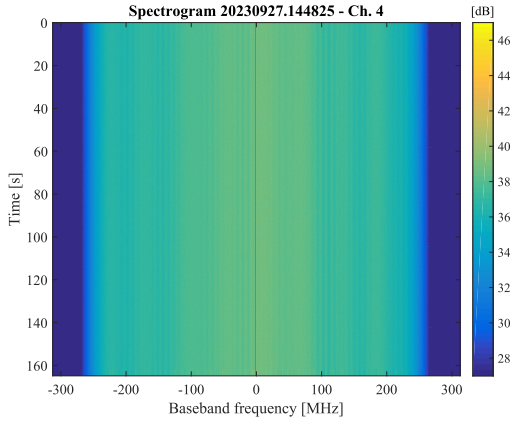

(b) Surveillance Kymeta antenna

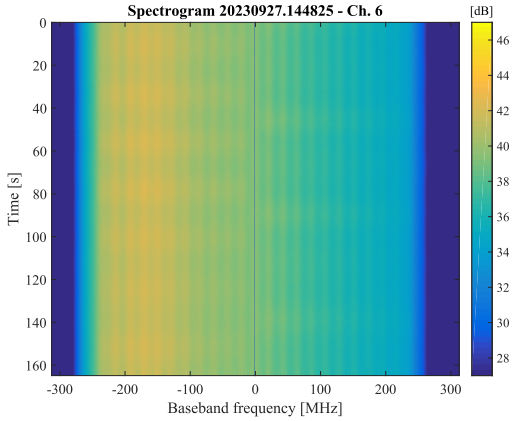

(c) Reference horn antenna

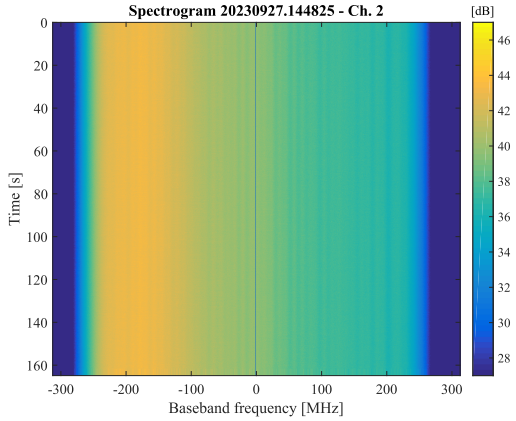

(d) Surveillance horn antenna

Figure 6.18: Spectrograms of the signals recorded during 162 s for a center frequency of 11.2 GHz with the four channels during a pass of the ONEWEB-0446 satellite.

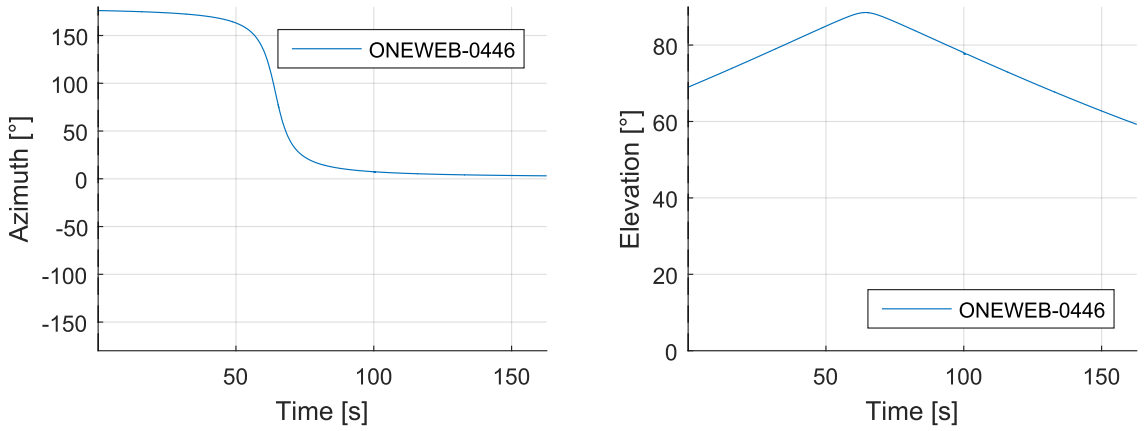

Figure 6.19: Azimuth and elevation of the ONEWEB-0446 satellite being tracked by the reference Kymeta antenna during the considered recording.

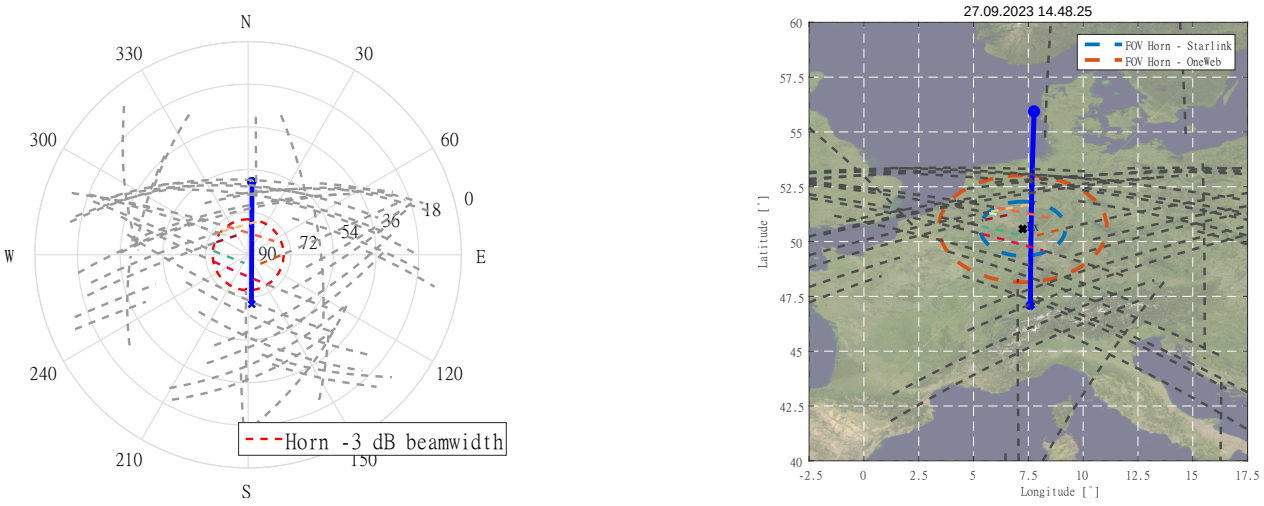

Figure 6.20: Sky plot of the satellite passes (left) and projection over an Earth map (right) of the satellites crossing the cone defined by an elevation higher than 40° during the considered measurement. Sections of the passes crossing the reference horn antenna -3 dB-beamwidth are represented with a colored dashed line, while the rest of the pass is represented with a gray dashed line. Tracked sections by the reference Kymeta antenna are represented by a solid colored line, whose start is marked with a cross and the end with a circle.

OneWeb satellites illuminate a point on the ground with consecutive beams which are fixed in the satellite body reference, while adjacent beams transmit in different frequency channels to avoid interference. Although, no signals are visible in the spectrograms of both surveillance antennas, a slight ripple is observed in the spectrogram of the reference horn antenna, which is clearer in the averaged level for each considered frequency channel represented in Figure 6.21, due to the low SNR reception of OneWeb signals from the satellite crossing the main beam. Each of the beams illuminate a certain point on ground for about 10 seconds which is in agreement with the specified beamwidth in the along track direction of the transmitting OneWeb beams.

The received signals from OneWeb satellites covered the full 240 MHz channel, while no narrow-band beacon signals are observed. It is known that OneWeb signals are single carrier-time division multiplexed (SC-TDM) signals and, therefore, synchronization and pilot sequences would typically cover the full band. Since no averaged level changes are observed that could be associated to changes on network load, which are expected in a common operation of a communication system, the received signals might be some kind of test signals or “always-on” components (i.e. synchronization and pilot signals).

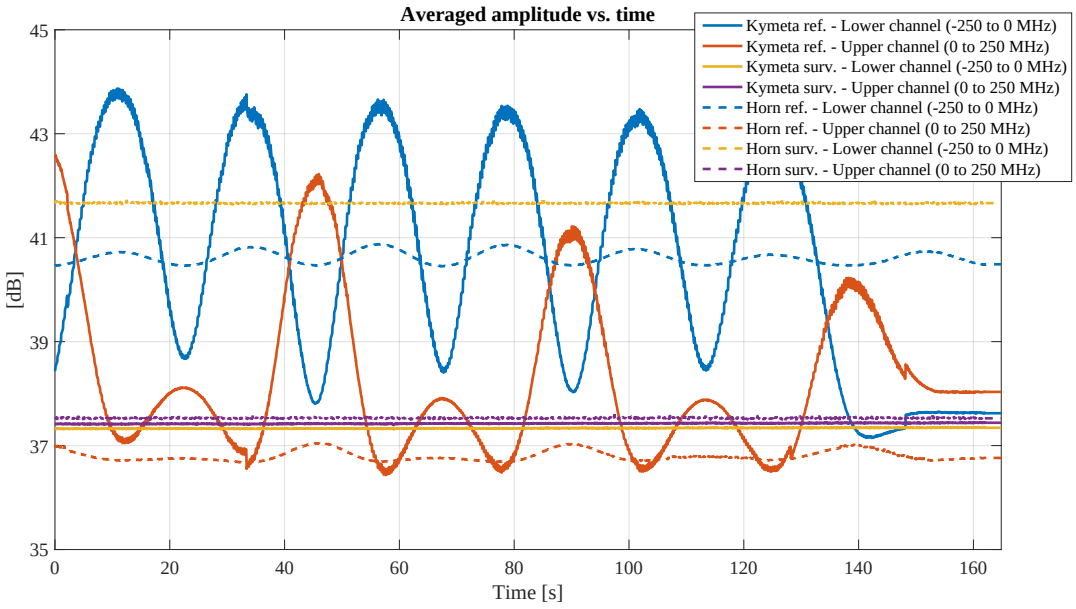

Figure 6.21: Averaged amplitude level along time in both digitised frequency channels (i.e. lower channel from 10.95 GHz to 11.2 GHz and upper channel from 11.2 GHz to 11.45 GHz) for the four considered antennas.

An exemplary result of the range-Doppler map computed based on the cross-correlation between the reference signal received with the Kymeta antenna and the surveillance signal received by the horn antenna at the measurement time of 55 s for 0.54 s of CPI, without applying any motion compensation or back-projection, is shown in Figure 6.22. This result validates the possibility to measure scattered signals exploiting OneWeb transmissions and, compare to the Starlink results, presents better SNR due to the characteristics of the received OneWeb transmissions, which are received with a uniform level for each beam along the pass.

Figure 6.23 shows the analysis of the bistatic geometry at the considered time in terms of the bistatic range, bistatic Doppler frequency and bistatic Doppler frequency rate for the monitored area considering its orography and static clutter. As can also be seen in Figure 6.24, the specific geometry during the CPI, with the surveillance horn antenna looking South and the OneWeb satellite also approaching from South, leads to iso-range curves whose tangents at the points associated to the pointing direction of the antenna are mostly parallel to the iso-Doppler curves, giving rise to the quasi linear dependency between bistatic range and bistatic Doppler which is observed in the clutter scattered signals of the range-Doppler map, and not much angle-dependant clutter spread. In addition, spatial ambiguities occur as several points present the same bistatic range and Doppler frequency.

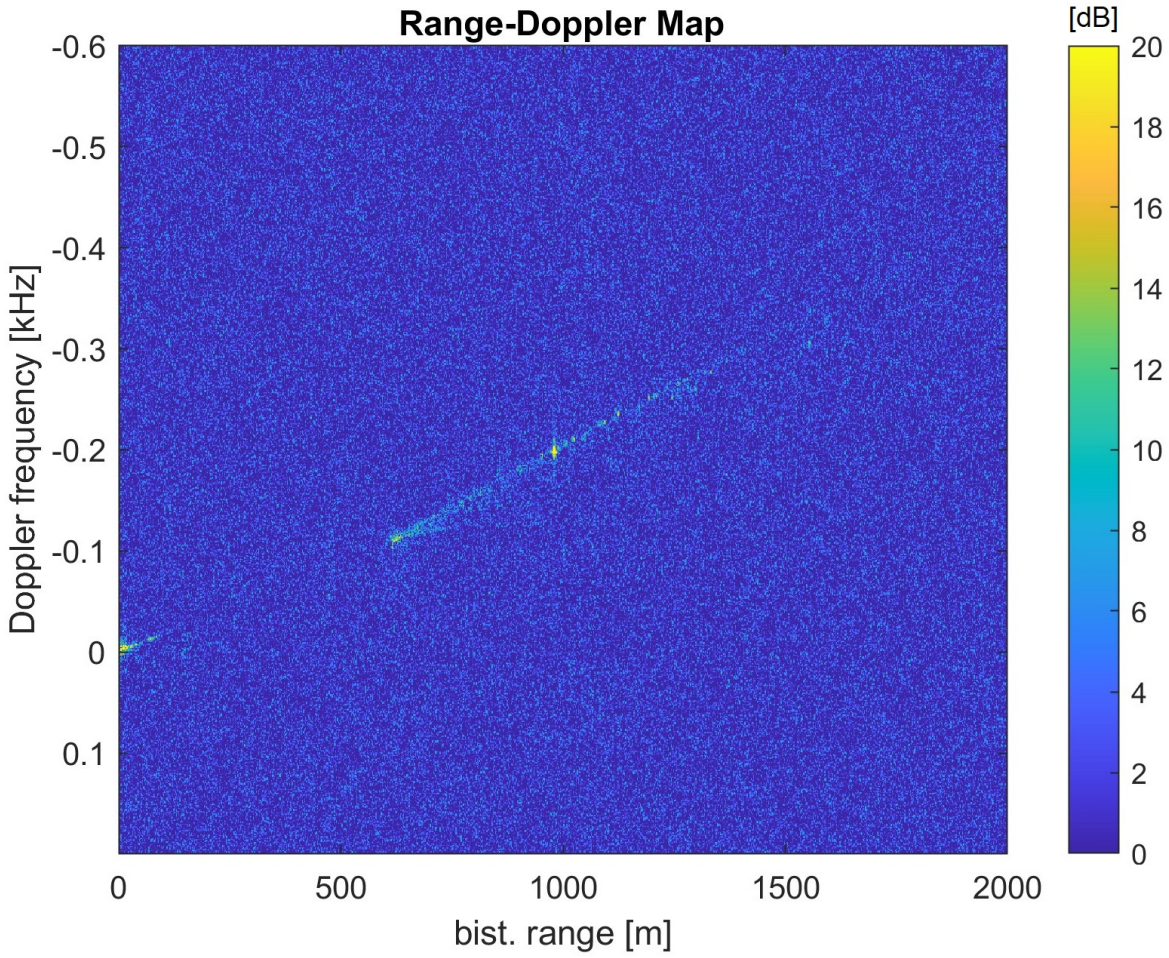

Figure 6.22: Range-Doppler map computed with a 0.54 s CPI by cross-correlating the reference signal received with the Kymeta antenna and the surveillance signal received with the horn antenna looking South for a OneWeb acquisition with the satellite approaching from South.

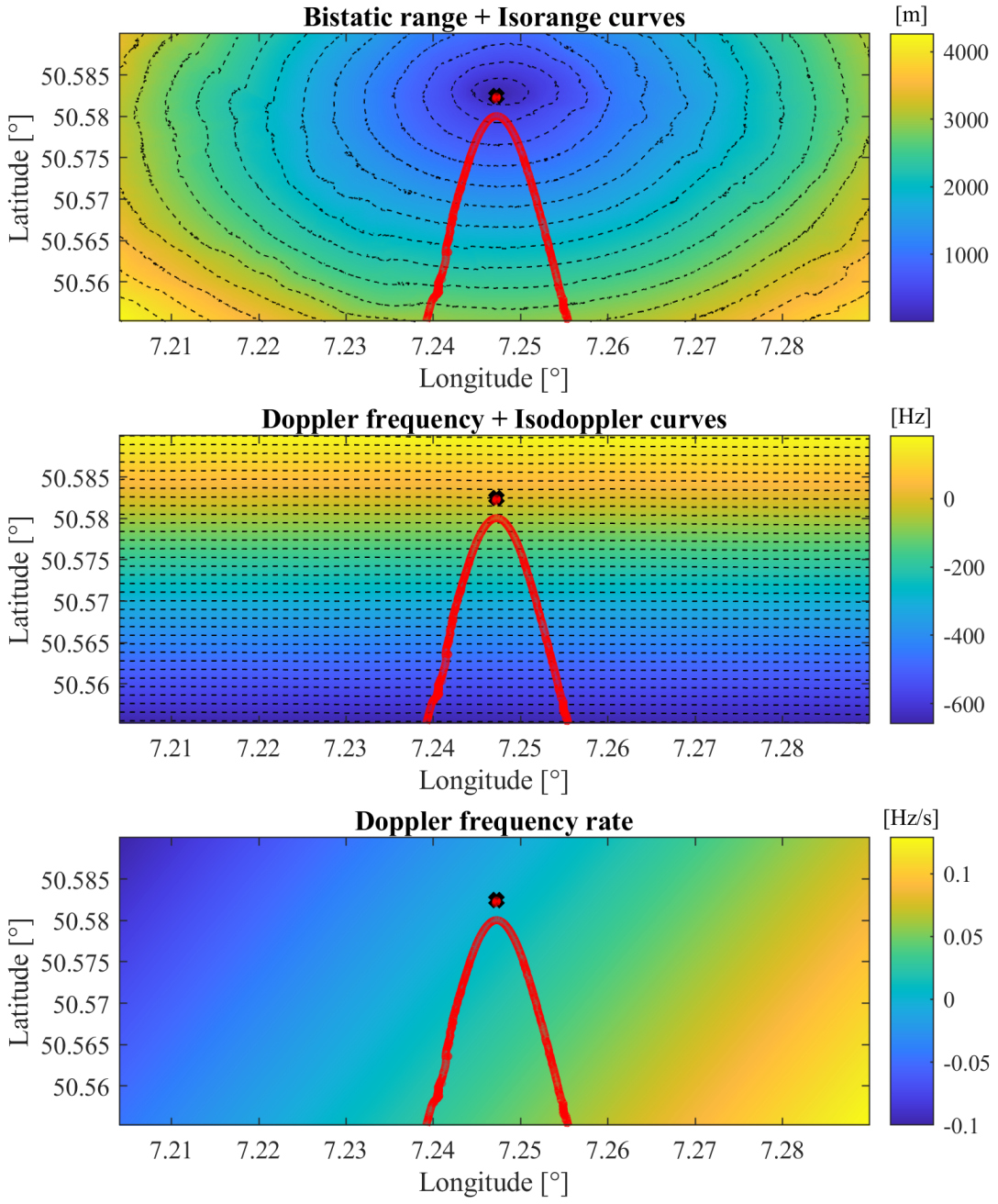

Figure 6.23: Bistatic range, bistatic Doppler frequency and bistatic Doppler frequency rate for the monitored area at the considered measurement time. Iso-range and iso-Doppler curves are marked by dashed black lines. The -3 dB-footprint of the surveillance horn-antenna pattern is marked with a solid red line.

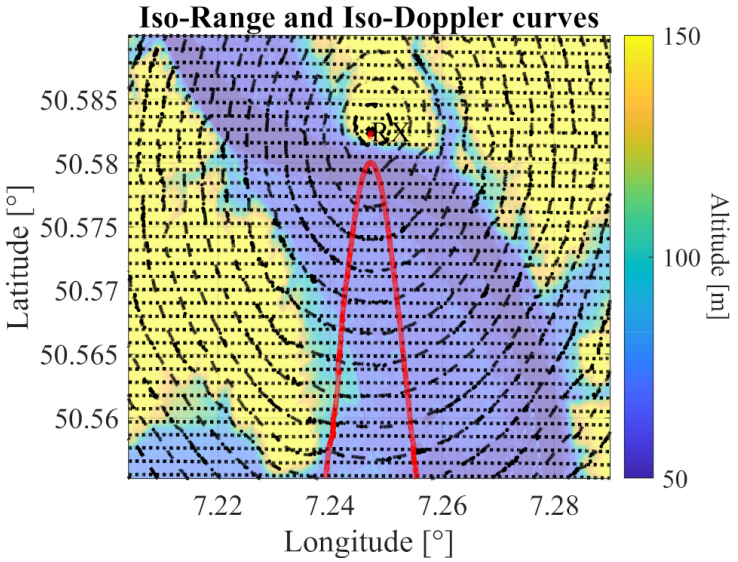

Figure 6.24: Iso-range and iso-Doppler curves (dashed black lines) over an altitude map of the monitored area. The -3 dB-footprint of the surveillance horn-antenna pattern is marked with a solid red line.

In order to better match the measured range-Doppler clutter response with a simulated one considering the specific position and dynamics of the reference satellite at the measured time, it has been observed that a time-shift can be applied to the predicted trajectory of the satellite from the TLE data. This is due to the already discussed inaccuracies of the satellite orbit propagation from TLE data using the SGP4 model. A similar time-adjustment method to reduce the SGP4 propagation error in the context of opportunistic navigation exploiting LEO satellites has been presented in [Hay23]. As an example, for the considered measurement time, after applying a 4 s-time shift to the propagated satellite trajectory, the projection of a grid of points in line of sight (LOS) and inside the antenna footprint (Figure 6.25) over the range-Doppler map matches the measured clutter response, as shown in Figure 6.26. Besides, Figure 6.27 represents the projection over the range-Doppler domain of the grid of points in LOS for a $\pm 45°$ sector and for the antenna footprint, showing how the antenna beam limits the clutter Doppler spread as the instantaneous field-of-view is narrower.

Given the analysed bistatic geometry, when projecting the range-Doppler map onto a geographic coordinate system, no cross-range resolution improvement is observed, as shown in Figure 6.28 and, also, in Figure 6.29 over a satellite image of the area. This result motivates the future application of fusion or multistatic approaches to exploit the spatial diversity offer

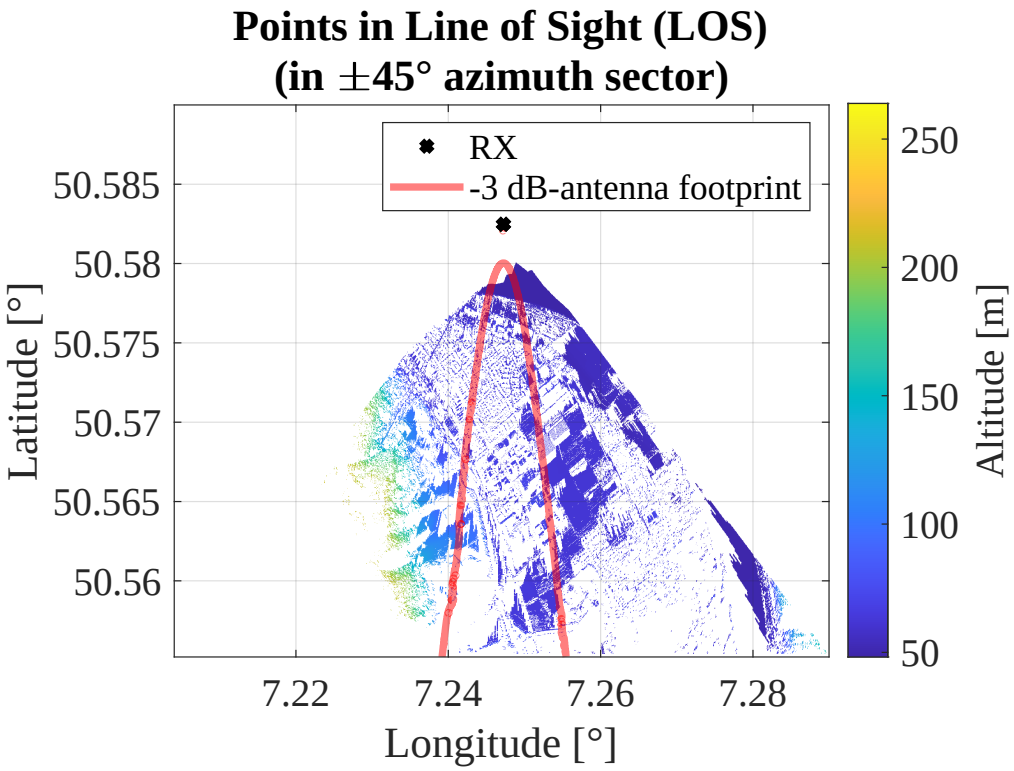

Figure 6.25: Surface points in line of sight from a grid spanning a ±45° azimuth sector around the surveillance antenna pointing direction. The color of each point represents its associated altitude. The -3 dB-footprint of the surveillance horn-antenna pattern is marked with a solid red line.

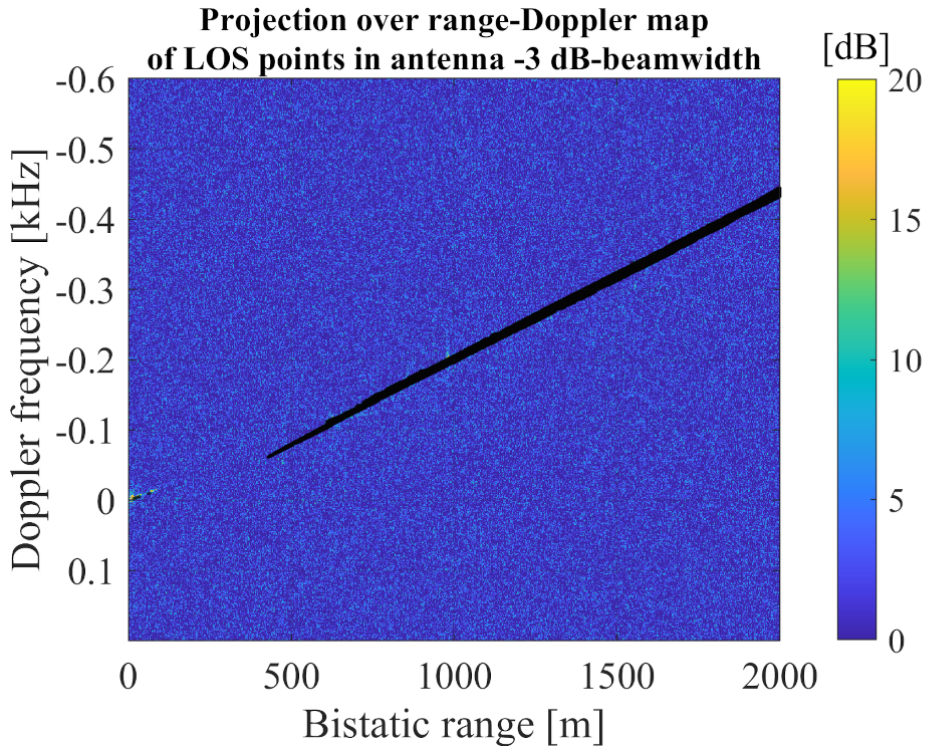

Figure 6.26: Projection (in black) of LOS points inside the surveillance -3 dB-antenna beamwidth over the computed range-Doppler map.

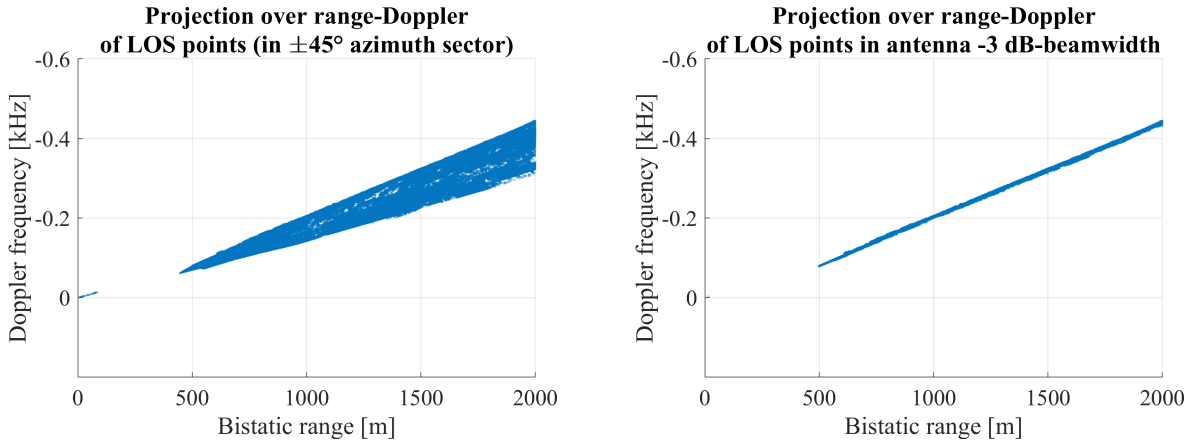

(a) Projection of points in line of sight from a grid spanning a ±45° azimuth sector around the antenna pointing direction.

(b) Projection of points in line of sight and inside the surveillance -3 dB-antenna beamwidth from a grid spanning a ±45° azimuth sector around the antenna pointing direction.

Figure 6.27: Projection of surface points onto the range-Doppler domain.

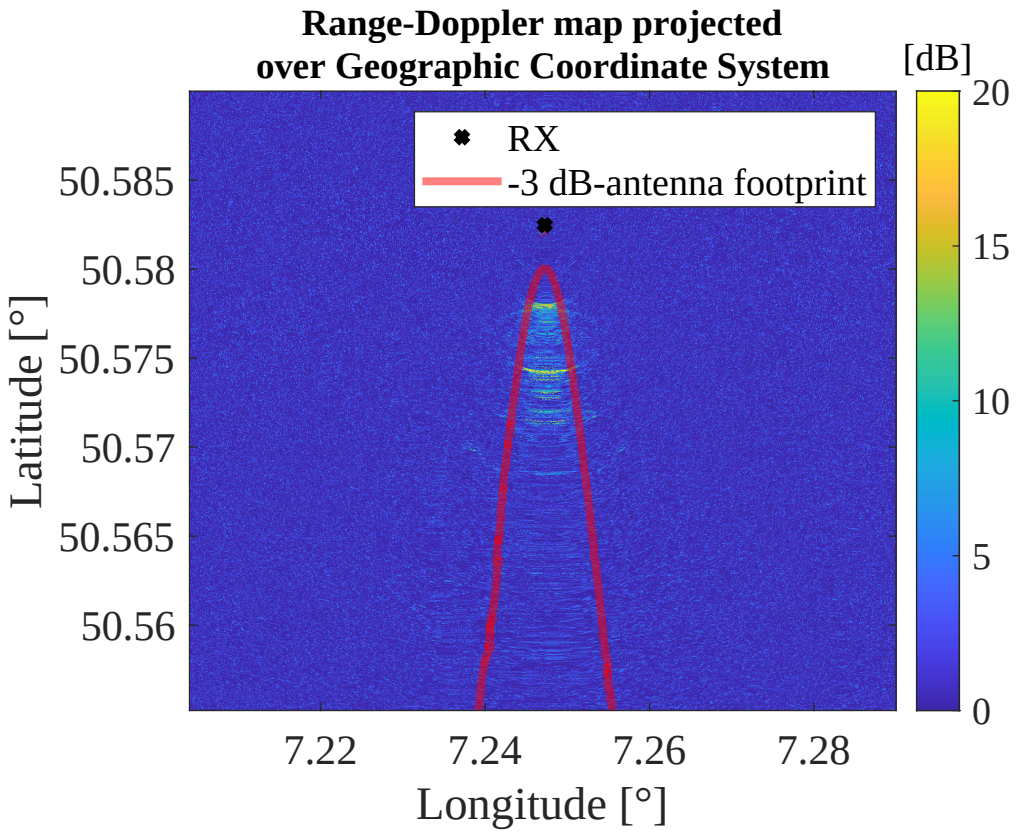

Figure 6.28: Computed range-Doppler map projected onto a geographic coordinate system around the receiver location.

by the dense satellite constellations and the development of methods to select the reference satellite based on the optimization of the geometry for the area of interest. Nevertheless, comparing the projected range-Doppler map onto the geographic coordinates, distinctive features of the monitored area can be observed, e.g. the limit of the river.

Figure 6.30 represents the computed range-Doppler map for another time interval further on the satellite trajectory showing how the evolution of the geometry along the satellite pass changes the bistatic range and Doppler frequency of the received scattered signals. This is also observed in Figure 6.31 which represents a max hold of the range-Doppler maps computed during 8 seconds, clearly showing the bistatic range and Doppler migration that even clutter scattered signals suffer and the need to apply motion compensation techniques based on an accurate estimation of the satellite positions during the CPI to effectively increased the integration time and possibly improve the signal-to-noise ratio of the scattered signals and the resolution in the cross-range dimension.

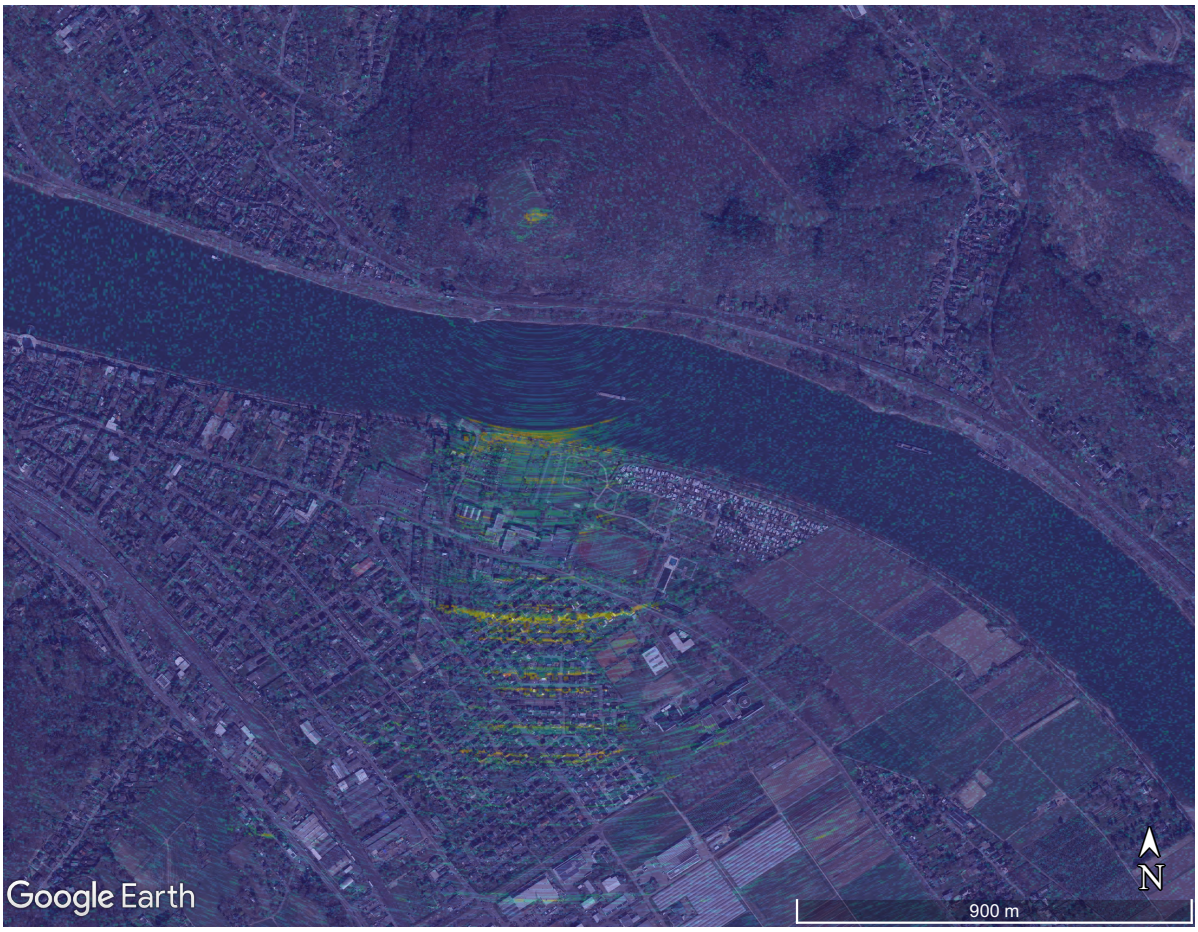

Figure 6.29: Computed range-Doppler map projected onto a geographic coordinate system around the receiver location and compared with a satellite image from Google Earth.

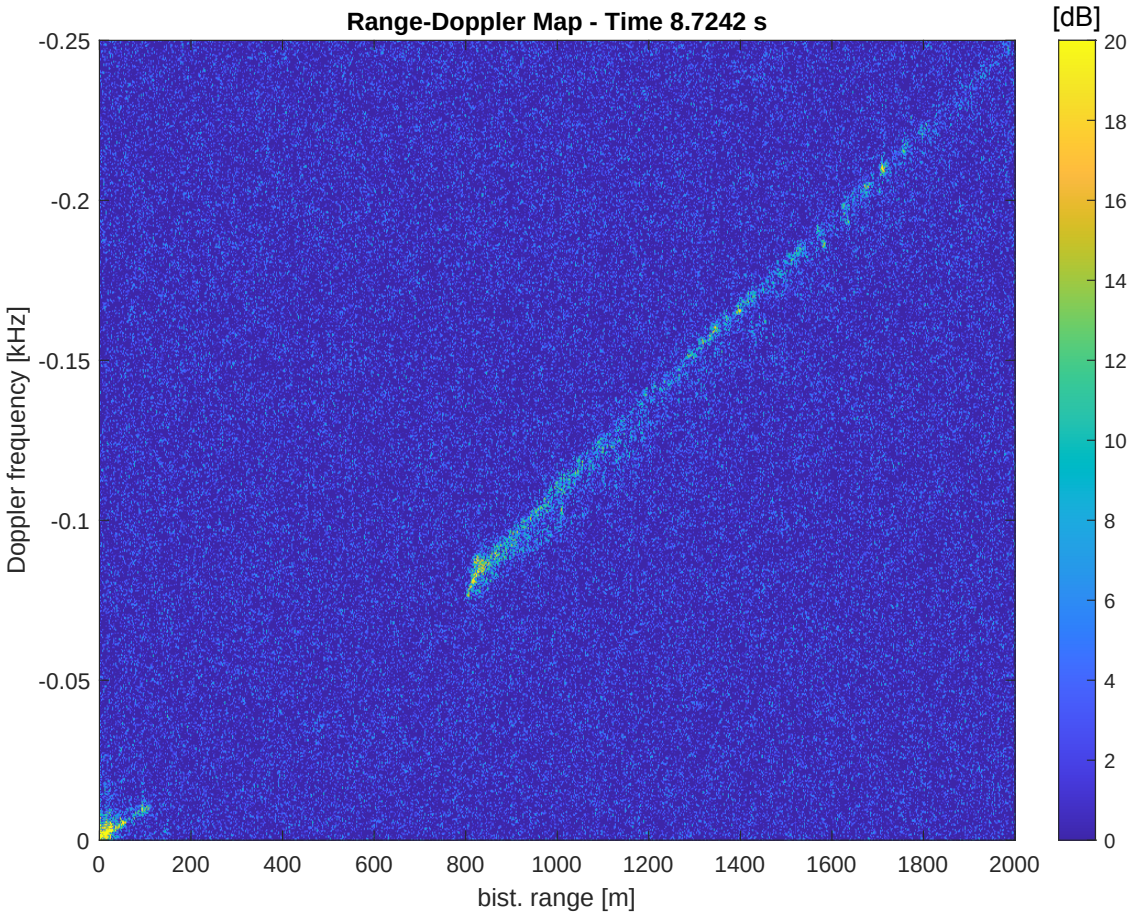

Figure 6.30: Range-Doppler map computed with a 0.54 s CPI by cross-correlating the reference signal received with the Kymeta antenna and the surveillance signal received with the horn antenna looking South for a OneWeb acquisition with the satellite approaching from South for a later time than the result in Figure 6.22.

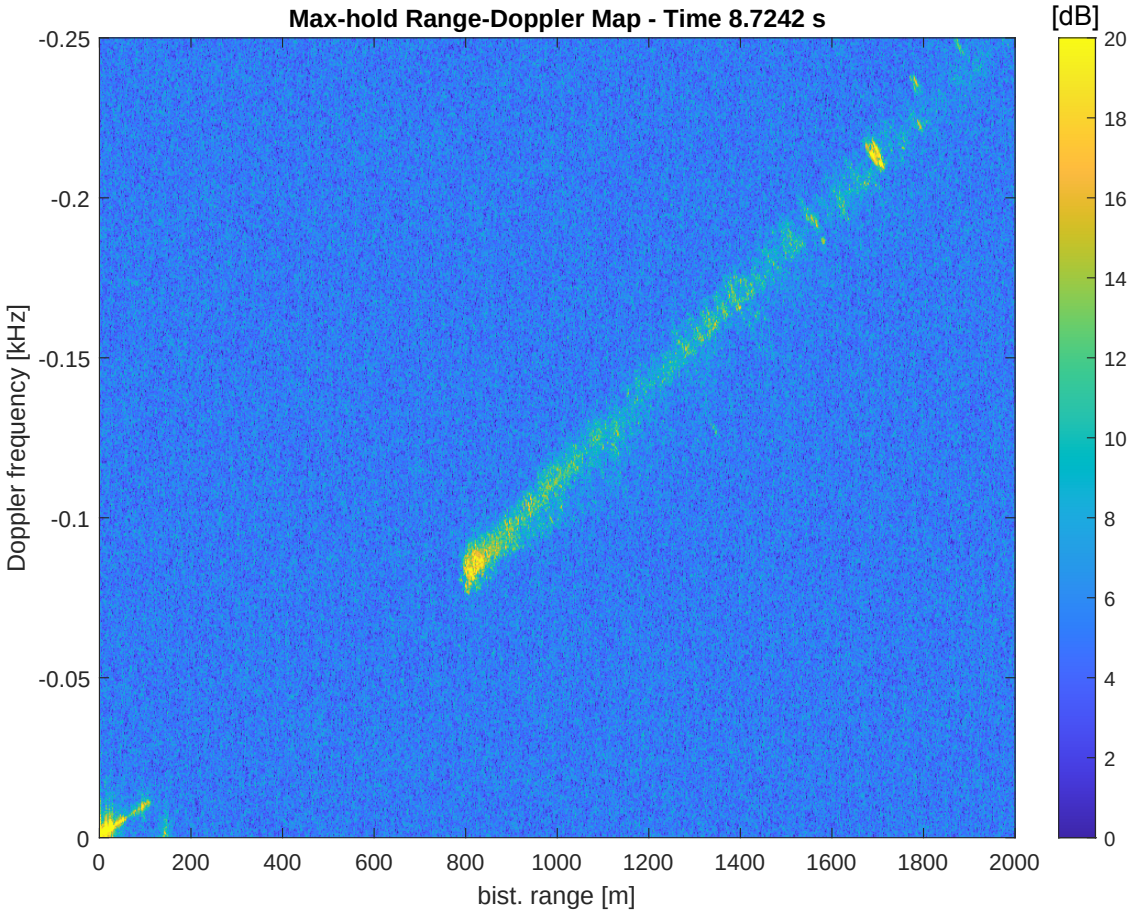

Figure 6.31: Max-hold over the range-Doppler maps with CPI 0.54 s computed during 8.7 s for the considered OneWeb acquisition.

6.2 Drone detection measurements

A measurement campaign at Fraunhofer FHR (50°37'2.12"N, 7°7'40.62"E) with a cooperative target, i.e. a medium size DJI Matrice 350 RTK drone, has also been performed to evaluate and validate the possibility of exploiting these LEO satellite signals as illumination of opportunity for surveillance applications.

Figure 6.32 shows the setup and location of the measurement in which two Kymeta antennas were used as reference antennas and two horn antennas with a baseline of 70 cm between them were used as surveillance antennas. The manual tilt of the Kymeta antennas was set to zero, i.e. pointing towards zenith, and they were controlled to tracked the selected reference satellites after an azimuth calibration based on the reference direction from Astra 19.2° satellites. The horn antennas, which have an estimated -3 dB-beamwidth of 30°, were manually pointed towards 230° in azimuth with an elevation of 9° monitoring a sector in which the cooperative target performed radial flights at a speed of around 4 m/s.

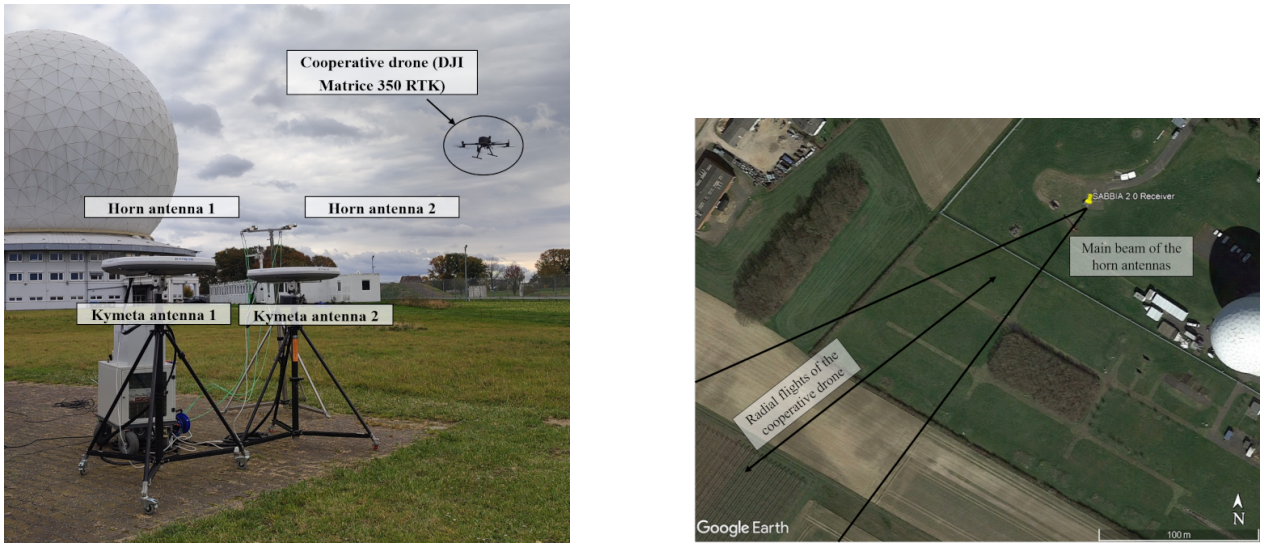

Figure 6.32: Measurement scenario to validate the target detection capabilities: Picture of the setup including the cooperative drone, two Kymeta antennas used as reference channels and two surveillance horn antennas used as surveillance channels (left), and satellite view of the area indicating the pointing and monitored sector of the horn antennas in which radial flights were performed by the cooperative drone.

As preliminary results, Figure 6.33 shows the obtained range-Doppler map based on the cross-correlation of a OneWeb reference signal received by a Kymeta antenna and a surveillance signal received by a horn antenna for a CPI of 0.36 s during a time interval in which the

drone was approaching the receiver at approximately 4 m/s. A scattered signal at around 150 m bistatic range and 115 Hz bistatic Doppler frequency, which could be associated to the cooperative target can be observed. However, the non-coherent integration of range-Doppler maps computed during 3 s shows a blurred target response, which is expected given the high range resolution of the system and the range migration effects. Therefore, in order to increase the CPI, target motion compensation techniques would be require in order to improve the SNR of the target scattered signals and enable the detection of targets at longer ranges or targets of lower RCS.

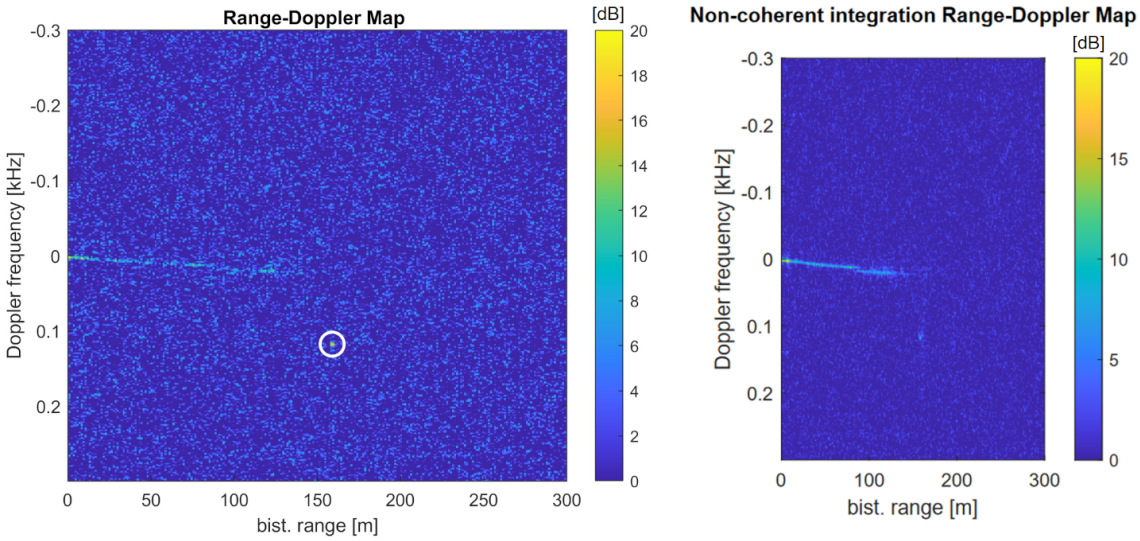

Figure 6.33: Preliminary drone detection results: Range-Doppler map computed by the cross-correlation using a OneWeb reference signal received by a Kymeta antenna and a surveillance signal received by a horn antenna with a CPI of 0.36 s for a time in which the drone was approaching the receiver at 4 m/s (left) and non-coherent integration of range-Doppler maps with CPI 0.36 s computed during 3 seconds (right).

Nevertheless, this result also experimentally validates the exploitation of user-downlink signals from broadband communication LEO satellites for target detection applications showing the feasibility to detect a medium-size drone at ranges up to at least 150 m using a surveillance antenna of 30° -3 dB-beamwidth. The application of target motion compensation techniques [Pig17] to enable longer coherent integration times and clutter cancellation algorithms [Col09] is expected to improve these results and enhance the target detection capabilities of the proposed system.

6.3 Conclusions

The exploitation of user-downlink signals transmitted by the novel broadband communication LEO satellites as emerging illuminators of opportunity for passive radar applications has been analysed and experimentally validated using developed prototypes.

The characteristics of these satellite constellations such as Starlink or OneWeb are of great interest for the development of satellite-based passive radars in terms of their global and persistent coverage, number of satellites, estimated received power level on Earth surface and maximum signal bandwidth. Theoretical analyses performed of the maximum achievable range and Doppler resolutions, as well as the experimental characterisation of their signals for passive radar applications, have shown the promising capabilities of these illuminators of opportunity.

The design and development of a passive radar architecture based on the use of narrow-beam high-gain antennas with satellite tracking capabilities to receive the reference signals have also allowed to carry out measurement campaigns for the experimental validation of this emerging concept. These field tests have demonstrated the capability to detect clutter scattered signals from a monitored urban area up to 1.5 km from the receiver, and scattered signals from a medium-size drone up to 150 m from the receiver using a 30° -3 dB-beamwidth horn antenna for the surveillance channel.

However, a number of limitations has been observed and discussed, which need to be further addressed in order to develop more robust systems with enhanced capabilities.

As the considered LEO satellites are communication systems and not broadcast systems, the availability and characteristics of the signals is closely related to the transmission of data payload, the number of users, and the handover and resource allocation protocols used by these satellites. Therefore, it is necessary to identify robust signal components (i.e. "always on" signals) such as the beacon signals transmitted by Starlink satellites, or to implement automatic search methods to select the appropriate satellite and frequency channel with data transmission. Furthermore, system capabilities such as, for example, range or cross-range resolutions depend on the bistatic geometry and, therefore, the reference satellite can be

selected based on the optimisation of the geometry for the area of interest. The expansion of these satellite constellations and the deployment of new ones that will provide greater spatial and signal diversity are expected to improve the availability of signals transmitted with a suitable geometry, although this will also increase the complexity of the selection methods. Also, the development of digital arrays with the ability to synthesise multiple independent beams will allow the simultaneous tracking and reception of multiple reference signals transmitted by different satellites, enabling the application of multistatic techniques.

The predictable movement of LEO satellites theoretically enables the application of imaging methods to improve cross-range resolution based on bistatic SAR with ground-based receivers. However, to allow the application of imaging methods based on the satellite movement compensation, e.g. back-projection, and to increase the coherent integration time, the position estimation accuracy typically obtained by propagating the satellite TLE data with the SGP4 model is not enough to focus the scattered signal responses, being necessary to implement more accurate estimation methods possibly based on the processing of the direct signals (e.g. orbit determination techniques based on the estimation of the Doppler frequency of the received direct signals). In addition, these satellite dynamics also give rise to range and Doppler migration effects and spread clutter in target detection applications, requiring the application of TMC techniques to effectively increase the coherent integration time and more complex clutter cancellation or GMTI algorithms.

The results obtained in this part of the thesis have demonstrated the technical feasibility of exploiting broadband communication LEO satellite signals for passive radar systems, enabling the application of emerging remote sensing or surveillance techniques. Besides, the ongoing expansion of the spatial sector with an increasing number of planned satellite constellations, including also governmental communication constellations such as the European IRIS^2, and the use of novel frequency bands, such as V-band, are expected to promote further investigation and developments of the presented concepts and techniques.

Part IV

CONCLUSIONS

Chapter 7

Conclusions and Future Work

Based on the discussion of the results and conclusions presented in the parts associated with the LTE-based passive radar and the broadband communication LEO satellite-based passive radar, this chapter presents the main conclusions of this thesis and the envisioned future research lines.

7.1 Conclusions

This thesis has focused on the analysis, design, development and experimental validation of systems and techniques for the exploitation of two types of complementary emerging illuminators of opportunity in passive radar applications:

1. Downlink signals of the LTE mobile communications system.
2. User-downlink signals in the 10.7 GHz to 12.7 GHz band of the novel broadband communication LEO satellite constellations such as Starlink and OneWeb.

The emerging multi-channel COTS SDR devices with enhanced capabilities have been mainly used as the enabling technology for the development of prototypes and the experimental validation of the proposed techniques.

As stated in the introduction, the objective of this thesis was to demonstrate both theoretically and experimentally the technical feasibility of using the considered wireless

communication systems (i.e. LTE and LEO communication satellite constellations) as illuminators of opportunity by: performing the analysis and characterization for passive radar applications of both systems and their transmitted user-downlink signals; developing passive radar prototypes; and conducting measurement campaigns to validate the developments.

The performed analyses and experimental characterization of the downlink LTE signals demonstrate the technical feasibility and suitable properties to exploit them as illumination of opportunity in passive radar applications. Besides, a system architecture based on the use of adaptive digital array techniques implemented using COTS SDR has been proposed and validated in a measurement campaign with focus on drone detection for critical infrastructure surveillance. The results of this field test has shown the feasibility to detect small drones at close range using a non-calibrated adaptive beamforming technique and exploiting the LTE downlink signals. The main advantage of this system lies in its reduced cost compared to active radars. In addition, this system does not require frequency allocation, does not contribute to the congestion of the electromagnetic spectrum or interferes with critical communication systems, and operates in all light and weather conditions, making it a suitable technology for the surveillance of critical infrastructures.

However, limitations have been identified related to the required dynamic range of the receivers, the effects of the network load on the performance of the radar system, and the occurrence of blind sectors when applying digital beamforming techniques, which impact in the performance and robustness of the proposed LTE-based passive radar system. These limitations could be addressed by developing methods that optimize the selection of the base station and frequency channel considered as reference signal, by optimizing the deployment of the receiving node in order to achieve a suitable bistatic geometry for the area of interest, and by resorting to a multistatic configuration exploiting several base stations or deploying multiple receiving nodes.

Regarding the broadband communication LEO satellites with persistent and global coverage, the analysis of their characteristics showed promising potential capabilities to be exploited as illumination of opportunity for passive radar applications in comparison with other satellite-based illuminators of opportunity, justifying the great interest in experimentally investigating

this concept. For this reason, after developing experimental systems that enable the validation of the proposed techniques, two measurement campaigns were performed demonstrating the feasibility to detect clutter scattered signals, and a medium-sized drone at a range of 150 m using a 30° beamwidth horn antenna in the surveillance channel.

All these results that show the promising capabilities of the proposed systems contribute to the development of new applications and advanced techniques in the context of urban multistatic surveillance based on passive radar nodes exploiting mobile communication signals, and of persistent remote area or infrastructure monitoring, for example, for avalanche detection, exploiting the novel broadband communication LEO satellites.

7.2 Future research lines

Since this doctoral thesis has validated the exploitation of both LTE and broadband communication LEO satellite signals for passive radar application, showing promising results and enabling the application of novel techniques, many topics could be further investigated. Those considered of high relevance are described below.

Analysis and development of a multistatic LTE-based passive radar configuration for urban scenarios. Given the complexity of urban scenarios in terms of moving targets, clutter and line-of-sight blocking, the analysis and development of a multistatic configuration with multiple receiving LTE-based nodes, also operating in FSR mode, and exploiting the typically dense transmitter network are considered of great interest in order to address current limitations. Besides, the proposed system can be expanded to exploit the new standards of mobile communication systems such as 5G and the future 6G, although further investigation is required in order to overcome limitations such as those imposed by the intensive spatial multiplexing used in these novel systems, which challenges the passive radar operation by making the acquisition of a reference signal more difficult. In this context of urban surveillance, it is also considered relevant the application of the emerging concepts and techniques of Joint Communication and Sensing (JCAS) or Integrated Sensing and Communication (ISAC) in which some cooperation from the transmitter is expected.

Application of advanced passive radar techniques based on the exploitation of LEO satellite signals. Once validated the feasibility of using these satellite signals as illumination of opportunity for passive radar, many advanced techniques can be investigated in order to improve the performance of the system and expand its capabilities:

- Application of imaging methods such as SAR exploiting the transmitter movement in order to improve the cross range resolution and achieve a persistent local area monitoring with ground-based receivers. To enable the application of these algorithms, more accurate methods to improve the satellite position estimation are required, since the propagation of TLE data using SGP4 does not show enough accuracy to, for example, effectively perform the backprojection algorithm.
- Application of Ground Moving Target Indicator (GMTI) and clutter cancellation techniques in order to improve the detection of moving targets. Besides, the movement of the targets might also enable the application of inverse SAR techniques or the measurement of micro-Doppler signatures for target classification.
- Application of techniques enabled by multichannel receivers such as polarimetry (by recording orthogonal polarizations), single-pass interferometry (by recording different spatial channels) or multistatic approaches (by simultaneously tracking several reference satellites).
- Integrated operation with other satellite-based illuminators of opportunity, such as DVB-S that offers a complimentary and static illumination source.
- Operation on moving platforms while maintaining the satellite tracking based on dual GNSS/IMU sensors.

Bibliography

[Abr23] K. Abratkiewicz, A. Księżyk, M. Płotka, P. Samczyński, J. Wszołek, and T. P. Zieliński, "SSB-based signal processing for passive radar using a 5G network", *IEEE Journal of Selected Topics in Applied Earth Observations and Remote Sensing*, vol. 16, pp. 3469–3484, 2023.

[Adv] Advanced Radar Technologies, *Art Midrange 3D*, [Online]. Available at: https://advancedradartechnologies.com/products/art-drone-sentinel-2/.

[Al 22] B. Al Homssi, A. Al-Hourani, K. Wang, P. Conder, S. Kandeepan, J. Choi, B. Allen, and B. Moores, "Next generation mega satellite networks for access equality: Opportunities, challenges, and performance", *IEEE Communications Magazine*, vol. 60, no. 4, pp. 18–24, 2022.

[Alm23] A. Almodóvar-Hernández, D. Mata-Moya, M.-P. Jarabo-Amores, N. Rey-Maestre, and M. Benito-Ortiz, "Motion compensation for long integration times and DoA processing in passive radars", *Remote Sensing*, vol. 15, no. 4, p. 1031, 2023.

[Axe03] S. R. Axelsson, "Noise radar for range/Doppler processing and digital beamforming using low-bit ADC", *IEEE Transactions on Geoscience and Remote Sensing*, vol. 41, no. 12, pp. 2703–2720, 2003.

[Bak05] C. Baker, H. Griffiths, and I. Papoutsis, "Passive coherent location radar systems. part 2: Waveform properties", *IEE Proceedings-Radar, Sonar and Navigation*, vol. 152, no. 3, pp. 160–168, 2005.

[Bár15] J.-L. Bárcena-Humanes, P.-J. Gómez-Hoyo, M.-P. Jarabo-Amores, D. Mata-Moya, and N. De-Rey-Maestre, "Feasibility study of EO SARs as opportunity illuminators

in passive radars: PAZ-based case study", *Sensors*, vol. 15, no. 11, pp. 29 079–29 106, 2015.

[Bar21] C. B. Barneto, S. D. Liyanaarachchi, M. Heino, T. Riihonen, and M. Valkama, "Full duplex radio/radar technology: The enabler for advanced joint communication and sensing", *IEEE Wireless Communications*, vol. 28, no. 1, pp. 82–88, 2021.

[Bar19] C. B. Barneto, T. Riihonen, M. Turunen, L. Anttila, M. Fleischer, K. Stadius, J. Ryynänen, and M. Valkama, "Full-duplex OFDM radar with LTE and 5G NR waveforms: Challenges, solutions, and measurements", *IEEE Transactions on Microwave Theory and Techniques*, vol. 67, no. 10, pp. 4042–4054, 2019.

[Bea22] P. J. Beasley and M. A. Ritchie, "Bladerad: Development of an active and passive, multistatic enabled, radar system", in *2021 18th European Radar Conference (EuRAD)*, IEEE, 2022, pp. 98–101.

[Beh15] F. Behner, S. Reuter, H. Nies, and O. Loffeld, "Synchronization and processing in the HITCHHIKER bistatic SAR experiment", *IEEE Journal of Selected Topics in Applied Earth Observations and Remote Sensing*, vol. 9, no. 3, pp. 1028–1035, 2015.

[Ber10] F. Berizzi, M. Martorella, D. Petri, M. Conti, and A. Capria, "USRP technology for multiband passive radar", in *2010 IEEE Radar Conference*, IEEE, 2010, pp. 225–229.

[Bis10] H. Bischl, H. Brandt, T. de Cola, R. De Gaudenzi, E. Eberlein, N. Girault, E. Alberty, S. Lipp, R. Rinaldo, B. Rislow, *et al.*, "Adaptive coding and modulation for satellite broadband networks: From theory to practice", *International Journal of Satellite Communications and Networking*, vol. 28, no. 2, pp. 59–111, 2010.

[Bla23a] G. P. Blasone, F. Colone, and P. Lombardo, "Forward-looking passive radar with non-uniform linear array for automotive applications", *IEEE Transactions on Vehicular Technology*, 2023.

[Bla23b] G. P. Blasone, F. Colone, P. Lombardo, and P. Markiton, "Passive STAP approaches for GMTI", in *Passive Radars on Moving Platforms*, Institution of Engineering and Technology, 2023, pp. 213–264.

[Blá23a] R. Blázquez-García, D. Cristallini, M. Ummenhofer, V. Seidel, J. Heckenbach, and D. O'Hagan, "Experimental comparison of Starlink and Oneweb signals for passive radar", in *2023 IEEE Radar Conference (RadarConf23)*, IEEE, 2023, pp. 1–6.

[Blá23b] R. Blázquez-García, D. Cristallini, M. Ummenhofer, V. Seidel, J. Heckenbach, and D. O'Hagan, "Capabilities and challenges of passive radar systems based on broadband low-Earth orbit communication satellites", *IET Radar, Sonar & Navigation*, 2023.

[Blá23c] R. Blázquez-García, D. Cristallini, M. Ummenhofer, V. Seidel, J. Heckenbach, and D. O'Hagan, "Multichannel passive radar demonstrator based on Starlink satellite signals for persistent bistatic SAR interferometry", in *IGARSS 2023-2023 IEEE International Geoscience and Remote Sensing Symposium*, IEEE, 2023, pp. 403–406.

[Blá22a] R. Blázquez-García, M. Ummenhofer, D. Cristallini, and D. O'Hagan, "Experimental acquisition of Starlink satellite transmissions for passive radar applications", in *2022 IET Radar Conference (Radar)*, IET, 2022, pp. 1–6.

[Blá22b] R. Blázquez-García, M. Ummenhofer, D. Cristallini, and D. O'Hagan, "Passive radar architecture based on broadband LEO communication satellite constellations", in *2022 IEEE Radar Conference (RadarConf22)*, IEEE, 2022, pp. 1–6.

[Bro13] J. W. Brown, "FM airborne passive radar", Ph.D. dissertation, UCL (University College London), 2013.

[Cas08] E. E. Case, A. M. Zelnio, and B. D. Rigling, "Low-cost acoustic array for small UAV detection and tracking", in *2008 IEEE National Aerospace and Electronics Conference*, IEEE, 2008, pp. 110–113.

[Cel] CelesTrak, *Current supplemental two-line element sets*, [Online]. Available at: http://celestrak.com/NORAD/elements/supplemental.

[Cha14] B. K. Chalise, Y. D. Zhang, M. G. Amin, and B. Himed, "Target localization in a multi-static passive radar system through convex optimization", *Signal Processing*, vol. 102, pp. 207–215, 2014.

[Cha18] C.-Y. Chang, D. Sabella, D. García-Roger, D. Ferling, F. Tillman, G. M. Dell'Aera, L. G. Baltar, M. Färber, M. Payaró, N. Nikaein, *et al.*, "Implementation of hardware and software platforms", in *5G System Design: Architectural and Functional Considerations and Long Term Research*, Wiley Online Library, 2018, pp. 483–520.

[Che98] V. Chemyak, "Fundamentals of multisite radar systems", in *Multistatic radars and Multiradar Systems*, Gordon and Breach Science Publishers, 1998.

[Che21] J. Chen, M. Xing, H. Yu, B. Liang, J. Peng, and G.-C. Sun, "Motion compensation/autofocus in airborne synthetic aperture radar: A review", *IEEE Geoscience and Remote Sensing Magazine*, vol. 10, no. 1, pp. 185–206, 2021.

[Che19] Z. Cheng, Z. He, and B. Liao, "Target detection performance of collocated MIMO radar with one-bit ADCs", *IEEE Signal Processing Letters*, vol. 26, no. 12, pp. 1832–1836, 2019.

[Che16] K. Chetty, Q. Chen, and K. Woodbridge, "Train monitoring using GSM-R based passive radar", in *2016 IEEE Radar Conference (RadarConf)*, IEEE, 2016, pp. 1–4.

[Col13] F. Colone, C. Bongioanni, and P. Lombardo, "Multifrequency integration in FM radio-based passive bistatic radar. part I: Target detection", *IEEE Aerospace and Electronic Systems Magazine*, vol. 28, no. 4, pp. 28–39, 2013.

[Col20] F. Colone, "DVB-T-based passive forward scatter radar: Inherent limitations and enabling solutions", *IEEE Transactions on Aerospace and Electronic Systems*, vol. 57, no. 2, pp. 1084–1104, 2020.

[Col21] F. Colone, C. Bongioanni, and P. Lombardo, "Experimental results for a passive forward scatter radar based on OFDM waveforms of opportunity", in *2021 21st International Radar Symposium (IRS)*, IEEE, 2021, pp. 1–10.

[Col12] F. Colone, P. Falcone, C. Bongioanni, and P. Lombardo, "WiFi-based passive bistatic radar: Data processing schemes and experimental results", *IEEE Transactions on Aerospace and Electronic Systems*, vol. 48, no. 2, pp. 1061–1079, 2012.

[Col09] F. Colone, D. O'hagan, P. Lombardo, and C. Baker, "A multistage processing algorithm for disturbance removal and target detection in passive bistatic radar",

IEEE Transactions on Aerospace and Electronic Systems, vol. 45, no. 2, pp. 698–722, 2009.

[Col16] F. Colone, C. Palmarini, T. Martelli, and E. Tilli, "Sliding extensive cancellation algorithm for disturbance removal in passive radar", *IEEE Transactions on Aerospace and Electronic Systems*, vol. 52, no. 3, pp. 1309–1326, 2016.

[Con12] M. Conti, F. Berizzi, M. Martorella, E. Dalle Mese, D. Petri, and A. Capria, "High range resolution multichannel DVB-T passive radar", *IEEE Aerospace and Electronic Systems Magazine*, vol. 27, no. 10, pp. 37–42, 2012.

[Cri10] D. Cristallini, M. Caruso, P. Falcone, D. Langellotti, C. Bongioanni, F. Colone, S. Scafe, and P. Lombardo, "Space-based passive radar enabled by the new generation of geostationary broadcast satellites", in *2010 IEEE Aerospace Conference*, IEEE, 2010, pp. 1–11.

[Cri23a] D. Cristallini, D. O'Hagan, T. Weyland, and R. Blázquez-García, "Outlook on future trends", in *Passive Radars on Moving Platforms*, Institution of Engineering and Technology, 2023, pp. 291–312.

[Cri23b] D. Cristallini, R. Blazquez-Garcia, and D. O'Hagan, "K-space signal occupancy of Starlink signals and their applications in passive radar imaging", in *2023 IEEE Radar Conference (RadarConf23)*, IEEE, 2023, pp. 1–6.

[Cri18] D. Cristallini, I. Pisciottano, and H. Kuschel, "Multi-band passive radar imaging using satellite illumination", in *2018 International Conference on Radar (RADAR)*, IEEE, 2018, pp. 1–6.

[Cui15] G. Cui, J. Liu, H. Li, and B. Himed, "Signal detection with noisy reference for passive sensing", *Signal Processing*, vol. 108, pp. 389–399, 2015.

[Dah16] E. Dahlman, S. Parkvall, and J. Skold, *4G, LTE-advanced Pro and the Road to 5G*. Academic Press, 2016.

[Dan17] L. Daniel, S. Hristov, X. Lyu, A. G. Stove, M. Cherniakov, and M. Gashinova, "Design and validation of a passive radar concept for ship detection using communication satellite signals", *IEEE Transactions on Aerospace and Electronic Systems*, vol. 53, no. 6, pp. 3115–3134, 2017.

[Del19] I. Del Portillo, B. G. Cameron, and E. F. Crawley, "A technical comparison of three low Earth orbit satellite constellation systems to provide global broadband", *Acta astronautica*, vol. 159, pp. 123–135, 2019.

[del17] N. del-Rey-Maestre, D. Mata-Moya, M.-P. Jarabo-Amores, P.-J. Gómez-del-Hoyo, J.-L. Bárcena-Humanes, and J. Rosado-Sanz, "Passive radar array processing with non-uniform linear arrays for ground target's detection and localization", *Remote sensing*, vol. 9, no. 7, p. 756, 2017.

[del19] N. del-Rey-Maestre, D. Mata-Moya, M.-P. Jarabo-Amores, P.-J. Gomez-del-Hoyo, and J. Rosado-Sanz, "Optimum beamforming to improve UAV's detection using DVB-T passive radars", in *2019 International Radar Conference (RADAR)*, IEEE, 2019, pp. 1–6.

[dQue19] Á. D. de Quevedo, F. I. Urzaiz, J. G. Menoyo, and A. A. López, "Drone detection and radar-cross-section measurements by RAD-DAR", *IET Radar, Sonar & Navigation*, vol. 13, no. 9, pp. 1437–1447, 2019.

[EPA] EPAK, *Dsi9 ku, marine internet antenna*, [Online]. Available at: https://www.epak.de/en/vsat-internet-systems/vsat-dsi9ku-pro-90cm.

[Eur17] European Telecommunications Standards Institute (ETSI), *ETSI TS 136 211: LTE; Evolved Universal Terrestrial Radio Access (E-UTRA); Physical channels and modulation (GPP TS 36.211 version 14.2.0 release 14)*, 2017.

[Eve15] A. Evers and J. A. Jackson, "Cross-ambiguity characterization of communication waveform features for passive radar", *IEEE Transactions on Aerospace and Electronic Systems*, vol. 51, no. 4, pp. 3440–3455, 2015.

[Fan18] G. Fang, J. Yi, X. Wan, Y. Liu, and H. Ke, "Experimental research of multistatic passive radar with a single antenna for drone detection", *IEEE Access*, vol. 6, pp. 33 542–33 551, 2018.

[FLI] FLIR Systems, *Uncompromising vision in the pursuit of security*, [Online]. Available at: https://www.flir.com/applications/security/.

[Fol05] F. Folster and H. Rohling, "Data association and tracking for automotive radar networks", *IEEE Transactions on Intelligent Transportation Systems*, vol. 6, no. 4, pp. 370–377, 2005.

[Gar19] J. L. Garry and G. E. Smith, "Experimental observations of micro-Doppler signatures with passive radar", *IEEE Transactions on Aerospace and Electronic Systems*, vol. 55, no. 2, pp. 1045–1052, 2019.

[Gas16] G. Gassier, G. Chabriel, J. Barrère, F. Briolle, and C. Jauffret, "A unifying approach for disturbance cancellation and target detection in passive radar using OFDM", *IEEE Transactions on Signal Processing*, vol. 64, no. 22, pp. 5959–5971, 2016.

[Gen20a] Z. Geng, "Evolution of netted radar systems", *IEEE Access*, vol. 8, pp. 124 961–124 977, 2020.

[Gen20b] Z. Geng, R. Xu, and H. Deng, "LTE-based multistatic passive radar system for UAV detection", *IET Radar, Sonar & Navigation*, vol. 14, no. 7, pp. 1088–1097, 2020.

[Gho10] A. Ghosh, J. Zhang, J. G. Andrews, and R. Muhamed, *Fundamentals of LTE*. Pearson Education, 2010.

[Gom18] R. Gomes, L. Sismeiro, C. Ribeiro, T. R. Fernandes, M. G. Sanchez, A. Hammoudeh, and R. F. Caldeirinha, "Will COTS RF front-ends really cope with 5G requirements at mmWave?", *IEEE Access*, vol. 6, pp. 38 745–38 769, 2018.

[Gom22a] P. Gomez-del-Hoyo, N. del-Rey-Maestre, M.-P. Jarabo-Amores, D. Mata-Moya, and M.-C. Benito-Ortiz, "Improved 2D ground target tracking in GPS-based passive radar scenarios", *Sensors*, vol. 22, no. 5, p. 1724, 2022.

[Gom22b] P. Gomez-Del-Hoyo, K. Gronowski, and P. Samczynski, "The STARLINK-based passive radar: Preliminary study and first illuminator signal measurements", in *2022 23rd International Radar Symposium (IRS)*, IEEE, 2022, pp. 350–355.

[Gom23a] P. Gomez-Del-Hoyo and P. Samczynski, "Digital steerable antenna control system for IoO tracking in Starlink based passive radar applications", in *2023 24th International Radar Symposium (IRS)*, IEEE, 2023, pp. 1–10.

[Gom23b] P. Gomez-del-Hoyo, P. Samczynski, and F. Michalak, "Analysis of Starlink users' downlink for passive radar applications: Signal characteristics and ambiguity function performance", in *2023 IEEE Radar Conference (RadarConf23)*, IEEE, 2023, pp. 1–6.

[Gri05] H. Griffiths and C. Baker, "Passive coherent location radar systems. Part 1: Performance prediction", *IEE Proceedings-Radar, Sonar and Navigation*, vol. 152, no. 3, pp. 153–159, 2005.

[Gri22] H. D. Griffiths and C. J. Baker, *An introduction to passive radar*. Artech House, 2022.

[Har78] F. J. Harris, "On the use of windows for harmonic analysis with the discrete Fourier transform", *Proceedings of the IEEE*, vol. 66, no. 1, pp. 51–83, 1978.

[Hay23] S. Hayek, J. Saroufim, and Z. M. Kassas, "Ephemeris error modeling in opportunistic LEO satellite tracking with pseudorange and Doppler measurements", in *Proceedings of the 36th International Technical Meeting of the Satellite Division of The Institute of Navigation (ION GNSS+ 2023)*, 2023, pp. 2123–2133.

[He16] R. He, B. Ai, G. Wang, K. Guan, Z. Zhong, A. F. Molisch, C. Briso-Rodriguez, and C. P. Oestges, "High-speed railway communications: From GSM-R to LTE-R", *IEEE Vehicular Technology Magazine*, vol. 11, no. 3, pp. 49–58, 2016.

[Hen23] M. Henninger, S. Mandelli, A. Grudnitsky, T. Wild, and S. ten Brink, "Crap: Clutter removal with acquisitions under phase noise", in *2023 2nd International Conference on 6G Networking (6GNet)*, IEEE, 2023, pp. 1–8.

[Hen17] B. L. P. Henríquez and E. Deakin, *High-Speed Rail and Sustainability: Decision-making and the political economy of investment*. Taylor & Francis, 2017.

[Hen] Hensoldt, *Twinvis passive radar*, [Online]. Available at: https://www.hensoldt.net/products/radar-iff-and-datalink/twinvis-passive-radar/.

[Hum23] T. E. Humphreys, P. A. Iannucci, Z. M. Komodromos, and A. M. Graff, "Signal structure of the Starlink Ku-band downlink", *IEEE Transactions on Aerospace and Electronic Systems*, 2023.

[Ind] Indra Sistemas, *Perimeter protection: Fencing*, [Online]. Available at: https://www.indracompany.com/en/perimeter-protection-fencing.

[Jac19] A. Jackman, "Consumer drone evolutions: Trends, spaces, temporalities, threats", *Defense & Security Analysis*, vol. 35, no. 4, pp. 362–383, 2019.

[Jar23] N. Jardak and R. Adam, "Practical use of Starlink downlink tones for positioning", *Sensors*, vol. 23, no. 6, p. 3234, 2023.

[Jęd22] K. Jędrzejewski, M. Malanowski, K. Kulpa, Ł. Maślikowski, and M. Bączyk, "A concept of a multiband passive radar system for air traffic control on general aviation airfields", in *2022 23rd International Radar Symposium (IRS)*, IEEE, 2022, pp. 356–360.

[Jov18] S. Jovanoska, M. Brötje, and W. Koch, "Multisensor data fusion for UAV detection and tracking", in *2018 19th International Radar Symposium (IRS)*, IEEE, 2018, pp. 1–10.

[Jov21] S. Jovanoska, B. Knoedler, D. P. Palanivelu, L. Still, T. Fiolka, M. Oispuu, C. Steffes, and W. Koch, "Passive sensor processing and data fusion for drone detection", in *Proceedings of the NATO STO Meeting Proceedings: MSG-SET-183 Specialists' Meeting on Drone Detectability: Modelling the Relevant Signature, Prague, Czech Republic*, 2021, pp. 27–29.

[Kan20] C. K. Kang, "Development of a peripheral-central vision system to detect and characterize airborne threats", Ph.D. dissertation, Virginia Tech, 2020.

[Kha21] J. Khalife, M. Neinavaie, and Z. M. Kassas, "The first carrier phase tracking and positioning results with Starlink LEO satellite signals", *IEEE Transactions on Aerospace and Electronic Systems*, vol. 58, no. 2, pp. 1487–1491, 2021.

[Kla16] J. Klare, O. Biallawons, and D. Cerutti-Maori, "Detection of UAVs using the MIMO radar MIRA-CLE Ka", in *Proceedings of EUSAR 2016: 11th European Conference on Synthetic Aperture Radar*, VDE, 2016, pp. 1–4.

[Kno20] B. Knoedler, C. Steffes, and W. Koch, "Detecting and tracking a small UAV in GSM passive radar using track-before-detect", in *2020 IEEE Radar Conference (RadarConf20)*, IEEE, 2020, pp. 1–6.

[Ksi23] A. Księęyk, M. Płotka, K. Abratkiewicz, R. Maksymiuk, J. Wszołek, P. Samczyński, and T. P. Zieliński, "Opportunities and limitations in radar sensing based on 5G broadband cellular networks", *IEEE Aerospace and Electronic Systems Magazine*, 2023.

[Kul08] K. Kulpa, "The CLEAN type algorithms for radar signal processing", in *2008 Microwaves, Radar and Remote Sensing Symposium*, IEEE, 2008, pp. 152–157.

[Kum23] A. Kumar, E. Giusti, and M. Martorella, "Hybrid polarimetry inverse SAR", in *2023 IEEE International Radar Conference*, IEEE, 2023.

[Kum20] P. Kumari, A. Mezghani, and R. W. Heath, "A low-resolution ADC proof-of-concept development for a fully-digital millimeter-wave joint communication-radar", in *ICASSP 2020-2020 IEEE International Conference on Acoustics, Speech and Signal Processing (ICASSP)*, IEEE, 2020, pp. 8619–8623.

[Kus13] H. Kuschel, J. Heckenbach, and J. Schell, "Deployable multiband passive/active radar for air defense (dmpar)", *IEEE Aerospace and Electronic Systems Magazine*, vol. 28, no. 9, pp. 37–45, 2013.

[Kym] Kymeta, *U8 antenna*, [Online]. Available at: https://www.kymetacorp.com/solutions/.

[Leó15] F. León-Infante, J.-T. González-Partida, R. Blázquez-García, and M. Burgos-García, "Processing chain of a radar network for safety improvement in the usage of heavy machinery", in *2015 European Radar Conference (EuRAD)*, IEEE, 2015, pp. 157–160.

[Li16] C. J. Li and H. Ling, "An investigation on the radar signatures of small consumer drones", *IEEE Antennas and Wireless Propagation Letters*, vol. 16, pp. 649–652, 2016.

[Li10] Q. Li, G. Li, W. Lee, M.-i. Lee, D. Mazzarese, B. Clerckx, and Z. Li, "MIMO techniques in WiMAX and LTE: A feature overview", *IEEE Communications Magazine*, vol. 48, no. 5, pp. 86–92, 2010.

[Li04] W. Li, X. Huang, and H. Leung, "Performance evaluation of digital beamforming strategies for satellite communications", *IEEE Transactions on Aerospace and Electronic Systems*, vol. 40, no. 1, pp. 12–26, 2004.

[Lin22] P. Lingadevaru, B. Pardhasaradhi, and P. Srihari, "Feasibility of adopting 6G frequencies for transmitter of opportunity by passive radar", in *2022 IEEE International Symposium on Smart Electronic Systems (iSES)*, IEEE, 2022, pp. 326–330.

[Liu17] A. Liu, Q. Yang, X. Zhang, and W. Deng, "Collision avoidance radar system for the bullet train: Implementation and first results", *IEEE Aerospace and Electronic Systems Magazine*, vol. 32, no. 5, pp. 4–17, 2017.

[Lom12] P. Lombardo, F. Colone, W. Melvin, and J. Scheer, "Advanced processing methods for passive bistatic radar systems", in *Principles of modern radar: advanced radar techniques*, SciTech Publishing Raleigh, NC, USA, 2012, pp. 739–821.

[Loz10] A. Lozano and N. Jindal, "Transmit diversity vs. spatial multiplexing in modern MIMO systems", *IEEE Transactions on Wireless Communications*, vol. 9, no. 1, pp. 186–197, 2010.

[Lü19] M. Lü, J. Yi, X. Wan, and Y. Liu, "Experimental research of drone monitoring using multi-static passive radar", *The Journal of Engineering*, vol. 2019, no. 20, pp. 6795–6798, 2019.

[Ma17] H. Ma, M. Antoniou, D. Pastina, F. Santi, F. Pieralice, M. Bucciarelli, and M. Cherniakov, "Maritime moving target indication using passive GNSS-based bistatic radar", *IEEE Transactions on Aerospace and Electronic Systems*, vol. 54, no. 1, pp. 115–130, 2017.

[Ma18] H. Ma, M. Antoniou, A. G. Stove, J. Winkel, and M. Cherniakov, "Maritime moving target localization using passive GNSS-based multistatic radar", *IEEE Transactions on Geoscience and Remote Sensing*, vol. 56, no. 8, pp. 4808–4819, 2018.

[Mak22] R. Maksymiuk, K. Abratkiewicz, P. Samczyński, and M. Płotka, "Rényi entropy-based adaptive integration method for 5G-based passive radar drone detection", *Remote Sensing*, vol. 14, no. 23, p. 6146, 2022.

[Mal19] M. Malanowski, *Signal processing for passive bistatic radar*. Artech House, 2019.

[Mal14] M. Malanowski, K. Kulpa, J. Kulpa, P. Samczynski, and J. Misiurewicz, "Analysis of detection range of FM-based passive radar", *IET Radar, Sonar & Navigation*, vol. 8, no. 2, pp. 153–159, 2014.

[Mal09] M. Malanowski, K. Kulpa, and R. Suchozebrski, "Two-stage tracking algorithm for passive radar", in *2009 12th International Conference on Information Fusion*, IEEE, 2009, pp. 1800–1806.

[Mar23a] P. Markiton, F. Colone, and P. Lombardo, "Pasive radar for GMTI", in *Passive Radars on Moving Platforms*, Institution of Engineering and Technology, 2023, pp. 175–211.

[Mar17] T. Martelli, F. Murgia, F. Colone, C. Bongioanni, and P. Lombardo, "Detection and 3D localization of ultralight aircrafts and drones with a WiFi-based passive radar", in *International Conference on Radar Systems (Radar 2017)*, IET, 2017, pp. 1–6.

[Mar20] T. Martelli, F. Colone, and R. Cardinali, "DVB-T based passive radar for simultaneous counter-drone operations and civil air traffic surveillance", *IET Radar, Sonar & Navigation*, vol. 14, no. 4, pp. 505–515, 2020.

[Mar23b] M. Martorella and D. Cristallini, "Introduction to passive radar", in *Passive Radars on Moving Platforms*, Institution of Engineering and Technology, 2023, pp. 1–25.

[McD] J. C. McDowell, *General catalog of artificial space objects, release 1.5.4*, [Online]. Available at: https://planet4589.org/space/gcat.

[Min] Ministerio de Asuntos Económicos y Transformación Digital, *Portal Infoantenas*, [Online]. Available at: https://geoportal.minetur.gob.es/VCTEL/vcne.do.

[Mol22] D. M. Molla, H. Badis, L. George, and M. Berbineau, "Software defined radio platforms for wireless technologies", *IEEE Access*, vol. 10, pp. 26 203–26 229, 2022.

[Mos15] C. Moscardini, D. Petri, A. Capria, M. Conti, M. Martorella, and F. Berizzi, "Batches algorithm for passive radar: A theoretical analysis", *IEEE Transactions on Aerospace and Electronic Systems*, vol. 51, no. 2, pp. 1475–1487, 2015.

[Mül17] T. Müller, "Robust drone detection for day/night counter-UAV with static VIS and SWIR cameras", in *Ground/Air Multisensor Interoperability, Integration, and Networking for Persistent ISR VIII*, SPIE, vol. 10190, 2017, pp. 302–313.

[Mun22] J. F. Munoz-Martin, N. Rodriguez-Alvarez, X. Bosch-Lluis, and K. Oudrhiri, "Stokes parameters retrieval and calibration of hybrid compact polarimetric GNSS-R signals", *IEEE Transactions on Geoscience and Remote Sensing*, vol. 60, pp. 1–11, 2022.

[Nat] National Instruments, *USRP-2945 specifications*, [Online]. Available at: https://www.ni.com/docs/de-DE/bundle/usrp-2945-specs/page/specs.html.

[NAT20] NATO STO Task Group-227, "Cognitive radar. cognitive jammer-based ISAR passive radar", STO Technical Report, Tech. Rep., 2020.

[Nei23] M. Neinavaie and Z. M. Kassas, "Unveiling Starlink LEO satellite OFDM-like signal structure enabling precise positioning", *IEEE Transactions on Aerospace and Electronic Systems*, 2023.

[Nei21a] M. Neinavaie, J. Khalife, and Z. M. Kassas, "Acquisition, Doppler tracking, and positioning with Starlink LEO satellites: First results", *IEEE Transactions on Aerospace and Electronic Systems*, vol. 58, no. 3, pp. 2606–2610, 2021.

[Nei21b] M. Neinavaie, J. Khalife, and Z. M. Kassas, "Blind Doppler tracking and beacon detection for opportunistic navigation with LEO satellite signals", in *2021 IEEE Aerospace Conference (50100)*, IEEE, 2021, pp. 1–8.

[Ngu19] N. H. Nguyen and K. Doğançay, *Signal Processing for Multistatic Radar Systems: Adaptive Waveform Selection, Optimal Geometries and Pseudolinear Tracking Algorithms*. Academic Press, 2019.

[Ngu16] P. Nguyen, M. Ravindranatha, A. Nguyen, R. Han, and T. Vu, "Investigating cost-effective RF-based detection of drones", in *Proceedings of the 2nd workshop on micro aerial vehicle networks, systems, and applications for civilian use*, 2016, pp. 17–22.

[Nic22] J. Nicolás-Álvarez, X. Carreño-Megias, E. Ferrer, M. Albert-Galí, J. Rodríguez-Tersa, A. Aguasca, and A. Broquetas, "Interferometric orbit determination system for geosynchronous SAR missions: Experimental proof of concept", *Remote Sensing*, vol. 14, no. 19, p. 4871, 2022.

[Noh20] G. Noh, B. Hui, and I. Kim, "High speed train communications in 5G: Design elements to mitigate the impact of very high mobility", *IEEE Wireless Communications*, vol. 27, no. 6, pp. 98–106, 2020.

[Núñ23] J. M. Núñez-Ortuño, J. P. González-Coma, R. Nocelo López, F. Troncoso-Pastoriza, and M. Álvarez-Hernández, "Beamforming techniques for passive radar: An overview", *Sensors*, vol. 23, no. 7, p. 3435, 2023.

[OHa20] D. O'Hagan, D. Cristallini, V. Seidel, and L. Cesbron Lavau, "Passive radar avalanche warning method and system", EP3926363A1, 2020.

[OHa18] D. W. O'Hagan, S. R. Doughty, and M. R. Inggs, "Multistatic radar systems", in *Academic Press Library in Signal Processing, Volume 7*, Elsevier, 2018, pp. 253–275.

[Och17] J. Ochodnickỳ, Z. Matousek, M. Babjak, and J. Kurty, "Drone detection by Ku-band battlefield radar", in *2017 International Conference on Military Technologies (ICMT)*, IEEE, 2017, pp. 613–616.

[Osw06] V. Osweiler, "Covariance Estimation and Autocorrelation of NORAD Two-Line Element Sets", Thesis, 2006.

[Pal14] L. Pallotta, "Covariance matrix estimation for radar applications", Ph.D. dissertation, Università degli Studi di Napoli Federico II, 2014.

[Pal12] J. E. Palmer, H. A. Harms, S. J. Searle, and L. Davis, "DVB-T passive radar signal processing", *IEEE transactions on Signal Processing*, vol. 61, no. 8, pp. 2116–2126, 2012.

[Par] Parasol, *Parasol passive radar - demand-controlled obstacle lighting - ADLS*, [Online]. Available at: https://www.passiv-radar.de/en/.

[Pas20] D. Pastina, F. Santi, F. Pieralice, M. Antoniou, and M. Cherniakov, "Passive radar imaging of ship targets with GNSS signals of opportunity", *IEEE Transactions on Geoscience and Remote Sensing*, vol. 59, no. 3, pp. 2627–2642, 2020.

[Pat18] J. S. Patel, F. Fioranelli, and D. Anderson, "Review of radar classification and RCS characterisation techniques for small UAVs or drones", *IET Radar, Sonar & Navigation*, vol. 12, no. 9, pp. 911–919, 2018.

[Pet15] T. Pető, "Multichannel passive radar receiver platform", in *2015 17th International Conference on Transparent Optical Networks (ICTON)*, IEEE, 2015, pp. 1–4.

[Pig17] F. Pignol, F. Colone, and T. Martelli, "Lagrange-polynomial-interpolation-based Keystone transform for a passive radar", *IEEE Transactions on Aerospace and Electronic Systems*, vol. 54, no. 3, pp. 1151–1167, 2017.

[Pis18] S. Pisa, E. Piuzzi, E. Pittella, P. Lombardo, A. Genovese, D. Bloisi, D. Nardi, P. d'Atanasio, and A. Zambotti, "Numerical and experimental evaluation of

the radar cross section of a drone", in *2018 15th European Radar Conference (EuRAD)*, IEEE, 2018, pp. 309–312.

[Pis19] I. Pisciottano, D. Cristallini, and D. Pastina, "Maritime target imaging via simultaneous DVB-T and DVB-S passive ISAR", *IET Radar, Sonar & Navigation*, vol. 13, no. 9, pp. 1479–1487, 2019.

[Pis20] I. Pisciottano, F. Santi, D. Pastina, and D. Cristallini, "DVB-S based passive polarimetric ISAR—methods and experimental validation", *IEEE Sensors Journal*, vol. 21, no. 5, pp. 6056–6070, 2020.

[Qui23] A. Quirini, F. Colone, and P. Lombardo, "Impact of supervised reciprocal filter on clutter cancellation in OFDM radar", in *2023 IEEE International Radar Conference*, IEEE, 2023.

[Raj16] R. S. A. Raja Abdullah, N. H. Abdul Aziz, N. E. Abdul Rashid, A. Ahmad Salah, and F. Hashim, "Analysis on target detection and classification in LTE based passive forward scattering radar", *Sensors*, vol. 16, no. 10, p. 1607, 2016.

[Raj20] R. S. A. Raja Abdullah, S. Alhaji Musa, N. E. Abdul Rashid, A. Sali, A. A. Salah, and A. Ismail, "Passive forward-scattering radar using digital video broadcasting satellite signal for drone detection", *Remote Sensing*, vol. 12, no. 18, p. 3075, 2020.

[Ric14] M. A. Richards and J. A. Scheer, *Principles of Modern Radar: Radar Applications*. SciTech Pub., 2014.

[Rod23] J. T. Rodriguez, F. Colone, and P. Lombardo, "Supervised reciprocal filter for OFDM radar signal processing", *IEEE Transactions on Aerospace and Electronic Systems*, 2023.

[Roh83] H. Rohling, "Radar CFAR thresholding in clutter and multiple target situations", *IEEE Transactions on Aerospace and Electronic Systems*, no. 4, pp. 608–621, 1983.

[Sai05] R. Saini and M. Cherniakov, "DTV signal ambiguity function analysis for radar application", *IEE Proceedings-Radar, Sonar and Navigation*, vol. 152, no. 3, pp. 133–142, 2005.

[Sam21] P. Samczyński, K. Abratkiewicz, M. Płotka, T. P. Zieliński, J. Wszołek, S. Hausman, P. Korbel, and A. Księżyk, "5G network-based passive radar", *IEEE Transactions on Geoscience and Remote Sensing*, vol. 60, pp. 1–9, 2021.

[San20] F. Santi, D. Pastina, and M. Bucciarelli, "Experimental demonstration of ship target detection in GNSS-based passive radar combining target motion compensation and track-before-detect strategies", *Sensors*, vol. 20, no. 3, p. 599, 2020.

[San21] F. Santi, I. Pisciottano, D. Pastina, and D. Cristallini, "First experimental results on multi-angle DVB-S based passive ISAR exploiting multipolar data", in *2021 IEEE Radar Conference (RadarConf21)*, IEEE, 2021, pp. 1–6.

[Sar03] T. K. Sarkar, Z. Ji, K. Kim, A. Medouri, and M. Salazar-Palma, "A survey of various propagation models for mobile communication", *IEEE Antennas and Propagation Magazine*, vol. 45, no. 3, pp. 51–82, 2003.

[Say19] A. Sayin, M. Cherniakov, and M. Antoniou, "Passive radar using Starlink transmissions: A theoretical study", in *2019 20th International Radar Symposium (IRS)*, IEEE, 2019, pp. 1–7.

[Sch15] A. Schroder, M. Renker, U. Aulenbacher, A. Murk, U. Boniger, R. Oechslin, and P. Wellig, "Numerical and experimental radar cross section analysis of the quadrocopter DJI Phantom 2", in *2015 IEEE Radar Conference*, IEEE, 2015, pp. 463–468.

[Sch05] H. Schulze and C. Lüders, *Theory and applications of OFDM and CDMA: Wideband wireless communications*. John Wiley & Sons, 2005.

[Sch17] C. Schüpbach, C. Patry, F. Maasdorp, U. Böniger, and P. Wellig, "Micro-UAV detection using DAB-based passive radar", in *2017 IEEE Radar Conference (RadarConf)*, IEEE, 2017, pp. 1037–1040.

[Sed21] S. Sedighi, K. V. Mishra, M. B. Shankar, and B. Ottersten, "Localization with one-bit passive radars in narrowband internet-of-things using multivariate polynomial optimization", *IEEE Transactions on Signal Processing*, vol. 69, pp. 2525–2540, 2021.

[Sei22] V. Seidel, J. Heckenbach, F. Kriehmigen, I. Pisciottano, M. Ummenhofer, and D. Cristallini, "High resolution DVB-S based passive radar for ISAR imaging

and drone detection", in *EUSAR 2022; 14th European Conference on Synthetic Aperture Radar*, VDE, 2022, pp. 1–4.

[Sha16] T. Shan, S. Liu, Y. D. Zhang, M. G. Amin, R. Tao, and Y. Feng, "Efficient architecture and hardware implementation of coherent integration processor for digital video broadcast-based passive bistatic radar", *IET Radar, Sonar & Navigation*, vol. 10, no. 1, pp. 97–106, 2016.

[Shi18] X. Shi, C. Yang, W. Xie, C. Liang, Z. Shi, and J. Chen, "Anti-drone system with multiple surveillance technologies: Architecture, implementation, and challenges", *IEEE Communications Magazine*, vol. 56, no. 4, pp. 68–74, 2018.

[Sho14] G. A. Showman, "An overview of radar imaging", in *Principles of Modern Radar: Radar Applications*, SciTech Pub., 2014, pp. 835–891.

[Sla23] A. Slavov, F. V. Crespi, S. Sandenbergh, D. Bok, D. O'Hagan, and P. Knott, "Coherency limits of different transceivers within USRP X310 as a radar node", in *2023 24th International Radar Symposium (IRS)*, IEEE, 2023, pp. 1–10.

[Son16] Y.-S. Song, J. Kim, S. W. Choi, and Y.-K. Kim, "Long term evolution for wireless railway communications: Testbed deployment and performance evaluation", *IEEE Communications Magazine*, vol. 54, no. 2, pp. 138–145, 2016.

[Spa16] L. Space Exploration Holdings, *SpaceX non-geostationary satellite system.* FCC filing SAT-LOA-20161115-00118, 2016.

[Spa20] Space Exploration Holdings, LLC, *Application for modification of authorization for the SpaceX NGSO satellite system*, FCC filing SAT-MOD-20200417-00037, 2020.

[spa] space-track.org, [Online]. Available at: https://www.space-track.org/.

[Sto17] A. G. Stove, M. S. Gashinova, S. Hristov, and M. Cherniakov, "Passive maritime surveillance using satellite communication signals", *IEEE Transactions on Aerospace and Electronic Systems*, vol. 53, no. 6, pp. 2987–2997, 2017.

[Su19] Y. Su, Y. Liu, Y. Zhou, J. Yuan, H. Cao, and J. Shi, "Broadband LEO satellite communications: Architectures and key technologies", *IEEE Wireless Communications*, vol. 26, no. 2, pp. 55–61, 2019.

[Sub11] I. Suberviola, I. Mayordomo, and J. Mendizabal, "Experimental results of air target detection with a GPS forward-scattering radar", *IEEE Geoscience and Remote Sensing Letters*, vol. 9, no. 1, pp. 47–51, 2011.

[Sva22] F. Svanström, F. Alonso-Fernandez, and C. Englund, "Drone detection and tracking in real-time by fusion of different sensing modalities", *Drones*, vol. 6, no. 11, p. 317, 2022.

[Tan05] D. K. Tan, H.-b. Sun, Y. Lu, M. Lesturgie, and H. L. Chan, "Passive radar using global system for mobile communication signal: Theory, implementation and measurements", *IEE Proceedings-Radar, Sonar and Navigation*, vol. 152, no. 3, pp. 116–123, 2005.

[Tay23] A. Taylor and D. Poullin, "Experimental UAV detection using 4G-LTE-based passive radar", in *2023 IEEE International Radar Conference*, IEEE, 2023.

[Ulv10] T. Ulversoy, "Software defined radio: Challenges and opportunities", *IEEE Communications Surveys & Tutorials*, vol. 12, no. 4, pp. 531–550, 2010.

[Umm20] M. Ummenhofer, L. C. Lavau, D. Cristallini, and D. O'Hagan, "UAV micro-Doppler signature analysis using DVB-S based passive radar", in *2020 IEEE International Radar Conference (RADAR)*, IEEE, 2020, pp. 1007–1012.

[Umm23] M. Ummenhofer, V. Seidel, J. Heckenbach, R. Blázquez-García, and D. Cristallini, "First results of DVB-S based passive polarimetric measurements of micro-Doppler signatures of a helicopter", in *2023 IEEE International Radar Conference*, IEEE, 2023.

[Val01] D. A. Vallado, *Fundamentals of astrodynamics and applications*. Springer Science & Business Media, 2001, vol. 12.

[Van02] H. L. Van Trees, *Optimum array processing: Part IV of detection, estimation, and modulation theory*. John Wiley & Sons, 2002.

[Was19] C. Wasserzier, P. Wojaczek, D. Cristallini, J. Worms, and D. O'Hagan, "Doppler-spread clutter suppression in single-channel noise radar", in *2019 International Radar Conference (RADAR)*, IEEE, 2019, pp. 1–4.

[Woj18] P. Wojaczek, F. Colone, D. Cristallini, and P. Lombardo, "Reciprocal-filter-based STAP for passive radar on moving platforms", *IEEE Transactions on Aerospace and Electronic Systems*, vol. 55, no. 2, pp. 967–988, 2018.

[Wor20] WorldVu Satellites Limited, *OneWeb request modification of its authorization for US market access for OneWeb NGSO FSS systems*, FCC filing SAT-MLP-20200526-00062, 2020.